Materialphysik

Thermal stability of Py/Cu and Co/Cu giant magnetoresistance (GMR) multilayer systems

Inaugural-Dissertation
zur Erlangung des Doktorgrades
der Naturwissenschaften im Fachbereich Physik
der Mathematisch-Naturwissenschaftlichen Fakultät
der Westfälischen Wilhelms-Universität Münster

von
Vitaliy Vovk
aus Cherkasy/Ukraine

– 2007–

Dekan:	Prof. Dr. Johannes Peter Wessels
Erster Gutachter:	Prof. Dr. Guido Schmitz
Zweiter Gutachter:	Prof. Dr. Sergej Demokritov
Tage der mündlichen Prüfungen:	12.03.2008 / 13.03.2008 / 13.03.2008
Tag der Promotion:	13.03.2008

Лене и Кириллу
to Lena and Kyrill

Contents

Summary

NiFe/Cu and Co/Cu multilayer systems have been studied regarding the mechanisms of thermal degradation of the giant magnetoresistance effect (GMR). The different thermodynamics of the studied systems results in different mechanisms of the GMR degradation as shown by highest resolution nanoanalysis using the three dimensional wide angle tomographic atom probe.

According to the TAP analysis, GMR deterioration in Py/Cu system occurs due to the broadening of the layer interfaces observed at 250 °C. In contrast, due to the strong demixing tendency, Co/Cu multilayers remain stable up to 450 °C. At higher temperatures ferromagnetic bridging of the neighboring Co layers takes place leading to the GMR breakdown.

In both Py/Cu and Co/Cu systems recrystallization is induced at 350-450 °C, which is accompanied by a change in the crystallographic orientation from <111> to <100> wire texture. The reaction may be utilized to produce GMR sensor layers of remarkable thermal stability. Although the systems of interest are equivalent in respect of the observed phenomenon, the Ni_xFe_{1-x}/Cu system is chosen for a detailed analysis because it allows a precise control of the lattice constant by varying the Fe content in the Ni_xFe_{1-x} layer. It is shown that the crystallographic reorientation is triggered by the minimization of lattice mismatch elastic energy. Moreover, the counteraction between the elastic and interfacial energy minimizations exerts a critical influence on the recrystallization probability.

Zusammenfassung

NiFe/Cu und Co/Cu Multilagen werden in Bezug auf die thermische Stabilität des Riesen-Magnetowiderstand-Effekts untersucht. Die unterschiedlichen thermodynamischen Eigenschaften der betrachteten Systeme führen zu jeweils anderen Mechanismen, welche die Abnahme des GMR-Effekts verursachen, wie durch Nanoanalyse mit höchster Auflösung an der 3-dimensionalen Weitwinkelatomsonde gezeigt werden konnte. Nach den Ergebnissen der Nanoanalyse tritt der GMR-Zusammenbruch in Py/Cu-Systemen aufgrund der Verbreiterung der Grenzfläche, die nach der Wärmebehandlung über 200 °C beobachtet wurde, auf. Im Gegensatz dazu bleiben Co/Cu Mehrfachschichtsysteme wegen der starken Tendenz zur Entmischung bis zu 450 °C stabil. Bei höheren Temperaturen führt hier ferromagnetische Brückenbildung zwischen benachbarten Kobaltschichten zum Zusammenbruch des GMR-Effekts.

Sowohl in Py/Cu als auch in Co/Cu Systemen beginnt bei 350-450 °C eine Rekristallisation, durch die sich die kristallographische Orientierung von <111> Drahttextur in <110> umwandelt. Diese Reaktion kann genutzt werden, um GMR-Sensorschichten von beachtlicher thermischer Stabilität herzustellen. Obwohl die oben genannten Systeme bezüglich der Rekristallisationsphänomene gleichwertig sind, wurde für die Analyse das Ni_xFe_{1-x}-System gewählt, da es eine Variation der Gitterkonstanten zulässt. Es wurde gezeigt, dass die kristallographische Reorientierung durch die Minimierung der elastischen Energie ausgelöst wird. Darüber hinaus übt das Wechselspiel zwischen Minimierung der elastischen Energie und der Grenzflächenenergie kritischen Einfluss auf die Rekristallisationswahrscheinlichkeit aus.

Chapter 1

Introduction

By convention sweet, by convention bitter,
by convention hot, by convention cold,
by convention colour: but in reality atoms and void.
Democritus 460-370 BC

The development of nano-technologies defines the advance of modern electronic devices. The characteristic size of functional units decreases continuously fulfilling the Moor's law. The stability of the interfaces and the control of the materials interreaction often becomes an important issue for the reliable operation. Thus, particular interest is attracted by the very initial steps of interaction between the constituent materials, which are distinguished by steep composition gradients. In general, the kinetic behavior of these highly non-equilibrium states can not be described by the equilibrium thermodynamics. The difficulties in investigation of sharp interfaces and initial interdiffusion stages arise from the typical length scale, which does not exceed a few nanometer. In order to carry out a detailed nanoanalysis, we used the wide angle 3D atom probe (WATAP), which has been proven to yield an atomic chemical sensitivity and improved statistical significance. Using this unique technique, the single atoms of the studied materials are measured and mapped in a real 3D space providing an unambiguous picture of the interaction processes between atoms of different species.

This work deals with nanoanalysis of thin film systems revealing advanced magnetic properties. The discovery of antiferromagnetic coupling in multilayer film structures consisting of alternating ferromagnetic and non-ferromagnetic materials [1] and the GMR effect found shortly afterwards [2, 3] triggered a new wave of scientific interest. It is hard to overestimate the importance of these discoveries for industrial applications. In only nine years, the first hard disk drives with GMR read heads came to the mass production. It became one of the most important and successful innovations of the 20th century. The German and French scientists P. Grünberg and A. Fert, who independently discovered the GMR effect, were awarded the 2007 Nobel Prize in physics.

Due to their better sensitivity, GMR read heads enabled recording densities beyond 200 Gbit/in^2 (GMR read heads in combination with perpendicular recording), a perfor-

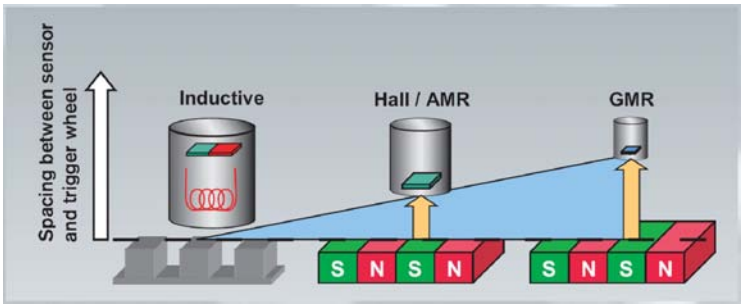

Figure 1.1: Comparison of different magnetic sensor technologies on the example of the rotation speed sensor (the graphic is taken from the Bosch advertisement booklet).

mance that was inconceivable with older thin film inductive or even magnetoresistive read heads. Nowadays, the magnetic medium itself, rather than the reading head, represents the limiting factor due to the superparamagnetic effect. Owing to further advantages, the GMR sensing devices have found a growing range of new applications. Especially the automotive industry requires the small size low power consumption magnetoelectronic sensing devices. Linear and rotary position sensors, gradiometers, current-, acceleration-, pressure sensors, ignition timing sensors allow to get a full control over a car functionality. The very high sensitivity of the GMR sensors allows to place them further away from the scanned object. In Fig. 1.1 the comparison of different magnetic sensor technologies is shown. Electronics now accounts for more than twenty percent of a vehicle's cost and there are some forecasts that this figure will increase to at least forty percent by 2010.

Short-term thermal stability at temperatures in the range of 200-400 °C during manufacturing, and for some applications, e.g. orientation and rotation speed sensors in combustion engines, the long-term stability beyond the conventional 100-150 °C, is a crucial issue. Experiments carried out on Co/Cu and Py/Cu systems ("Py" is the abbreviation used for permalloy - a $Ni_{81}Fe_{19}$ alloy) revealed the degradation of the GMR effect amplitude at about 150 °C and 120 °C, respectively [4, 5], if the thickness of individual layers was optimized for the first antiferromagnetic coupling (AFC) maximum. Systems optimized for the second AFC maximum, which are often used for practical purposes due to their better reproducibility and stability, lose their GMR properties at about 400 °C and 250 °C, respectively [6, 7].

Rather different mechanisms have been suggested to explain the GMR degradation and underlying microstructural changes. In general, Co/Cu and Py/Cu systems may be expected to behave quite differently due to the unequal thermodynamics of both systems. Transmission electron microscopy (TEM) studies of Co/Cu multilayer samples performed by Rätzke et al. [8] showed the transport of Cu into the Co layers along the grain boundaries. If the width of resulting local breaks of the Co layers corresponds to the thickness of AFC, it may affect the GMR by frustration effects. Following

Monte-Carlo simulations and experimental observations performed by Bobeth et al. [9], formation of pinholes in Co layers with subsequent fusion of these layers by coalescence of resulting bulges on the edges of holes could be responsible for the GMR breakdown caused by ferromagnetic shortcuts. In the case of Py/Cu, grain boundary diffusion of Ni into the Cu layer was initially proposed [10] to form ferromagnetic bridges between Py layers. However, recent 3DAP analysis [11] at relevant temperatures has demonstrated only minor grain boundary diffusion and identified a short-ranged interdiffusion at the interfaces due to non-equilibrium point defects as the important mechanism. One of the aims of this study is to elucidate the morphological changes in Co/Cu multilayers causing the GMR deterioration at elevated temperatures and to compare the results with those of Py/Cu system.

In addition to atomic transport by either volume or grain boundary diffusion, a further interesting process causes a dramatic modification of the microstructure of studied systems. During the abnormal grain growth induced at temperatures in the range from 350 to 500 °C, the initial <111> wire texture transforms into the quasi-single-crystalline <100> texture. Surprisingly, the integrity of the layered structure is preserved in the course of recrystallization. Since the GMR effect amplitude depends on the specific crystallographic orientation of the thin film system, this microstructural transformation can influence the thermal stability of the sensor substantially. GMR multilayers with enhanced thermal stability can be produced by preadjustment of the Cu layer thickness to the <100> recrystallization texture, as shown by our colleagues from Bielefeld University [12]. Fundamental physical mechanisms causing the observed microstructural transformation are in the focus of the current work.

This thesis is organized as follows: in the second chapter, the fundamental aspects of the spintronics are introduced. The main magnetoresistance effects and important application issues are reviewed there. Attention is paid to the origin of stresses in thin films and the effects they imply concerning the microstructure development in the multilayers. Experimental methods such as FIM and TAP analysis as well as XRD characterization techniques will be explained in the third chapter. The peculiarities of the sample preparation methods can also be found in this chapter. In the fourth and fifth chapters, performed experiments are described providing necessary experimental details and results concerning the microstructure and morphology transformation in the GMR multilayers under annealing. The sixth chapter is devoted to the analysis of the obtained experimental data. Conclusions and outlooks comprise the seventh chapter.

Chapter 2

Theoretical background

2.1 Magnetic interactions in thin film systems

The interaction of ferromagnetic (FM) materials brought in close proximity has been studied already for a very long time. But the accurate investigation of resulting phenomena became possible only in the last several decades with the development of the thin film deposition methods. Only the thin magnetic films enabled the gapless contact between different materials and well-defined layer interfaces, at which direct exchange interaction between spins takes place. The interesting effects were expected to be obtained by decreasing the spacing between two pieces of magnetic materials (in macroscopic experiments the magnets are always separated by the roughness of surfaces and oxide layers) until the situation is reached when their spins on both sides of the interface have opposite directions. For that, an interlayer (spacer layer) with different thickness can be deposited between two magnetic materials. FM fields can interact across nonmagnetic interlayers in various ways depending on the system geometry, quality of the interface and spacer material. The understanding of the interaction mechanisms is very important for the optimization of the magnetoelectronic devices. The most important coupling types are described briefly below in this section. Magnetostatic coupling, aligning the magnetizations antiparallel, may arise due to the fringing fields if the lateral dimensions are small. This situation resembles the macroscopic case, when two ferromagnets are brought in close proximity, being separated by the oxide layer and the roughness of the surfaces in contact. Opposite poles of magnets attract each other due to minimization of fringing field energy. Magnetizations can be aligned parallel due to the so-called orange peel (Néel type) coupling, arising at wavy interfaces (will be explained in more detail in Sec. 2.1.1). Parallel alignment of the magnetizations can be also achieved due to the pinhole formation through the nonmagnetic spacer, which allows direct exchange between the FM layers. Antiferromagnetic (AF) spacers may induce parallel or antiparallel coupling in FM layers depending on the number of the atomic planes in the spacer. An even number of monolayers leads to antiparallel coupling and odd number

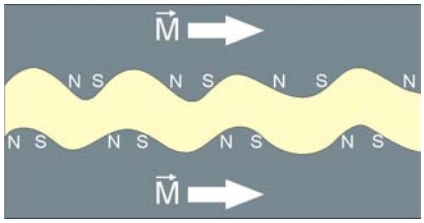

Figure 2.1: Sketch for the explanation of the orange peel coupling between two ferromagnetic films due to the conformal roughness of the interface. After Ref. [16].

to parallel coupling[1] provided the preparation of such layered systems is sufficiently accurate (atomically sharp interfaces without steps are required) [14]. But in the two past decades, the highest interest is drawn to the magnetic coupling, which possesses coupling periods that are longer than a monolayer (about 1 nm). This interesting phenomenon is observed even in systems, where the spacer is a nonmagnetic material (paramagnet or diamagnet). In the latter case magnetic coupling can not be explained due to the static magnetic order in the interlayer. This type of coupling was discovered in the end of the 80s (discovery of AF coupling in Fe/Cr/Fe systems by Grünberg et al. [1]). Its oscillatory nature, parallel and antiparallel magnetization orientation depending on the spacer thickness, was found shortly later in 1990 by Parkin et al. [15]. In consequence it was named oscillatory interlayer exchange coupling (IEC). In Sec. 2.1.2 this kind of coupling will be described in more detail because of its importance for the current study.

2.1.1 Orange peel (Néel type) coupling

Let us consider a system consisting of two FM layers separated by a nonmagnetic spacer. For the following considerations the spacer layer material is not substantial, it can be conducting as well as nonconducting. If the interfaces between layers are wavy with many protrusions, stray magnetic fields may arise having local north and south poles along the interface. If the roughness is conformal, which is the usual situation during the polycrystalline metallic film growth, the different magnetic poles of the upper and lower film oppose each other to minimize the energy of the magnetic field (see Fig. 2.1). This configuration of the magnetic poles results in the fact that magnetization vectors in both FM layers are coupled in the same direction (is referred to as FM coupling). Thus, the Néel coupling is a magnetostatic interaction of dipolar nature. In this model FM coupling can be understood without going into details of specific electron properties. This effect can be very important for GMR multilayer systems, where quite thick layers are formed by repetition of FM and nonmagnetic layers. With increasing number of double layers in the multilayer the accumulated roughness of interfaces tend to increase as well, leading to the orange peel effect, which impairs the GMR sensors [17]. However, even for so-called spin valves consisting typically only of a few single layers, this effect can not be

[1] in the literature is referred to as proximity magnetism [13]

neglected because of grain boundary (GB) grooving [18]. As it was already mentioned, FM coupling can also take place in systems with pinholes through the nonmagnetic layer, bringing the FM layers in direct contact. It is sometimes a tedious task to separate this two magnetostatic effects experimentally, since wavy interfaces often imply pinhole formation.

2.1.2 Interlayer exchange coupling

Phenomenologically, the interlayer exchange coupling between two FM 3d metals (Ni, Fe, Co or their alloys) separated by a spacer layer can be described in terms of the areal density of the interlayer exchange coupling energy, σ_{exch}:

$$\sigma_{exch} = -J_1 cos(\Delta\phi) - J_2 cos^2(\Delta\phi) = -J_1 \cdot \frac{M_1 \cdot M_2}{|M_1 \cdot M_2|} - J_2 \cdot \left(\frac{M_1 \cdot M_2}{|M_1 \cdot M_2|}\right)^2, \qquad (2.1)$$

where, J_1 and J_2 are bilinear and biquadratic coupling constants, ϕ is the angle between the magnetizations M_1 and M_2 of the FM layers on both sides of the spacer. If the first term dominates (bilinear term), then from the minimization condition Eq. 2.1 determines a FM/AF coupling behavior for positive/negative J_1, respectively. If the second term dominates (biquadratic term) and the parameter J_2 is negative, 90°-coupling results, at which noncollinear alignment of the magnetization vectors takes place [19] (this coupling type arises mainly due to the interface roughness and is neglected when describing GMR systems).

There are two different approaches, which were suggested to describe the IEC qualitatively. On the one hand, the IEC is reminiscent of the RKKY coupling mechanism [20] (named after M. A. Ruderman, C. Kittel, T. Kasuja and K. Yosida [21, 22, 23]). After this model the coupling of magnetic ions is mediated by the spin-polarized conducting electrons, which adjust the magnetic moments in the system due to the hyperfine interactions. In contrast to direct exchange coupling and superexchange mechanisms, RKKY coupling is a long-range interaction, which allowed its adaptation to the IEC explanation. However, the coupling period (or coupling length) of IEC, which is typically of about 1 nm, could not be explained in terms of RKKY showing finer oscillations. But this issue was solved later by taking into account the discrete thickness of the interlayer [24].

On the other hand, an approach developed somewhat later explains the IEC behavior in terms of quantum well states formed within the nonmagnetic layer [25, 26]. Spin-dependent reflectivity at the FM/nonmagnetic interfaces takes place because of the difference of the density of states (DOS) in FM and nonmagnetic materials, which is demonstrated in Fig. 2.2. Spin-up (majority) electrons, aligned parallel to the magnetic field, don't feel big difference between spacer and FM layers because of the similarity of their energy bands. Thus, the scattering probability for them is relatively low. The spin-down electrons, in turn, are in a different situation. The respective (minority)

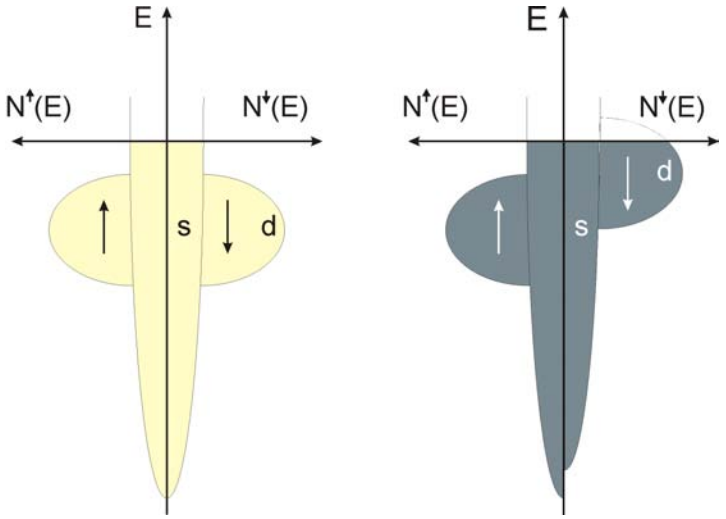

Figure 2.2: Density of states for nonmagnetic and FM materials (from left to right, respectively). For FM the energy band is split into two half-bands corresponding to different spin orientation.

bands in FM materials are always shifted to higher energies (partially beyond the Fermi-energy) due to the exchange interaction associated with ferromagnetic order. Minority electrons have to overcome a higher potential step on the FM/nonmagnetic interface than majority electrons, thus they are scattered with higher probability. Quantum well states (QWS) arise for this electron species. Standing waves may be formed in the spacer layer at certain spacer thicknesses due to interference. It should be pointed out, that these standing waves are only possible if the magnetization vectors in both FM layers are parallel. In the opposite case, minority electrons on one interface are the majority species on the other. Thus, electrons can leave the spacer layer by passing one of the interfaces without being reflected. As a consequence, no standing wave can appear. Similar to the description of a one-dimensional potential well, the condition to form a standing wave in a well of thickness D (thickness of spacer layer) is:

$$k_{\perp}^{n} = n\frac{\pi}{D}\,, \tag{2.2}$$

where $k_{\perp}^{n}$ is the electron wave vector perpendicular to the interface, n is an integer number. These wave vectors correspond to the discrete energy levels, W_n:

$$W_n = \frac{\hbar^2 (k_{\perp}^{n})^2}{2m} = n^2 \frac{\hbar^2 \pi^2}{2mD^2}\,. \tag{2.3}$$

The energy levels are shifted downwards for higher spacer thicknesses. When, with the increase of D, a new energy level crosses the Fermi energy, W_F, the correspondent QWS are filled up, and the energy of the electronic system increases. During the further increase of D, this level moves below the Fermi energy, the energy again decreases, until the next energy level approaches W_F. Thus, for the parallel magnetization alignment the energy oscillates with the spacer layer thickness variation. For the antiparallel

alignment, in turn, the energy of the system does not show oscillatory behavior and remains at a constant value. This value lies between the minima and maxima of the energy in the case of parallel alignment. As the lowest energy configuration is preferred, the alignment "rotates" between parallel and antiparallel. It is seen from Eq.2.2 that the coupling energy, and thus magnetization alignment in the FM layer, varies with the period:

$$\lambda = \frac{\pi}{k_{\perp}}, \tag{2.4}$$

and the amplitude value of the coupling strength remains the same for all spacer thicknesses. For the considerations given above, it was assumed that the spin orientation is conserved during the electron propagation through the spacer layer. This assumption, however, is not realistic for thicknesses larger than several nanometers. For higher thicknesses the spin-flip scattering diminishes the IEC considerably, leading to the exponential decay of the coupling amplitude, which is observed in experiments.

2.2 Magnetoresistance (MR) effects

The MR effect is defined as a relative change in electrical resistance under the effect of an external magnetic field. Four main magnetoresistance effects are known up to now. Although, all of them have in common the defining property, their intrinsic mechanisms are completely different. A brief overview of MR effects is given below. A few more words will be devoted to the GMR effect because of its importance for the current study.

2.2.1 Ordinary- (OMR) and anisotropic magnetoresistance (AMR)

OMR is the increase of the material resistivity in an applied magnetic field as a result of the Lorentz force acting on the electrons. Between collisions (e.g. with impurities or phonones) the electrons move along circular or helical orbits , which diminishes their effective mean free path. The OMR follows the so-called Kohler-rule [27]:

$$\frac{\rho_H - \rho_0}{\rho_0} = F\left(\frac{H}{\rho_0}\right), \tag{2.5}$$

where ρ_0 and ρ_H are the zero-field and non-zero field resistivities, respectively, F is a material dependent function and H is the applied magnetic field. The OMR increases with the increase of the applied magnetic field and is usually small in metals reaching up to 1-2% in fields of the order of 1 T. E.g., a typical value for bulk nickel in the magnetic field of $5 \cdot 10^3$ Oe is 1.6% [28]. This is a very small effect, so it is almost not used for industrial application purposes.

AMR [29] results from the spin-orbit interaction and causes the resistance to depend on the relative orientations of the magnetization and the electric current. In the direction of the magnetic field, the scattering probability of electrons is higher than that for other current to magnetization orientations. The resistivity, ρ depends on the electron scattering probability and is expressed by the following phenomenological equation:

$$\rho = \rho_{\perp} + (\rho_{\parallel} - \rho_{\perp})cos^2\theta\,, \tag{2.6}$$

where $\rho_{\parallel}$ and $\rho_{\perp}$ are the resistivities for the current density parallel and perpendicular to the magnetization orientations, respectively, and θ is the angle between the current density and the magnetization. The magnetic field range in which the AMR effect occurs is governed by the field needed to change the direction of the magnetization. It is obvious, that soft magnetic materials are used for high sensitivity sensors. At room temperature the largest effect amplitude is found in $Ni_{1-x}Co_x$ alloys, with x close to 0.2, for which the AMR amplitude reaches 6%. For Py, the bulk AMR amplitude is of about 4% [30] and scales down with the decreasing of the sensor dimensions. Thin film AMR sensors with a Py layer thickness of 30 nm show an AMR effect amplitude of about 2.5% [29], depending on the film deposition conditions. In the beginning of the 90s, inductive read heads in hard disk drives were replaced by AMR read heads. It was a very important innovation leading to the introduction of the GMR read heads shortly later, which increased the data storage density within one decade by orders of magnitudes. In fact, due to their simplicity the AMR sensors are widely used in many applications up to now, in spite of much lower effect amplitude in comparison to GMR and TMR sensors.

2.2.2 Giant magnetoresistance (GMR)

The GMR effect is observed in artificial layered structures consisting of FM and non-magnetic materials. A pronounced change of the electric resistance is observed if the magnetization configuration changes between neighboring FM layers. The resistance is higher in the case of antiparallel (or AF) magnetization relation and lower for the parallel (or FM) configuration. Quantitatively, the GMR effect is usually expressed as the relative change of the electrical resistance by the transition from FM to AM magnetization configuration:

$$\frac{\Delta R}{R_{FM}} = \frac{R_{AF} - R_{FM}}{R_{FM}}\,, \tag{2.7}$$

where R_{FM} and R_{AF} are the electrical resistances for the case of FM and AF alignment of the adjacent FM layers, respectively. The first reports about the GMR effect [2, 3] came right after the IEC discovery (see the Sec. 2.1.2), which provided the mechanism of setting the AF configuration of the magnetizations in the system. The first experiments showing the GMR effect in Fe/Cr multilayers are depicted in Fig. 2.3. At a certain nonmagnetic spacer thicknesses of 1..2 nm, the AF coupling establishes in the absence of the external magnetic field (magnetizations of odd FM layers are antiparallel to

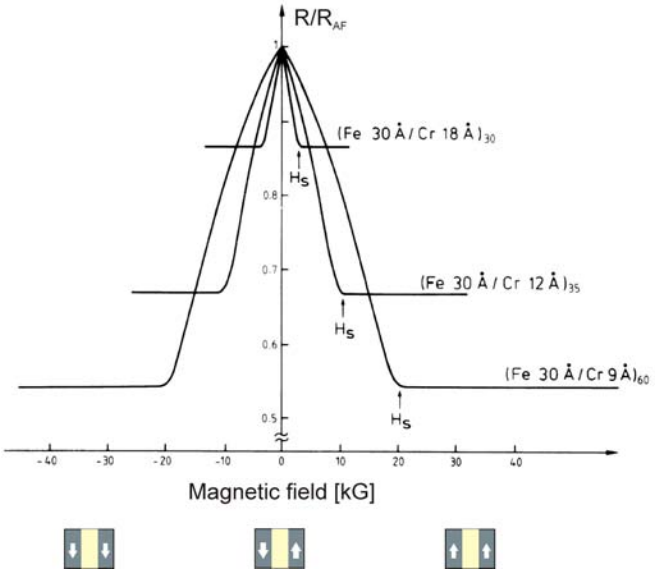

Figure 2.3: Magnetoresistance of three Fe/Cr multilayer structures at 4.2 K [2]. Magnetizations of neighboring layers, corresponding to the resistance curve are shown by arrows.

the magnetizations of even layers). External magnetic field directs the magnetizations uniformly, causing the "giant" decrease of the electrical resistance (left and right sides of the graph). The respective resistances differ by a factor of two, though, the measurement was carried out at 4.2 K and room temperature values in general are not so high. Typical GMR effect amplitudes (value of the effect in the saturation field) at room temperature are compiled in the Tab. 2.1. The name "Giant" magnetoresistance was chosen because of the much larger (at least by order of magnitude) sensitivity comparing to the AMR sensors used at that time. A huge scientific interest was focused on the GMR effect immediately after the first reports and was arisen by the considerable industrial interest in the area of magnetoelectronic sensing devices. The GMR investigation remained one of the most active areas in the solid state- and materials physics throughout the last twenty years.

The multilayer systems (see Fig. 2.4a) are not the only possible type of structures revealing the GMR effect. As an example arrays of multilayer nanowires electrodeposited into the pores of the insulating polymer matrix [32] can be mentioned. Moreover, the GMR can also be found in systems in which configurations of high electrical resistance are realized without the IEC. In the granular GMR systems [33], consisting of the nonmagnetic matrix with FM precipitates (e.g. Co/Cu), magnetic moments of the precipitates may not be coupled, thus being randomly oriented. In the presence of a sufficient external magnetic field, the GMR effect is observed due to the parallel alignment of the precipitate magnetizations (see the Fig. 2.4b). On the one hand, the GMR effect amplitude in such systems is quite low, on the other hand, the preparation of granular sensors is

Structure	$\Delta R/R_{FM}$ [%]	t_{FM} [nm]
Fe/Cr/Fe	1.5	12
Fe/Cr/Fe	5	5
$[Fe/Cr_{1.2\,nm}]_{50}$	42	0.45
Co/Cu/Co	2.0	10
Co/Cu/Co	19	3
$[Co/Cu_{0.9\,nm}]_{30}$	48	1.5
$[Co/Cu_{0.9\,nm}]_{16}$	65	1
$Co_{90}Fe_{10}/Cu/Co_{90}Fe_{10}$	6	0.8

Table 2.1: Compilation of representative GMR values of different material combinations at room temperature [31]. Additional layers, which don't contribute to the GMR, are omitted. t_{FM} is the thickness of one of the magnetic layers.

much simpler than layered ones. Another example is a multilayer system, in which the antiparallel magnetization configuration is achieved by the utilization of FM materials with different coercivities [34]. AF configuration is realized by a magnetic field which is just large enough to switch the soft magnetic layers but too low for switching the hard magnetic layers (see the Fig. 2.4c). These systems are referred to as pseudo spin-valves. A very similar principle is used in so-called spin-valves: instead of the magnetically hard layer, a soft FM layer is used, which is magnetically pinned by an AF layer (by the exchange bias effect) deposited on top of it. The magnetization of the other FM layer is free to follow the external magnetic field (see the Fig. 2.4d). Though the saturation GMR values of spin-valves are in general lower than in multilayer sensors, there are several advantages which make this structure more attractive for technical applications. Much smaller magnetic fields are needed for switching the spin-valves from FM to AF magnetizations alignment. Additionally, the direction of the external magnetic field is detected in contrast to the multilayer system, which are only able to detect the change in magnetic field strenth.

The investigations on the GMR are performed using two main geometries:

- Current in plane (CIP), at which the electrical current is measured in a direction parallel to the multilayer planes;
- Current perpendicular to plane (CPP), by measuring the electrical current perpendicular to the multilayer plane.

The magnitude of the GMR effect is stronger in the CPP case. However, special measures have to be taken in structuring and contacting of the system in order to measure the voltage drop in such unfavorable geometric conditions [35, 36] (lateral dimensions are by several orders of magnitude larger than the normal dimension along which the measurement is carried out). It is also not a trivial task to measure the electrical resis-

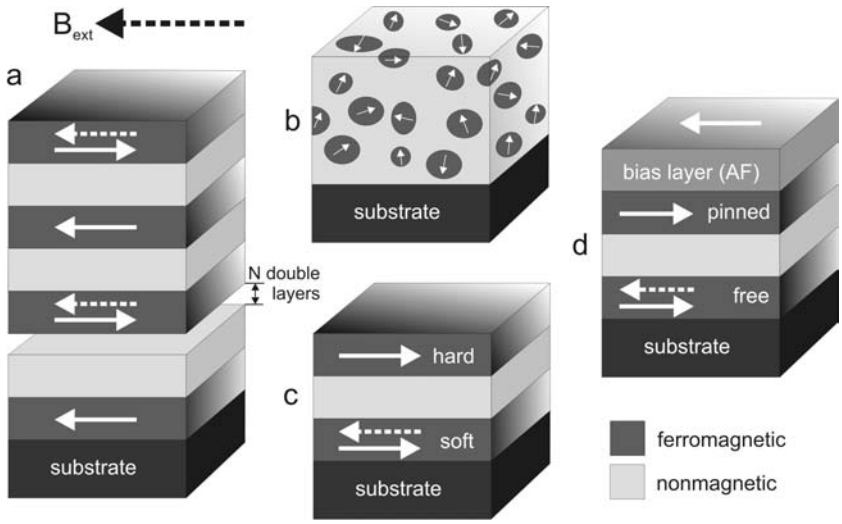

Figure 2.4: Different realizations of the GMR sensors (dashed magnetization vectors correspond to the case with applied external magnetic field): (a) Multilayer structure (magnetization); (b) Granular GMR system; (c) Pseudo spin-valve structure; (d) Spin-valve structure.

tance in a system, which is only several tens of nanometers thick. Thus, the majority of the experiments and applications use the CIP geometry.

The mechanisms of the GMR effect can be easily described by the simple two current model proposed originally by Mott in 1936 to explain the increase in resistivity of ferromagnetic metals during heating above the Curie temperature. This model assumes two independent electron channels, which are distinguished according to the projection of the electron spins along the quantization axis. The independence of this channels is provided by the fact that in metals the probability of spin-flip scattering is usually much lower then those with spin conservation. Due to the spin-dependent scattering and the spinsplit DOS of 3d transition metals described in the Sec. 2.1.2, spin-down and spin-up electron channels have different scattering probabilities in dependence on the spin to magnetization orientation and thus, different electrical resistance. The resistance is higher for antiparallel configuration (let us denote it R) and smaller for parallel spin to magnetization configuration (r). As it is seen from Fig. 2.5, in the AF coupled multilayer (left figure) both electron channels have approximately the same scattering probability due to the change of the magnetization direction from layer to layer. Spin-up and spin-down electrons are scattered strongly within one of the adjacent layers. The electrical resistance of both channels can be expressed by $R+r$. In the second case (right figure), in which the magnetizations of FM layers are parallel, a spin-up electron channel passes the whole multilayer without spin-dependent scattering (only spin-independent scattering takes place, resulting in the base value of the electrical resistance). The electrical resistance for a spin-up channel is given by $r+r$. A spin-down channel, in turn, is scattered in each FM layer because of its unfavorable spin orientation. The correspon-

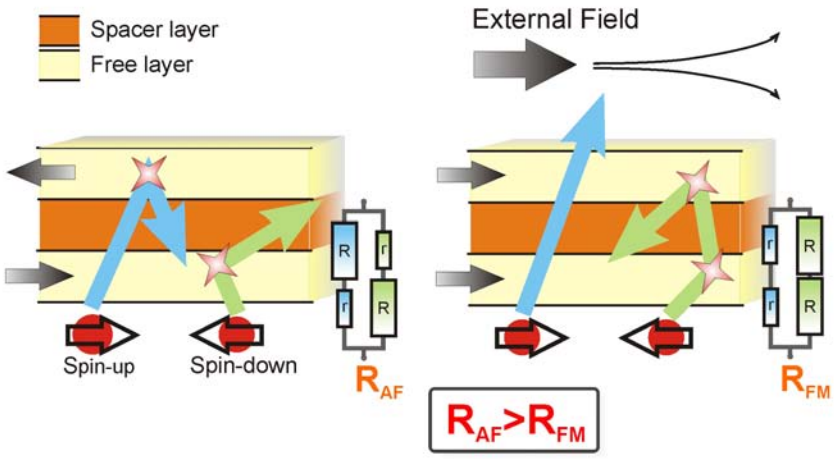

Figure 2.5: Schematic picture of the spin-dependent scattering in multilayer systems for the explanation of the GMR origin in terms of the simplistic Mott's model. Colors of the resistors in the electric circuit diagrams correspond to the colors of the electron channels.

dent resistance in this case is $R+R$. For the parallel electron channels (parallel current channels) the total resistance is given by:

$$\frac{1}{R_{AF}} = \frac{1}{R+r} + \frac{1}{R+r}; \tag{2.8}$$

$$\frac{1}{R_{FM}} = \frac{1}{r+r} + \frac{1}{R+R}. \tag{2.9}$$

It is easily seen, that the total resistance drops down at AF to FM transition ($R_{AF} > R_{FM}$), induced by applying an external magnetic field. As the energy of conduction electrons is close to the Fermi level, they propagate through the layered structure in all directions with very high velocities as compared to drift velocity in the direction of the applied electric field. Thus, both CPP (depicted in the Fig. 2.5) and CIP geometries are equal in terms of the most simple Mott's model.

2.2.3 Tunneling magnetoresistance (TMR)

The typical TMR sensor has a structure similar to that of a GMR spin-valve (see the Fig. 2.4d) apart from the nature of the spacer layer. In the TMR structures metal oxides of some 10 Å in thickness (usually Al_2O_3 or MgO) separate the FM layers by an insulating barrier. As in the case of the GMR, the TMR effect is determined by the mutual orientations of the magnetization of the FM layers. However, unlike GMR, the TMR effect is a consequence of the spin-polarized tunneling of the electrons through the insulating barrier, and it is observed in CPP geometry only. The magnitude of the

Structure	$\Delta R/R_p$ [%]	Temperature [K]
$Co/Ge_{10\,nm}/Co$	16	4.2
CoFe/ZnS/CoFe	5	270
CoFe/ZnS/CoFe	10	6
Fe/GaAs/Fe	1.55	300
$CoFeB/Al_2O_3/CoFeB$	70	300
CoFeB/MgO/CoFeB	472	300
CoFeB/MgO/CoFeB	804	5
CoFe/MgO/CoFe	220	300
CoFe/MgO/CoFe	300	4.2
Fe/MgO/Fe	180	300
Fe/Si/Fe	≈0	–

Table 2.2: TMR of different material combinations [31].

tunneling current is related to the overlap of the exponentially decaying wave functions inside the barrier. Quantitatively the TMR effect is characterized similar to the GMR by the Eq. 2.7. The first TMR experiment was carried out by M. Jullière already in 1975 [37]. He suggested that because of the applied voltage (typical voltages range from several tens to hundreds of mV) unoccupied states appear on one side of the barrier, which allows the tunneling of electrons under conservation of spin and energy. Using the DOS, one can define the spin polarization, P, of the conducting electrons:

$$P = \frac{N_\uparrow - N_\downarrow}{N_\uparrow + N_\downarrow}\,, \tag{2.10}$$

where $N_\uparrow$ and $N_\downarrow$ denote the number of states in an energy window at the Fermi level with a width given by the applied voltage. Only electrons from the states within this window can tunnel through the insulating barrier. TMR effect can be expressed with the spin polarization:

$$\frac{\Delta R}{R_{FM}} = \frac{2P^2}{1-P^2}\,. \tag{2.11}$$

In about 20 years after the TMR discovery, a remarkable attention was drawn to this effect as with the improvement of deposition techniques it was possible to prepare TMR sensors with an effect amplitude that reaches some tens of percent at room temperature. In Tab. 2.2 some representative values of the TMR effect are given. The remarkably high value of about 500% is achieved at room temperature in the TMR spin-valve with the MgO insulating layer. Nowadays, beside the common magnetic field sensor applications, TMR sensors are employed in the hard disk read heads replacing the GMR read heads as well as in magnetic non-volatile random access memory (MRAM).

2.2.4 Colossal magnetoresistance (CMR)

The CMR was found in doped manganite with perovskite structure by J. H. Santen and G. H. Jonker [38] already in 1950. Though, because of the comparably low magnetic fields reachable at that time, the full capacity of the effect was observed only in the 90s [39, 40]. The CMR effect can be extremely large resulting in a few orders of magnitude resistance change. For example the application of a magnetic field of 6 T to the epitaxial $La_{1/3}Ca_{1/3}/MnO_3$ film cooled to 77 K causes the decrease of the resistivity by the factor of 1250. The CMR originates from a metal-insulator transition in the vicinity of the Curie temperature and requires magnetic fields in the order of several Tesla. The latter properties limit the CMR application field. Though, in the last years many efforts are concentrated on making new material systems, which would exhibit the CMR at room temperature and lower magnetic fields.

2.3 Aspects of thin film growth and microstructure evolution

As this thesis concentrates on the nanocharacterization and the material physics of multilayer thin film systems, some important aspects of thin film growth need to be explained in this section. The preparation of layered systems with properties suitable for the specific purpose (grain size, texture, morphology) requires precise controlling of processing parameters and optimized structural design. In the early stages of film growth, the nature of interaction of the sputtered material with the substrate defines the further growth and formation of the specific microstructure. Surface processes (surface diffusion, interaction of adatoms with surface defects etc.) play a decisive role during the multilayer formation, since substrate and adatom materials are changing permanently during the layer to layer deposition. The influence of the substrate becomes particularly clear if epitaxial growth takes place at which the deposited material assumes the structure and lattice spacing of the substrate. As an example, the polymorphic transition of hcp Co and bcc Fe during the deposition on the fcc Cu substrate can be mentioned; as it will be proven in this work and earlier reports, e.g. [41, 42, 43], both materials assume the fcc structure of the Cu substrate at thicknesses smaller than several nanometers. Thin films with different crystallographic orientations can be achieved by the choice of appropriate substrates or special seed layers [44]. An important role in microstructure development during the deposition play intrinsic stresses arising at different stages of the thin film formation [45]. Stresses in the order of several GPa may arise due to the lattice mismatch of the deposited materials or due to the thermal expansion misfit [46]. These huge stresses may even affect the systems integrity, resulting for example in cracking of the deposited layers [45].

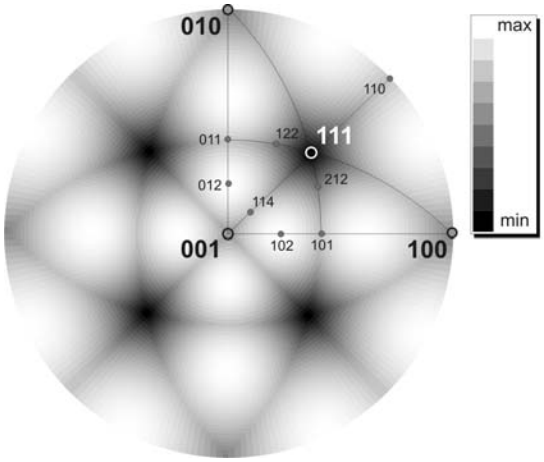

Figure 2.6: Surface energy anisotropy. The relative values of the surface energy density for the fcc lattice crystalls are depicted in the grades of grey in the standard (001) stereographic projection.

2.3.1 Surface- and interface energy

Surface energy is the net work needed to create a new surface, i.e. to cut a piece of material into two halves. In other words, it is a measure of the chemical bond disrupture needed for the formation of that surface. For the vast majority of solids, the surface energy is energetically less favorable than bulk (otherwise there would exist a driving force for the new surface formation resulting in the disintegration of the solid). There is an increase of the systems free energy caused by the disruption of the atomic bonds. However, there are different processes which can lower this free energy excess. Due to the interaction with the second and further neighbors, the normal to the surface spacing of surface atomic layers departs from the bulk value of the spacing, which restores the equilibrium to some degree. The excessive surface energy can also be accommodated by surface reconstruction. Loose atomic bonds in the surface vicinity can be reassembled resulting in a different crystal structure in this zone. But at least for some metals, as was confirmed by the ab initio simulations [47] for Cu, Ag and Au, the surface energy in the first approximation is proportional to the areal density of the broken bonds crossing the newly created surface. This is valid for all surface orientations. As a consequence, the surface energy reveals anisotropy depending on the crystallographic orientation of the surface normal. The broken bonds between second and further neighbors give a negligible contribution to the surface energy. The dependence for the ideally planar (with no steps) surface of the "perfect" fcc crystal is shown in Fig. 2.6. Calculation of the surfaces energy for the arbitrary orientation is described in more detail in Chap. 6. As it is easy to recognize, the surface energy tends to have smaller magnitude for high symmetry orientations.

Interfacial energy, being the excess free energy connected with the formation of bonds between different atomic species has substantially the same properties as the surface energy. It can be quantified by the areal density of the "A-B"-bonds created at the interface. For the fcc crystals it has essentially the same dependence on the interface normal direction as those depicted in the Fig 2.6. Though, in general the interfacial

energy is smaller than the surface energy (even the bonds between materials with high positive mixing energy are energetically more favorable than the lost bonds on the surface of correspondent materials), its contribution to the free energy of the system can be huge in the case of multilayer systems. Due to the high volume density of interfaces in multilayers having a small single layer thickness, the interfacial energy stored in such systems can be by orders of magnitude higher than the surface energy of the layer stack.

The knowledge of the directional dependence of the surface energy is sufficient to predict the minimum energy shape of the free standing atomic cluster, since it is only surface energy which changes by the shape variation. The same is applicable for small precipitates embedded in a matrix material. In this case, the interfacial energy directional dependence has to be analyzed. The low temperature equilibrium shape can be determined using the so-called Wulff construction, a method developed by G. Wulff already in the beginning of the last century [48]. At certain conditions, macroscopically flat thin film surfaces/interfaces can minimize the surface/interfacial energy by a fine-scale faceting, i.e., if the microscopical crystallographic direction does not coincide with the minimum of the surface/interfacial energy, it can be minimized by the creation of minimum-energy surface/interface segments inducing the increased roughness of the surface or interface, respectively. As will be shown in this work, interfacial energy minimization becomes particularly important for the thin film systems with curved geometry (like those used for TAP investigations). After the thermal treatment, facets of minimal interfacial energy tend to occupy a large fraction of the interface resulting in a non-uniform layer thicknesses along the interfaces.

2.3.2 Deposition modes and film microstructure

Atomic interactions of adatoms with the substrate and the deposition conditions (such as the deposition rate and the substrate temperature) essentially determine the final microstructure of the system. For example, if the surface diffusion barrier is very high, so that the thermal energy of adatoms is insufficient to overcome the barrier (low homologous temperatures), fine-crystalline and even amorphous layers can be produced. This effect is enhanced in high deposition fluxes. In contrast, coarser microstructures evolve at elevated temperatures and moderate deposition rates. Besides the kinetic factors, the onset of film growth is controlled by the interaction energies between film atoms and between film and substrate atoms. The relative magnitudes of these energies determine the mode of the film growth. If there is a tendency for film atoms to bond to surface atoms, the layer by layer growth mode is observed, which is called Frank-van der Merwe growth mode (see Fig. 2.7a). In terms of surface and interfacial energies, this mechanism takes place if the surface energy of the substrate, σ_s, is higher than the surface energy of the film, σ_f, and the interfacial energy, σ_{sf}, is not too large: $\sigma_s > \sigma_f + \sigma_{sf}$. This expression follows from the minimization of the free energy (the free energy change, Δg,

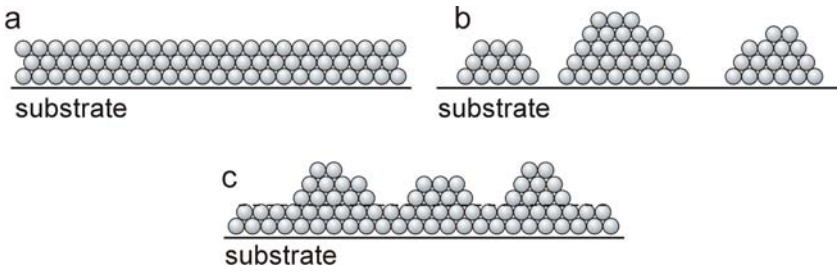

Figure 2.7: Schematic representation of classical thin film growth modes: (a) Frank-van der Merwe, (b) Volmer-Weber, and (c) Stranski-Krastanov.

should be less than zero):

$$\Delta g = A_f \sigma_f + A_{sf}(\sigma_{sf} - \sigma_s) < 0\,, \tag{2.12}$$

where A_f and A_{sf} are the areas of film and the area of film-substrate interface, respectively. For an isolated island of the deposited film, the contact angle, θ (see Fig. 2.8), can be defined from a tension balance at the contact line:

$$cos\theta = \frac{\sigma_s - \sigma_{sf}}{\sigma_f}\,. \tag{2.13}$$

This equation was derived by T. Young [49] for liquid droplets on a solid surface, but it is also valid for crystalline particles on mesoscopic scale. Thus, the Frank-van der Merwe growth mode is characterized by small contact angles of the growing film islands at which predominantly lateral growth of the atomic monolayers takes place. If bonding of adatoms to the substrate is less favorable, and for the surface and interfacial energies the relation holds: $\sigma_s < \sigma_f + \sigma_{fs}$, formation of three dimensional islands with high contact angles (approaching 90°) is observed (see Fig. 2.7b). Under continuous deposition flux, the layer develops by the impingement and coalescence of the growing islands. This type of thin film growth is called Volmer-Weber mode.

Sometimes, an intermediate growth mode is observed. The adatoms prefer bonding with the substrate atoms during the formation of the thin wetting layer (typically few monolayers) but later, three dimensional growth mode takes place (see Fig. 2.7c). This behavior is mainly observed in systems in which the film material is strained due to the size mismatch of the crystal lattices. This is the so-called Stranski-Krastanov growth mode.

Exceptional growth behavior, differing from classical growth modes, can be observed at elevated deposition temperatures or after subsequent annealing, if the surface energy

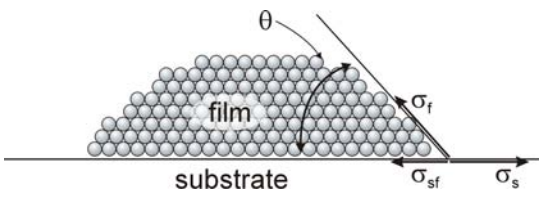

Figure 2.8: Schematic diagram of a growing film island with contact angle θ.

of the film is significantly higher than that of the substrate. Under this condition, the atomically thin films get covered with the substrate atoms in order to minimize the surface energy. Such behavior was reported for e.g. Ni deposited onto Ag single crystalline substrates upon annealing at 620-770 K [50]. Burrowing of Co nanoparticles into the Cu and Ag substrates was observed at 600 K [51]. The burrowing of the nanoparticles is a mechanism of surface smoothing in which the capillary forces play an important role.

Besides the kinetic factors and thermodynamics, the choice of epitaxial or polycrystalline microstructure is determined by the substrate nature. Using monocrystalline substrates, epitaxial growth can be achieved under special deposition conditions (high temperatures and low deposition flux). If the lattice mismatch is not too large ($<$0.5%), growth tends to be planar (van der Merwe mode). Slightly higher lattice mismatch results in the formation of islands of sputtered material (Stranski-Krastanov or Volmer-Weber mode), which, however, remain epitaxial. With the further increase of the lattice mismatch between the film and the substrate materials, epitaxial growth becomes increasingly difficult. Amorphous, polycrystalline, and monocrystalline substrates with a large lattice mismatch between the substrate and the film materials promote the polycrystalline growth. Since no directional coherency exists between film islands growing on the amorphous substrates, their impingement results in the creation of intervening grain boundaries due to the lattice translation incompatibility. Even if epitaxial growth takes place on the polycrystalline substrates, the difference in the substrate grain orientations is kept by the deposited film grains. Further growth results typically in a columnar grain structure with substrate grain boundaries being continued in the film material.

2.3.3 Classification of stresses in thin films

There is a division of thin film stresses into two categories: growth stresses and induced stresses. The first category represents intrinsic film stresses arising at different stages of the film growth. They are strongly dependent on the film and substrate materials (coherent/non-coherent bonding), substrate temperature during the deposition (mobility of adatoms, mobility of grain boundaries), growth flux and vacuum conditions. Although these stresses are usually reproducible and can be studied using various in situ techniques available nowadays, the understanding of the origins of the growth stresses is by no means complete and requires further justification. Induced stresses, in turn, are well understood. Reasonably complete models have been developed allowing quantitative estimates for the respective processes. This category of film stresses is often called extrinsic stresses, since they arise from the change of physical environment parameters subsequent to the film growth. The majority of induced stresses arise due to the substrate traction, and thus, it is not always possible to separate these stress contributions from the growth stresses. However, usually this does not pose a problem for the quantitative analysis due to the conventionality of classification. Different mechanisms for stress generation related to the metallic thin film systems have been proposed up to

now (see e.g. [52, 45]).

Growth stresses:

- surface/interface stress;
- island coalescence due to the surface energy reduction;
- grain growth or grain boundary area reduction;
- incorporation of impurities;
- vacancy annihilation;
- phase transformations and precipitation;
- structural damage as a result of high-energy deposition process;
- epitaxy constraint.

Induced stresses:

- temperature change with a difference in coefficients of thermal expansion between bonded elements;
- electrostrictive and magnetostrictive response strain;
- electrostatic forces;
- compositional segregation by bulk diffusion;
- stress induced phase transformations;
- electromigration;
- plastic or creep deformation.

The most important mechanisms resulting in the high magnitudes of stresses are subsequently discussed.

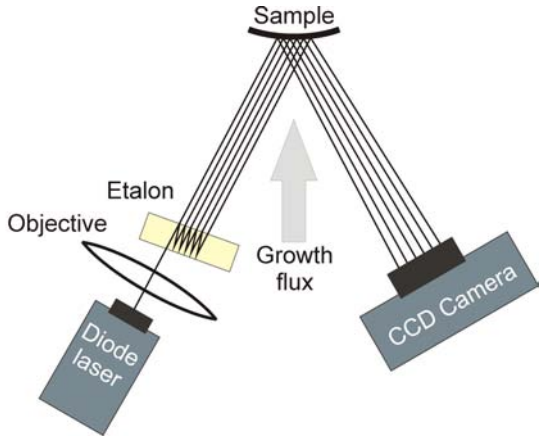

Figure 2.9: MOSS setup for in situ stress measurement.

2.3.4 Stresses in polycrystalline films

Let us first discuss the origins of intrinsic and extrinsic stresses present in a polycrystalline thin film system deposited onto an amorphous substrate. The growth of polycrystalline films begins in most cases from the formation of isolated islands (see Fig. 2.7b). Following this stage, the typical evolution of the film microstructure includes: impingement and coalescence of islands, percolation of the island array, and formation of a continuous layer and its growth. The mechanisms of stress development in these stages are not yet fully understood. However, due to the advances of in situ stress measurement techniques, it is possible to track the stress states during the deposition progress. A majority of these techniques are based on the measurement of the specimen substrate curvature, as for example the multibeam optical stress sensor (MOSS). MOSS is a laser deflectometer technique for in situ stress measurement. Compressive/tensile stresses can be assigned to the concave/convex curvature of the substrate. The basic measurement setup is depicted in Fig. 2.9. MOSS scans the sample with an array of parallel laser beams. A certain degree of divergence is induced in the laser beam array, which corresponds to the substrate curvature, κ. This divergence is measured during the deposition process by means of a CCD camera. The curvature is directly proportional to the product of effective film stress, σ, and average film thickness, h, as it is expressed by the Stoney formula:

$$\sigma h = \frac{M_s h_s^2}{6}\kappa\,, \tag{2.14}$$

where M_s and h_s are the biaxial modulus and the thickness of the substrate, respectively. Typical σh-curves for different metals are shown in Fig. 2.10. In order to get insight into the origins of the observed stress, correspondent stress states must be correlated with ex situ microstructural characterization. Such investigations allowed to identify general trends of stress behavior during the film deposition, which are characteristic to a variety of material combinations. A schematic representation of the typical stress evolution versus the film thickness is depicted in Fig. 2.11. According to that, the stress first becomes compressive, then tensile, and then again compressive. This behavior arises from a dynamic interplay between different stress generation and relaxation mechanisms.

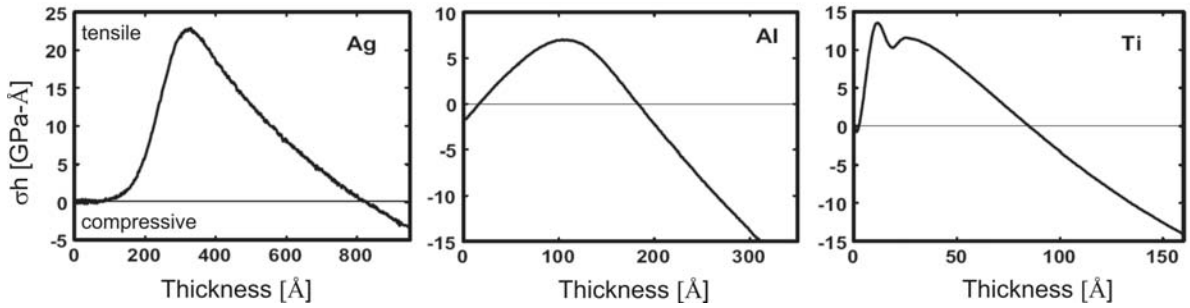

Figure 2.10: Stress-thickness vs. thickness during deposition of Ag, Al, and Ti (from Ref. [53]). All films are deposited using the electron beam evaporation technique.

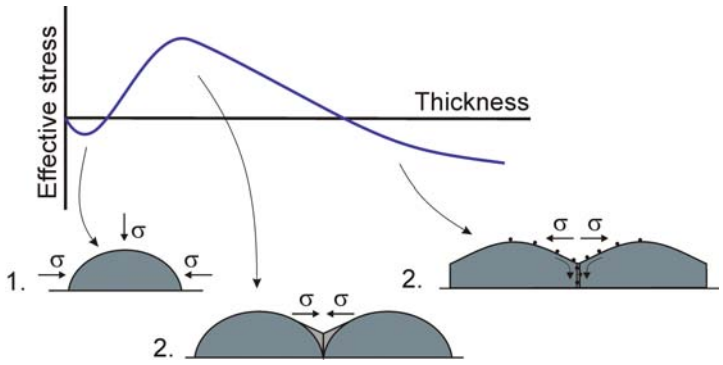

Figure 2.11: Schematic representation of the effective stress evolution versus the film thickness. Respective stress generation mechanisms are sketched.

But in general, the curve can be divided in three regions for which the following stages of film microstructure evolution are responsible (see the Fig. 2.11):

1. Compressive stress – action of the surface/interface stress on the isolated film islands [54].

   The origin of the idea lies in the observation that the lattice spacing in a small isolated island is smaller than the respective bulk value. In this case, the stress magnitude can be calculated using the following relation:

   $$\sigma = -\frac{2f}{R}\,, \tag{2.15}$$

   where f is the isotropic surface stress acting within the spherical surface of the crystallite of radius R.

2. Tensile stress – "zipping" of crystallite boundaries by formation of grain boundaries.

   As sketched in Fig. 2.11, when first contact of growing islands takes place, some

portion of the adjacent surfaces of the islands rapidly "zip" together to form a grain boundary. This process occurs due to the surface energy recovery on the cost of increasing elastic strain. The mean stress due to the "zipping", σ_{zip}, can be described as follows [53]:

$$\sigma_{zip} = \sqrt{E\frac{(1+\nu)\Delta\gamma}{(1-\nu)r_I}}, \tag{2.16}$$

where E and ν are the correspondent Young's modulus and Poisson's ratio, r_I is the radius of the crystallite at impingement and $\Delta\gamma = 2\gamma - \gamma_{GB}$ is the surface energy recovery due to the formation of a grain boundary. Since the estimate of σ_{zip} gives much larger stress magnitudes than observed experimentally, different relaxation effects may be responsible for stress mitigation. For example, as soon as the yield stress is reached in the strained crystallites, no further increase of stress takes place as dislocations begin to glide. At elevated temperatures, mechanism associated with increased surface mobility can diminish the stress assessed by the Eq. 2.16.

3. Compressive stress – incorporation of excess atoms into grain boundaries during the continued growth [55, 56].

   This is the least studied stage of stress generation. Available observations suggest that underlying mechanisms depend on the presence of grain boundaries (no compressive stress is observed during the deposition of monocrystalline materials) and on the deposition flux. According to the available models, surface supersaturation is the key thermodynamic factor that determines the steady-state stress. The observed compressive stress is induced by the migration of surface atoms into grain boundaries.

Once the films become continuous across the growth surface, no reduction of the compressive stresses is observed after the deposition interruption. Thus, the growth stresses significantly influence the final residual stress of the system. However, the stress distribution can be completely changed by time-dependent processes, such as a reduction of grain boundary area. In this process, free energy of the system is decreased by the amount of recovered grain boundary energy due to the grain growth. In the same time, tensile stress develops in the system due to the lower material density in the grain boundary regions (material have to be stretched in order to close less dense grain boundaries). Texture transformation processes, which will be described below (see Sec. 2.3.6), can also significantly affect the final stress state of the thin film system.

2.3.5 Stresses in epitaxial systems

As seen from the analysis of stresses in polycrystalline films, grain boundaries play the most important role in the stress generation. However, if the film structure evolves following the Frank-van der Merwe growth mode by nucleation of large planar grains and their subsequent coalescence, no grain boundaries are created (epitaxial films). Thus, the epitaxial systems do not follow the stress evolution scheme shown in Fig. 2.11. Instead, the epitaxial growth in heteroepitaxial systems leads to elastic lattice deformation as a result of a coherency constraint. Large mismatch stresses up to several GPa can arise in the systems with large lattice mismatch (2-3%). The lattice mismatch between film and substrate materials is the natural measure of the film strain:

$$\epsilon = \frac{a_s - a_f}{a_s}, \tag{2.17}$$

where a_s and a_f are the substrate and film lattice parameters, respectively. If the substrate is much thicker than the film, all the elastic accommodation takes place in the film material without substrate compliance. The situation in multilayer materials, where substrate and film are of the same thickness is treated in the discussion chapter of this thesis (see Sec. 6.2). Obviously, epitaxial growth leads to an increase of the systems free energy due to the elastic strain in the deposited film. As the coherent film becomes thicker, elastic strain of the film remains uniform over the growth area. Thus, the total elastic energy of the system is proportional to its volume. This increasing amount of energy drives different mechanisms of elastic strain relaxation, e.g. formation of misfit dislocations at the film-substrate interface, formation of partial dislocations or, in some cases, a change of surface morphology.

Critical thickness of a strained epitaxial film

The most common mechanism of the elastic strain relaxation is the formation of misfit dislocations on the substrate-film interface. The energy of a two-dimensional array of edge-type misfit dislocations, E_{disl}, with Burgers vector, b, and spacing, S, has the following dependence on the film thickness, h:

$$E_{disl} = \frac{\mu b^2}{4\pi(1-\nu)} \frac{2}{S} ln\left(\frac{h}{b}\right), \tag{2.18}$$

μ and ν are the shear modulus and Poisson's ratio in the substrate-film interface, respectively. As seen from this expression, the energy of an edge-type dislocation is proportional to the logarithm of film thickness. This is a much weaker dependence on thickness than the linear dependence in the case of areal density of elastic energy, E_{el}, which is derived in Sec. 2.4 to:

$$E_{el} = Bh\epsilon^2, \tag{2.19}$$

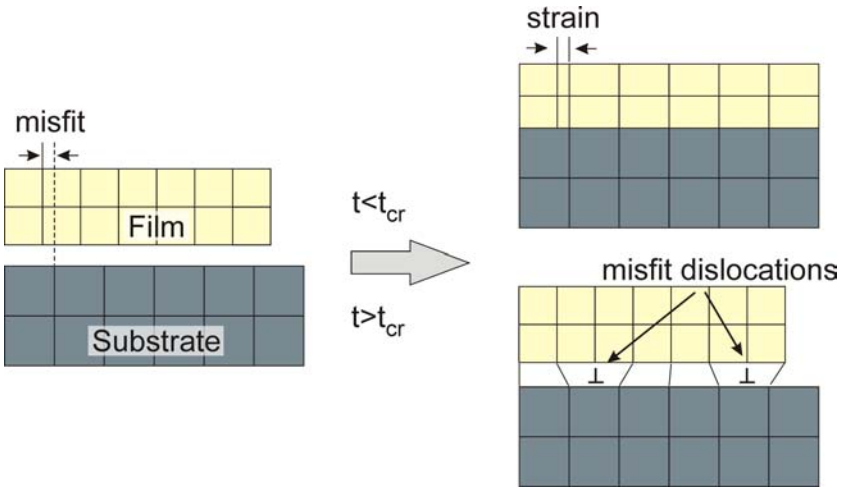

Figure 2.12: Critical film thickness for the formation of misfit dislocations.

where B is the biaxial elastic modulus. Thus, a critical film thickness must exist at which the formation of misfit dislocations is preferred over the elastic film strain (see Fig. 2.12). This thickness can be derived from the minimization of the systems free energy. As proposed by Nix [57], the total energy of a film with misfit dislocations is:

$$E_{tot} = E_{el} + E_{disl} = Bh\left(\epsilon - \frac{b}{S}\right)^2 + \frac{\mu b^2}{4\pi(1-\nu)}\frac{2}{S}ln\left(\frac{h}{b}\right) . \tag{2.20}$$

For a given film thickness, the equilibrium dislocation density can be determined by energy minimization with respect to the number of misfit dislocations per unit length:

$$\frac{\partial E}{\partial\left(\frac{1}{S}\right)} = -2Bhb\left(\epsilon - \frac{b}{S}\right) + \frac{\mu b^2}{2\pi(1-\nu)}ln\left(\frac{h}{b}\right) = 0\,, \tag{2.21}$$

or equivalently:

$$Bh\left(\epsilon - \frac{b}{S}\right) = \frac{\mu b}{4\pi(1-\nu)}ln\left(\frac{h}{b}\right) . \tag{2.22}$$

The critical film thickness, h_{cr}, is reached, when the first dislocations appear at the substrate-film interface with very large spacing ($b/S \to 0$):

$$h_{cr} = \frac{\mu b}{4\pi(1-\nu)B\epsilon}ln\left(\frac{h_{cr}}{b}\right) . \tag{2.23}$$

Using this implicit equation, the critical thickness for the dislocation formation can be assessed. For thicknesses larger than h_{cr}, the equilibrium state includes misfit dislocations, but for thicknesses lower than h_{cr}, the lowest energy is achieved by elastic strain of the lattice only. If the lattice mismatch between substrate and film materials is of about 2%, typical values of the critical thickness are in the range of 5 to 15 nm depending on the elastic properties of respective materials.

2.3.6 Texture evolution during recrystallization

During the deposition of fcc metals on amorphous substrates thin films evolve typically with <111> texture. This observation can be easily explained by the minimum surface and interfacial energies inherent to this crystallographic orientation (see Sec. 2.3.1). The <111> deposition texture is often transformed into <100> or <110> textures if the abnormal grain growth takes place in the course of the post-annealing treatment. The final texture of a film depends on dominating texture-dependent driving force, and is different for different films, substrates, and deposition conditions. Let us consider main driving forces for recrystallization:

- grain boundary area reduction;
- surface/interfacial energy anisotropy;
- elastic deformation energy anisotropy;
- other contributions like chemical driving force, magnetic energy anisotropy, temperature gradient etc. (these unsubstantial contributions may become important only in special conditions).

Grain boundary energy reduction is the fundamental cause of grain growth. In most cases it has the highest contribution to the system's free energy minimization. The correspondent driving force can reach very high values of 100-150 MPa (in the case if all grain boundary energy recovered in the initially fine-crystalline film). However, grain boundary area reduction itself can not be made responsible for the texture transformation. The choice of crystallographic orientation of growing grains is dictated by the surface/interfacial energy and the elastic energy minimization.

Due to the anisotropy of surface and interfacial energies, the change of the surface/interfacial energy per unit volume can be expressed as:

$$\Delta E_{s/i} = \frac{\sigma_1^{surf} - \sigma_2^{surf}}{h_f} + \frac{\sigma_1^{int} - \sigma_2^{int}}{h_f} = \frac{\sigma_1 - \sigma_2}{h_f} \tag{2.24}$$

where h_f is the film thickness, σ_1 and σ_2 are the sums of correspondent surface and interfacial energies, $\sigma_{1,2} = \sigma_{1,2}^{surf} + \sigma_{1,2}^{int}$, for the textures of the as-prepared and annealed states. In the case of single layer films grown on amorphous substrates, the difference of the interfacial energies for different textures can be negligible [58]. However, it may become increasingly important for multilayer systems with small periodicity.

The origin of the elastic energy can be very different depending on the specific film microstructure and nature of the substrate and film materials as well as on the environment conditions, and can lead to different recrystallization textures. Since the grain boundary migration process requires thermal activation, let us consider the elastic energy change at elevated temperatures. Elastic energy of considerable magnitude results

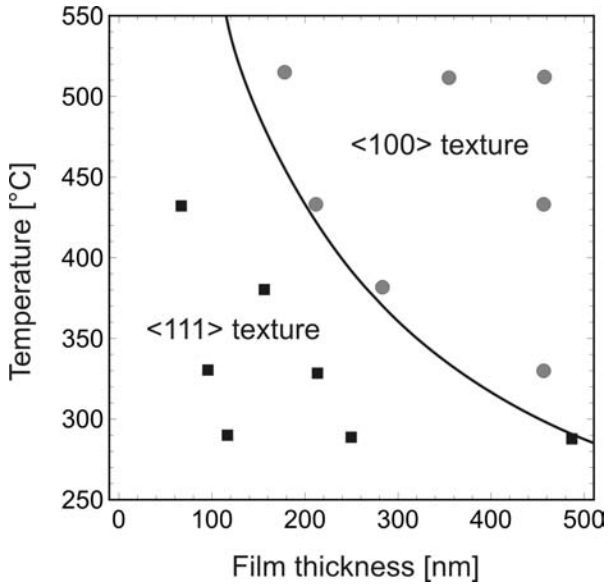

Figure 2.13: Experimentally observed texture after post-deposition annealing of Ag thin films deposited on the MgO(100) substrates. Adapted from [59].

from the difference of the thermal expansion coefficients of the substrate and film materials, $\Delta\alpha = \alpha_f - \alpha_s$. If the difference between deposition temperature and annealing temperature is ΔT, corresponding elastic strain of the film material (if substrate is much thicker than film) can be expressed as follows:

$$\epsilon = \Delta\alpha\Delta T\,. \tag{2.25}$$

For anisotropic materials orientational dependence of the corresponding biaxial moduli, B_{hkl}, takes place (see Sec. 2.4). If the biaxial modulus changes from B_1 to B_2 due to texture transformation, the corresponding change of elastic energy per unit volume of film material is

$$\Delta E_{el} = (B_1 - B_2)(\Delta\alpha\Delta T)^2\,. \tag{2.26}$$

If $\Delta E_{el} > \Delta E_{s/i}$, the recrystallization texture is governed by the minimization of the elastic energy. In fcc films grown on amorphous substrates it leads typically to the <100> texture. Grain reorientation serves in this case as an elastic energy relaxation mechanism and leads to an additional driving force component: $\Delta E_{el} - \Delta E_{s/i}$. This additional driving force can be very important, and in some cases can differentiate whether or not the recrystallization will occur [60]. In opposite case, if $\Delta E_{el} < \Delta E_{s/i}$, no texture reorientation is observed. In general, the condition for the <111> to <100> texture transformation can be written as:

$$(B_{111} - B_{100})(\Delta\alpha\Delta T)^2 > \frac{\sigma_{111} - \sigma_{100}}{h_f}\,. \tag{2.27}$$

As seen from Fig. 2.13, this result is in good agreement with experimental observations. Surface and interfacial energies dominate for small temperatures and small film thicknesses, whereas elastic energy overweights for high temperatures and high film thicknesses in correspondence with the limit line of Eq. 2.27 (solid line in the graph). The

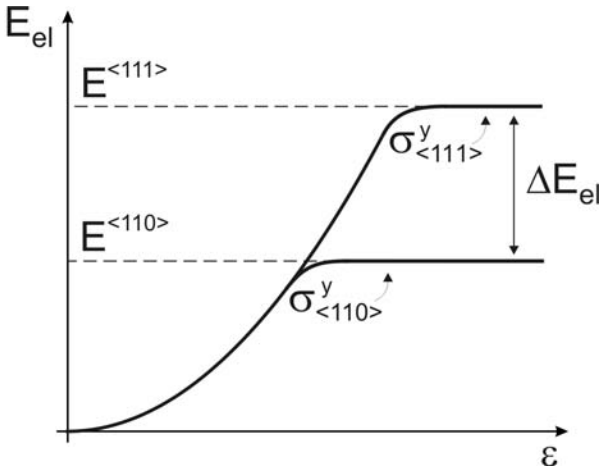

Figure 2.14: Elastic energy dependence on the respective grain orientation due to the difference of respective yield stress values.

considerations given above are valid if the lattice deformation of the film material is of elastic nature. The critical stress value (yield stress) for the initiation of plastic deformation decreases during the grain growth process following the Hall-Petch relation. Yield stress, σ_y, depends on crystallographic orientation of film grains as described in [61]. According to this dependence <110> grains have the lowest yield stress. It means that no further increase of the elastic energy takes place in the <110> grains after $\sigma_{y,<110>}$ is reached, whereas it can be increased further for other grain orientations. Therefore, <110> texture can decrease the elastic energy of the system if plastic deformation of the material takes place (see Fig 2.14). The maximum elastic energy change due to the texture transformation from <111> to <110> texture is then given by:

$$\Delta E_{el} = (\sigma_{y,<111>} - \sigma_{y,<110>})(\Delta\alpha\Delta T)\,, \tag{2.28}$$

where $\sigma_{y,<111>}$ and $\sigma_{y,<110>}$ are correspondent yield stress values for <111> and <110> oriented grains. As was proven experimentally, this mechanism works even in the case of isotropic materials such as Al [46].

2.4 Linear elasticity theory

For anisotropic materials, stress and strain are second-order tensors with nine components [62]:

$$\vec{\sigma} = \begin{bmatrix} \sigma_{xx} & \sigma_{xy} & \sigma_{xz} \\ \sigma_{yx} & \sigma_{yy} & \sigma_{yz} \\ \sigma_{zx} & \sigma_{zy} & \sigma_{zz} \end{bmatrix} ; \qquad \vec{\epsilon} = \begin{bmatrix} \epsilon_{xx} & \epsilon_{xy} & \epsilon_{xz} \\ \epsilon_{yx} & \epsilon_{yy} & \epsilon_{yz} \\ \epsilon_{zx} & \epsilon_{zy} & \epsilon_{zz} \end{bmatrix} .$$

σ_{ij} is the ith component of the force per unit area on a plane whose outward-drawn normal is parallel to the positive direction of j, as shown in Fig. 2.15. I.e., the ith component of the force, F_i, acting on the elementary area dS can be expressed as:

$$F_i = \sigma_{ij} dS_j \quad \text{(here and in the following the Einstein convention is employed).} \tag{2.29}$$

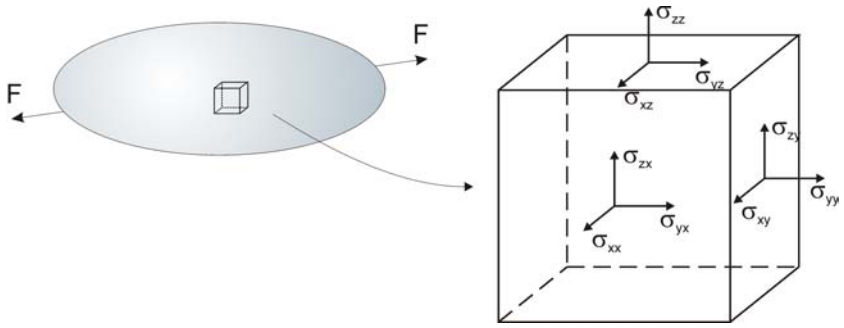

Figure 2.15: Stress distribution on an infinitesimal volume element.

Diagonal terms of the stress tensor represent normal stress components. These components tend to change the volume of the material (e.g. hydrostatic pressure, $\sigma_{xx} = \sigma_{yy} = \sigma_{zz}$), and are resisted by the materials bulk modulus. Non-diagonal terms, in turn, are the shear stress components. These components tend to deform the material without changing the volume and are resisted by the materials shear modulus. Due to the absence of torque, the following relation between stress components is valid:

$$\sigma_{ij} = \sigma_{ji}\,. \tag{2.30}$$

Thus, the stress tensor is symmetric and can be reduced to six components. The generalized Hooke's law for the three dimensional elastic body can be formulated as follows:

$$\sigma_{ij} = c_{ijkl}\epsilon_{kl}\,, \tag{2.31}$$

where c_{ijkl} is the elasticity tensor (stiffness matrix). From Eq. 2.30 and the relation $\epsilon_{kl} = \epsilon_{lk}$, it follows directly that:

$$c_{ijkl} = c_{jikl} = c_{ijlk} = c_{jilk}. \tag{2.32}$$

Besides the elastic stiffness matrix, the compliance matrix, $s_{ijkl} = c^{-1}_{ijkl}$, is commonly used:

$$\epsilon_{ij} = s_{ijkl}\sigma_{kl}. \tag{2.33}$$

The elastic energy density of the strained material is given by the following expression:

$$E_{el} = \int \sigma_{ij} d\epsilon_{ij} = \frac{1}{2}\epsilon_{ij}\sigma_{ij}. \tag{2.34}$$

The elastic coefficients are often written in a contracted matrix notation (Voigt notation), in which pairs of indices are substituted by single numbers ($c_{ijkl} = c_{mn}$) in the following way:

11	→	1
22	→	2
33	→	3
23 and 32	→	4
13 and 31	→	5
12 and 21	→	6

Due to the mentioned symmetry of strain and elasticity tensors, the generalized Hooke's law in Voigt notation can be represented as follows:

$$\begin{bmatrix}\sigma_{11}\\ \sigma_{22}\\ \sigma_{33}\\ \sigma_{23}\\ \sigma_{31}\\ \sigma_{12}\end{bmatrix} = \begin{bmatrix}c_{11} & c_{12} & c_{13} & c_{14} & c_{15} & c_{16}\\ c_{12} & c_{22} & c_{23} & c_{24} & c_{25} & c_{26}\\ c_{13} & c_{23} & c_{33} & c_{34} & c_{35} & c_{36}\\ c_{14} & c_{24} & c_{34} & c_{44} & c_{45} & c_{46}\\ c_{15} & c_{25} & c_{35} & c_{45} & c_{55} & c_{56}\\ c_{16} & c_{26} & c_{36} & c_{46} & c_{56} & c_{66}\end{bmatrix} \begin{bmatrix}\epsilon_{11}\\ \epsilon_{22}\\ \epsilon_{33}\\ \gamma_{23}\\ \gamma_{31}\\ \gamma_{12}\end{bmatrix} \tag{2.35}$$

Notice that in reduced scheme $\gamma_{ij} = 2\epsilon_{ij} (i \neq j)$ are used instead of the ϵ_{ij}. Due to the high degree of symmetry of the cubic crystal lattice, the stiffness matrix is reduced to the following form with only three independent components (c_{11}, c_{12}, and c_{44}):

$$c_{mn} = \begin{bmatrix}c_{11} & c_{12} & c_{12} & 0 & 0 & 0\\ c_{12} & c_{11} & c_{12} & 0 & 0 & 0\\ c_{12} & c_{12} & c_{11} & 0 & 0 & 0\\ 0 & 0 & 0 & c_{44} & 0 & 0\\ 0 & 0 & 0 & 0 & c_{44} & 0\\ 0 & 0 & 0 & 0 & 0 & c_{44}\end{bmatrix} \tag{2.36}$$

Elastic energy due to the equibiaxial mismatch strain (epitaxy constraint)

Coherent growth of lattice mismatched materials is accompanied by elastic lattice deformation (see Sec. 2.3.5). The expression for the elastic energy of a strained film can be drawn using the relations between stress and strain given above in this section. To avoid complexity of expressions let us concentrate on the case, in which the strain is parallel to cubic lattice axes, i.e. for a film with the [001] crystallographic direction perpendicular to the interface plane. Due to the symmetry of the cubic lattice, the in-plane strain of materials in contact is of equibiaxial nature:

$$\epsilon_{11} = \epsilon_{22} = \epsilon\,. \tag{2.37}$$

For the chosen film orientation, only normal stress components exist. According to Eq. 2.35 and stiffness matrix 2.36 for cubic crystal, they are given by following equations:

$$\sigma_{11} = \sigma_{22} = (c_{11} + c_{12})\epsilon + c_{12}\epsilon_{33}\,; \tag{2.38}$$

$$\sigma_{33} = 2c_{12}\epsilon + c_{11}\epsilon_{33}\,. \tag{2.39}$$

If no traction is applied along the z direction, the left part of Eq. 2.39 equals zero, and the out-of-plane strain (ϵ_{33}) can be expressed via the in-plane strain (ϵ):

$$\epsilon_{33} = -\frac{2c_{12}}{c_{11}}\epsilon\,. \tag{2.40}$$

From Eqs. 2.38 and 2.40 normal in-plane stresses are derived:

$$\sigma_{11} = \sigma_{22} = \frac{c_{11}^2 + c_{11}c_{12} - 2c_{12}^2}{c_{11}}\,\epsilon\,. \tag{2.41}$$

The combination of elastic constants is usually called biaxial elastic modulus, B^{hkl}:

$$B^{001} = \frac{c_{11}^2 + c_{11}c_{12} - 2c_{12}^2}{c_{11}}. \tag{2.42}$$

Now the elastic energy density of the in-plane strained film can be calculated according to Eq. 2.34:

$$E_{el}^{001} = \frac{1}{2}(\sigma_{11}\epsilon + \sigma_{22}\epsilon) = B^{001}\epsilon^2\,. \tag{2.43}$$

In the same way, the elastic energy density of the film with arbitrary orientation can be derived:

$$E_{el}^{hkl} = B^{hkl}\epsilon^2\,. \tag{2.44}$$

Chapter 3

Experimental methods

3.1 Introduction to field ion microscopy (FIM) and tomographic atom probe (TAP) methods

The Field Ion Microscopy (FIM) was introduced in 1951 [63] and almost entirely developed by E.W. Müller and his co-workers. The FIM was the first instrument capable of imaging conducting surfaces with atomic resolution in real space. This technique was originally established to solve problems in the fields of surface physics, crystallography and physical metallurgy. After supplementation by the atom probe mode, owing to its high resolution chemical analysis, the field of application of this method was considerably widened. However, early analytical instruments were equipped with a single time-of-flight detector to perform a one-dimensional analysis along cylindrical shaped volume of only a few nanometers in diameter. Taking into account the comparably small amount of counted atoms, the statistical significance of the data was very limited. This situation has changed by introduction of position sensitive detectors, which allowed to improve the statistical significance by registering atoms from a much larger specimen volume and to achieve high lateral resolution. The first position-sensitive atom probe was developed by A. Cerezo [64] in the end of the 80s. It featured a wedge-and-strip anode detector. Since then a variety of position-sensitive atom probes with different detector structures (optical, multianode array, delay-line detectors) have been developed improving the lateral resolution of ion detection. The most recent important step in the development of atom probe technique was the introduction of a laser assisted evaporation, enabling to measure semiconducting and even insulating materials, which is almost impossible with conventional high voltage pulse evaporation. Nowadays, almost all kinds of crystalline solids, glasses and even some biological materials can be measured by the state of the art atom probe technique. Though, some restrictions regarding the specimen preparation exist (special needle-like sample geometry with curved surface), this method becomes increasingly important for the nanocharacterization for both scientific and industrial purposes. Atomic resolution achieved by FIM already in 1956 is no longer unique to the method, but no other experimental method revealing atomic reso-

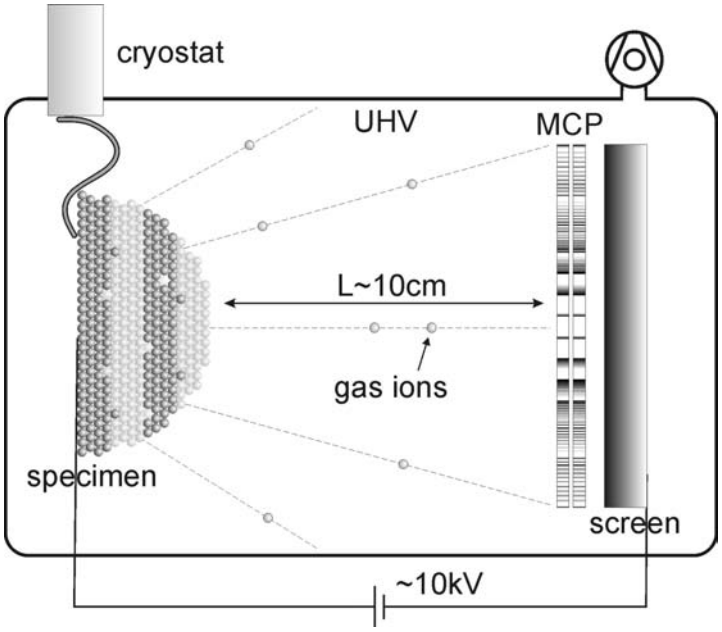

Figure 3.1: Schematic drawing of a field ion microscope.

lution (high resolution electron microscopy (HREM) or scanning tunneling microscopy (STM)) yields an atomic chemical sensitivity combined with 3D reconstruction inherent to the TAP method. This capability allows to carry out a nanoanalysis of the initial interdiffusion stages in magnetic multilayers consisting of alternating Co and Cu layers in which the typical diffusion zone thickness does not exceed 1 nm.

3.2 FIM

The basic principle of image formation in the FIM differs considerably from those of optical and electron microscopes and is remarkable for its simplicity. The image is produced by applying a high voltage to the specimen with respect to a phosphor screen in the presence of the so-called imaging gas (He, Ne, Ar, H_2 or their mixtures). The specimen is formed as a fine wire or needle with an extremely small apex curvature radius (R≈10-50nm). This geometry is needed to obtain enormous electric fields in the order of some tens of GV/m. The field in the vicinity of the specimen apex may be calculated using the following formula:

$$E = \frac{U}{\beta R}, \tag{3.1}$$

where U is the applied voltage, R is the radius of the spherical (approximation) specimen apex and β is an instrument and sample geometry dependent constant ($\beta \approx 7$). The specimen is mounted on a cryostat and connected to a high voltage lead inside the

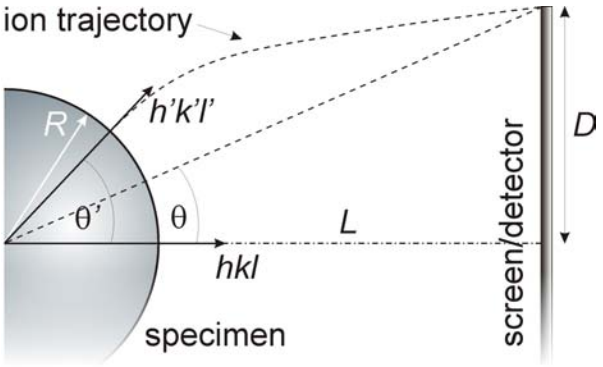

Figure 3.2: Schematic diagram of the FIM/TAP geometry for the determination of the magnification and image compression factor.

vacuum chamber with a residual pressure of 10^{-7} Pa (Fig. 3.1). During the operation, the tip is kept at a temperature of 10-100 K in an imaging gas atmosphere with a pressure of about $5 \cdot 10^{-3}$ Pa. The imaging system of the FIM consists of a single or a chevron type microchannel plate (MCP), which increases the signal of the oncoming ions, and a phosphorous screen situated at the distance of 5 to 15 cm from the specimen.

By the application of a high positive potential to the specimen, gas atoms become polarized by the inhomogeneous electric field and are drawn towards the apex of the tip. By inelastic collision with the tip, the polarized atoms are cooled down to the tip surface temperature and are trapped in a region of approximately 0.5 nm width above the tip surface (see Fig. 3.3). In this region, the energy of the electrons is below the Fermi level of the metallic specimen and tunneling is prohibited, so the atoms in this zone can not become ionized (this region is also called forbidden zone and the atoms, which are caught there, are called field adsorbed atoms). At distances much higher than x_c (see the Fig. 3.3), the probability of ionization also decreases. Thus, at sufficiently high electric fields, ionization occurs only in a narrow ionization zone at the distance x_c from the tip surface. The phenomenon of field ionization is a key process for the field ion microscopy. It was predicted theoretically already in 1928 by Oppenheimer. The voltage required for electron tunneling is proportional to the apex radius of the specimen and is typically between 2 and 15 kV to achieve a field of up to 60 V/nm (60 GV/m!) in the vicinity of the sample apex. The resulting positively charged gas ions are repelled and move along the trajectories schematically depicted in Fig. 3.2 towards the imaging system. The magnification of the FIM is estimated by the relation:

$$M = \frac{\kappa L}{R}, \tag{3.2}$$

where L and R are the distance from the tip to the screen and the tip apex radius, respectively, κ is an image compression factor of approximately 0.6 accounting for the curvature of ion trajectories towards the cathode (screen or position sensitive detector). This constant may be defined as the ratio of the aperture angle, θ, defined by the size of screen/detector, D, and the distance L to the angle, θ', between two crystallographic directions or poles, one in the center of the micrograph (hkl) and the other on its edge $(h'k'l')$ (see Fig. 3.2).

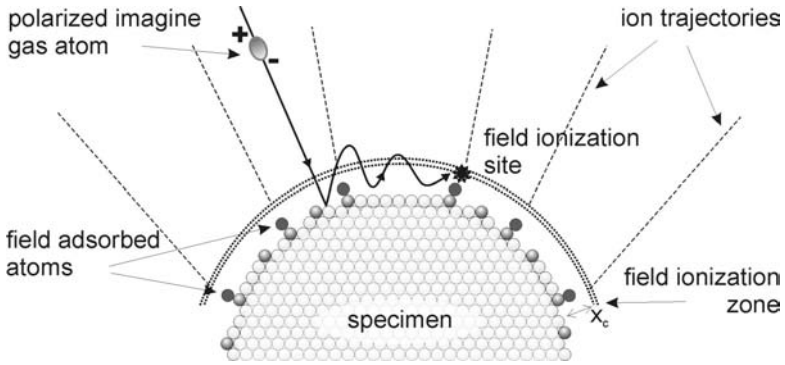

Figure 3.3: Schematic drawing of the field ionization process of gas atoms over the high field regions of the hemispherical tip surface. Atoms at the ledges and kinks are shaded.

After impinging on the surface of the MCP, the incoming gas ion generates a cascade of secondary electrons, which illuminate the phosphor screen. A few thousand of gas atoms per second must be ionized at the same site of a surface atom in order to produce an observable image on the phosphorous screen. For a hemispherically shaped tip, the surface atoms located on the ledges or kinks protrude from the surface. The tunneling probability of electrons from the gas atoms to the most prominent surface atoms located at these sites, and hence the gas atom ionization probability, is very high with the result that these surface atoms are imaged with much higher brightness. The topographical relief formed by the protruding atoms produces the contrast in the FIM image. The intersection of each stack of *hkl* atomic layers with the hemispherical tip envelope gives rise to an image consisting of several systems of concentric rings. The geometrical arrangement of this structure explains the well known crystallographic pattern of FIM images. If the image is formed from a single crystal, atomic layer edges of several pole directions are visible in a single FIM image (in Fig. 3.4a, a tungsten sample is shown). Some attempts have been made to fit the FIM image to a standard crystallographic projections, e.g. orthographic, gnomonic, stereographic or some intermediate projection relationships. Because of the complexity of ion trajectories, no projection method was found which precisely describes the positions of poles in the FIM image. In the outer regions, the trajectories are influenced by the specimen shank, compressing the image stronger than in the apex vicinity. The exact configuration of the poles depends also on the individual geometry of a microscope. The stereographic projection provides a good fit to the image for small angles from the specimen axis (compare Fig. 3.4a and b), therefore it is routinely used for crystallographic purposes. The projection method is a key point in tracing the ion trajectories back during the TAP data reconstruction, which will be described below in this chapter.

In the former time, ball models of the specimen apex were used to interpret the observed FIM images. Nowadays, a computer simulation can help with this task. The easiest model can be created by cutting a spherical slice from the generated lattice of a given structure and projecting it on a viewing plane in the given crystallographic direction.

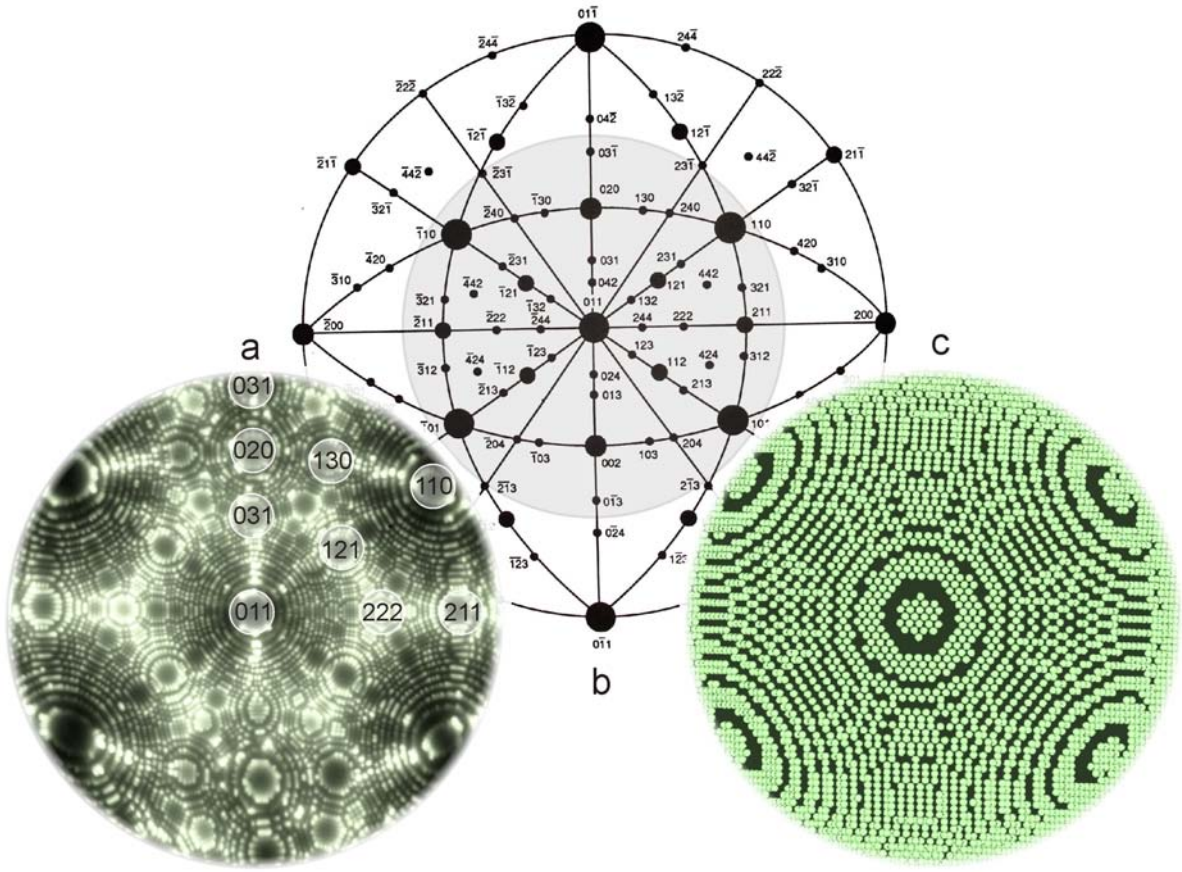

Figure 3.4: (a) Micrograph of <011> tungsten specimen (curvature radius at the apex - 28 nm); (b) Standard (011)-stereographic projection (shaded region corresponds to the FIM image area); (c) Simulated ball model image of a <011> tungsten tip (curvature radius at the apex - 10 nm).

This method is called "thin shell" model. Such simulations are very helpful in demonstrating the formation of FIM images and in their interpretation by direct comparison of the pattern. In Fig. 3.4c, such a simulated FIM micrograph of bcc lattice with [110] direction in the middle is depicted. Though the orthographic projection was used, one can see a good resemblance to the real FIM image of [110] tungsten shown in the Fig. 3.4a. One can improve the simulation model by determining the number of nearest neighbors for each atom and correlating it to the intensities in the image to produce a better match. One can also calculate the electrical field around the tip surface and choose the atoms in the vicinity of which the field reaches some given value for image formation. The last method gives the best accuracy and can also be used for the field desorption image formation by computing the trajectories of the evaporated ions. The computer models are very flexible, allowing to generate the images in any crystallographic direction, visualize lattice defects, solid solutions and multi-phase materials.

If the electric field is raised to a sufficiently high value, material may be removed from

the surface by field induced desorption [1]. The most prominent surface atoms are ionized and removed in this process, allowing time-of-flight (TOF) mass spectrometry. The threshold field-strength for evaporation is a function of the sublimation energy of the specific atoms and is therefore a material parameter, known as the evaporation field-strength. The process of field induced desorption can be followed on the imaging screen because it occurs in general at slightly higher field strengths than those required for ionization of the imaging gas (this field strength is referred to as the best image field (BIF)). As the evaporation field can vary substantially from material to material (e.g. Al - 19 V/nm, W - 57 V/nm), different imaging gases are used having the suitable BIFs (He - 44 V/nm, Ne - 38 V/nm, Ar and H_2 - 22 V/nm) for best specimen imaging. It is important that the BIF of correspondent imaging gas is close to the evaporation field of the specimen material. If the BIF is substantially higher, no image will be produced while evaporating the specimen material, if the BIF is much lower, the image might be too bright with no details seen. The process of field evaporation has some important advantages which are used to obtain better FIM images and to prepare substrates for thin film deposition:

1. Continuous field evaporation removes asperities and protrusions from the surface of a newly prepared tip making its shape nearly hemispherical.

2. Any oxide films or field adsorbed contaminant layers on the surface can be removed from the specimen surface in a controllable manner.

The combination of FIM with TOF mass spectrometry gives rise to atom probe field ion microscopy (APFIM). This technique allows chemical identification of single atoms that have been field-evaporated from the tip surface. By that, one can obtain one-dimensional depth composition profiles but no information about distribution of different constituents within an atomic layer. This limitation has been overcome by the development of position-sensitive detectors (PSD), which enabled three-dimensional atom probe tomography described in the next section. To summarize the description of the FIM technique, the by no means complete list of versatile application fields is given:

- Atomic resolution imaging of pure metals and alloys, some semiconducting and ceramic materials;

- Imaging of some organic and biological materials;

- Investigation of lattice defects, microstructural features and surface thermodynamics;

- Surface diffusion study;

- Crystallography tasks;

[1] The term field evaporation is also used in the literature, having the same meaning as the field desorption.

- Investigation of high electric field phenomena occurring at the specimen surface (the achieved electric field of some tens of GV/m can not be obtained by other man-maid techniques);
- Specimen development for TAP investigations (atomically clean surfaces with well-defined end-form are prepared, which can also be used as substrates for the investigation of thin films);
- Prescreening of the specimens to select the initial area for TAP analysis;
- As the viewing area in FIM is as a rule larger than that of TAP, it is usually used for TAP results checking;
- It is also used as the tool for obtaining geometric parameters of the specimens needed for volume reconstruction of TAP data.

3.2.1 Tip radius determination

Here it will be briefly explained how the FIM images can be used to estimate the geometric parameters of the imaged tip. The curvature radius of tip apex can be determined from the arrangement of the concentric rings. It can be done by counting the number of rings (atomic terraces) between two crystallographic poles with known Miller indices (see Fig. 3.5). The angle α between the hkl and $h'k'l'$ crystallographic direction in a cubic lattice is given by

$$\alpha = arccos\left(\frac{hh' + kk' + ll'}{\sqrt{h^2 + k^2 + l^2} \cdot \sqrt{h'^2 + k'^2 + l'^2}}\right) . \tag{3.3}$$

Then the local radius of the sample near the poles is determined as follows:

$$R = \frac{nd_{hkl}}{1 - cos(\alpha)} , \tag{3.4}$$

where n is the number of hkl planes between the poles, the other parameters are defined as shown in the Fig. 3.5. To determine the radius more accurately, it should be averaged

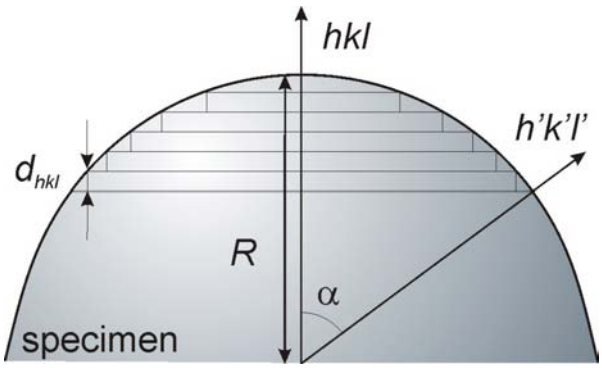

Figure 3.5: Schematic diagram of the FIM specimen for the tip apex curvature radius determination.

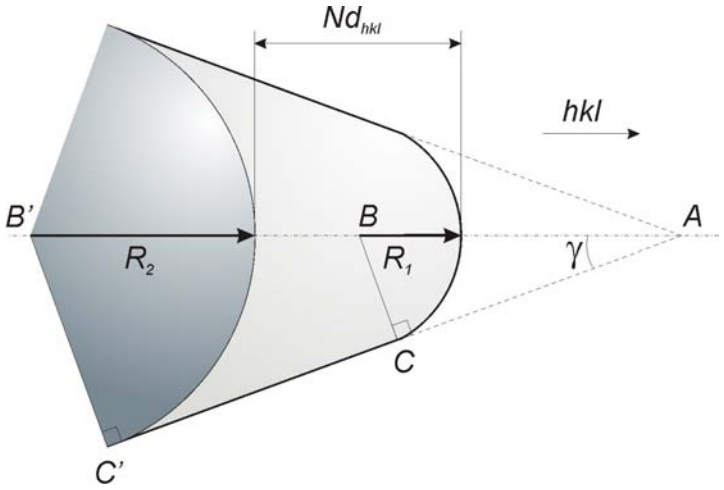

Figure 3.6: Schematic diagram for estimation of the average shaft angle from a controlled field evaporation.

from several calculations between different pole pairs. Knowing the tip radius at different voltages, one can calculate the parameter β from Eq. 3.1. The tip radius is one of the parameters needed for the volume reconstruction procedure of inhomogeneous thin film specimens, which will be described in Sec. 3.3.2.

3.2.2 Shaft-angle estimation

The average shaft angle, γ, of the specimen can be determined by taking the image of the sample with some apex curvature radius, R_1, evaporating a known number of the atomic terraces on the middle pole and taking the second picture in order to determine the final radius of the sample, R_2. In Fig. 3.6, the corresponding schematic diagram is depicted. From the two similar right-angled triangles, ABC and $AB'C'$ one can derive the following expression for the shaft angle calculation:

$$\gamma = arcsin\left(\frac{R_2 - R_1}{R_2 - R_1 + Nd_{hkl}}\right), \tag{3.5}$$

where N is the number of evaporated atomic planes in the hkl direction and d_{hkl} is the corresponding interplanar spacing. Along the tip radius the shaft angle is also an important parameter for the data reconstruction algorithm used for the reconstruction of the inhomogeneous thin film specimens. Determined in the described manner, values of shaft angle and tip radius have to be corrected to achieve the proper data reconstruction, since the shape of the tungsten tip coated with material usually does not mimic the shape of the as developed tungsten tip. Notwithstanding, it can be very helpful to have the first approximation of the shaft angle and initial radius values as a starting point for the data reconstruction procedure.

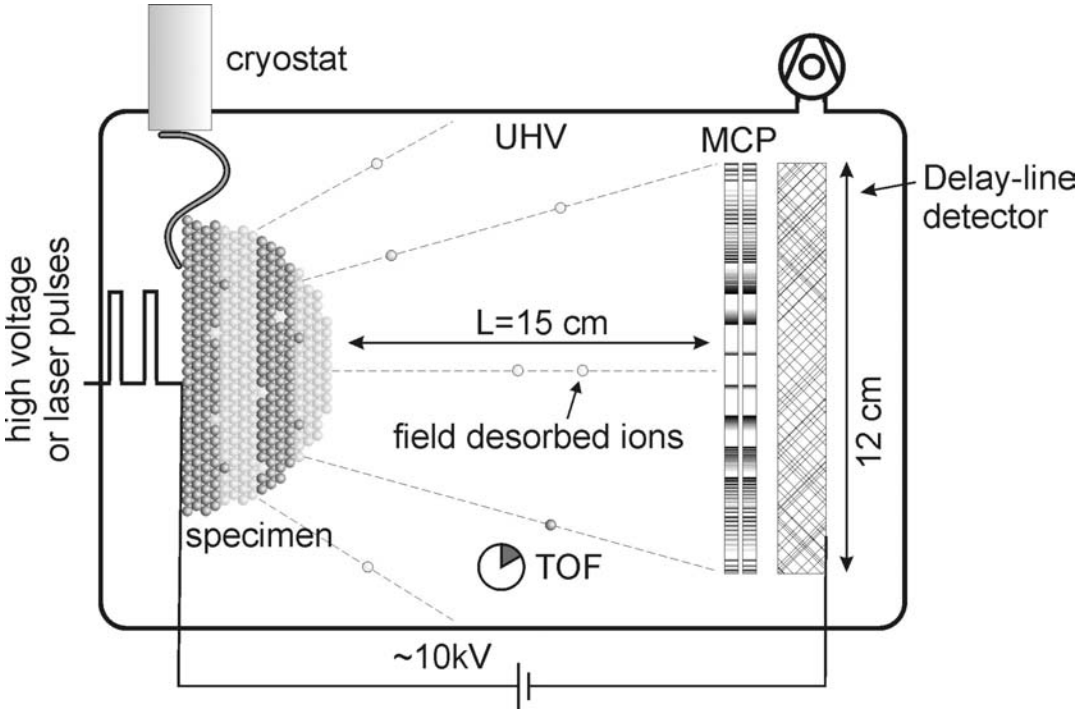

Figure 3.7: Schematic drawing of a laser assisted wide angle tomographic atom probe.

3.3 TAP

The three-dimensional atom probe is a combination of FIM, TOF mass spectroscopy and position sensitive detector (PSD). A schematic drawing highlighting the functional principles is shown in Fig. 3.3. It resembles to a great extent those of the FIM (compare to Fig.3.1). The main difference is that field desorbed ions of the specimen material are detected by means of PSD, instead of the imaging gas ions, producing the image in the FIM. The field evaporation occurs in controllable manner by applying high voltage pulses (or laser pulses in laser assisted mode) to the specimen. Several types of 3D atom probes exist, which are distinguished by the constituent PSD system [65]. Here, only the 3D atom probe type used at the Institute of Material Physics in Münster is introduced briefly. The picture and the drawing of the instrument are shown in Fig. 3.8. The presence of a lock chamber and a roomy storage chamber (about 60 specimens can be stored simultaneously), enables a high measurement throughput. All chambers are isolated by plate valves and pumped independently by turbo molecular pumps. Central control logics ensures failure free interaction of the vacuum pumps, electronic units and controls in the system. The instrument is a successor of the TAP at the University of Göttingen [66] having the following remarkable improvements:

1. Delay-line detector system [67];

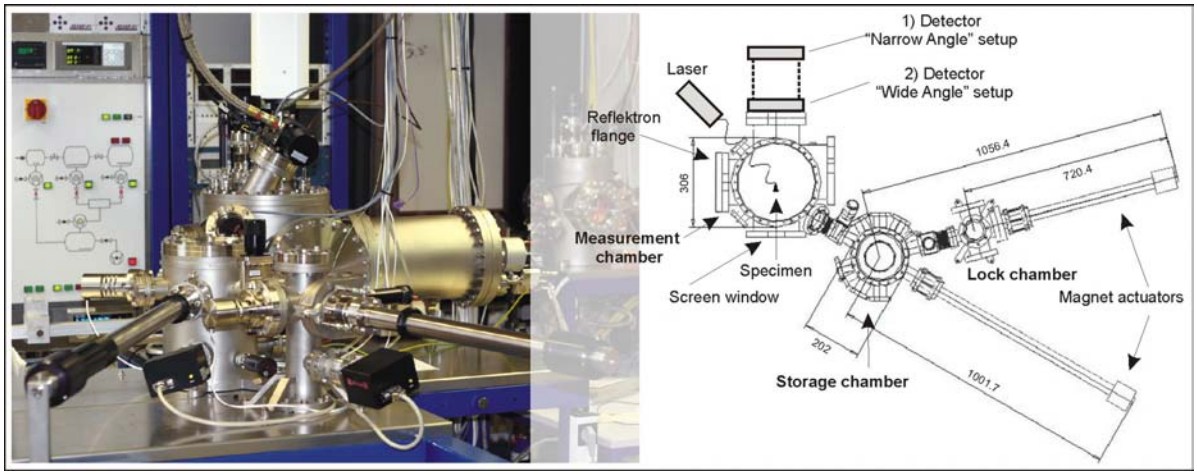

Figure 3.8: Laser assisted wide angle tomographic atom probe (LAWATAP) in the Institute of Material Physics in Münster.

2. Wide-angle measurement geometry (WATAP);

3. Laser-assisted evaporation mode (LATAP [2]). LATAP in Münster is described in [68].

The delay-line detector (DLD) system used in the LAWATAP provides multi-event detection of ions and enhanced lateral resolution (even inclined to the specimen axis atomic planes in tungsten can be detected) enabling a fast and reliable data acquisition process. The DLD system mounted on the vacuum flange of the measurement chamber is shown in Fig. 3.9. The detector system consists of a chevron type MCP, which is mounted in front of the DLD. The field evaporated atoms hit the MCP and produce electron clouds which serve as a signal for time-of-flight (TOF) measurement. The specific mass to charge ratio, which can be assigned to measured atomic species is determined from the TOF and applied voltage. During the field evaporation, the potential energy of the ion on the surface, $ne(U_{base} + \alpha U_{pulse})$, is converted to kinetic energy, $mL^2/2t^2$. This condition gives the relation for the mass to charge ratio:

$$\frac{m}{n} = 2e(U_{base} + \alpha U_{pulse})\frac{t^2}{L^2}, \tag{3.6}$$

where m and n are the mass and charge of an ion, respectively, and e is the electron charge. U_{base} and U_{pulse} are the base and pulse voltages, α is a so-called pulse efficiency factor, t is the time of flight and L the distance between sample and detector. The mass resolution of the instrument is better than 1/200 (the four major isotopes of tungsten are observed with minor overlapping). Parallel to the TOF spectrometry, the position of impingement of the electron cloud ($\approx 10^6$ electrons) onto the delay-line detector is determined. The functioning principle of the DLD is based on that of lecher lines [69].

[2] LAWATAP acronym is used for LATAP with the wide angle geometry.

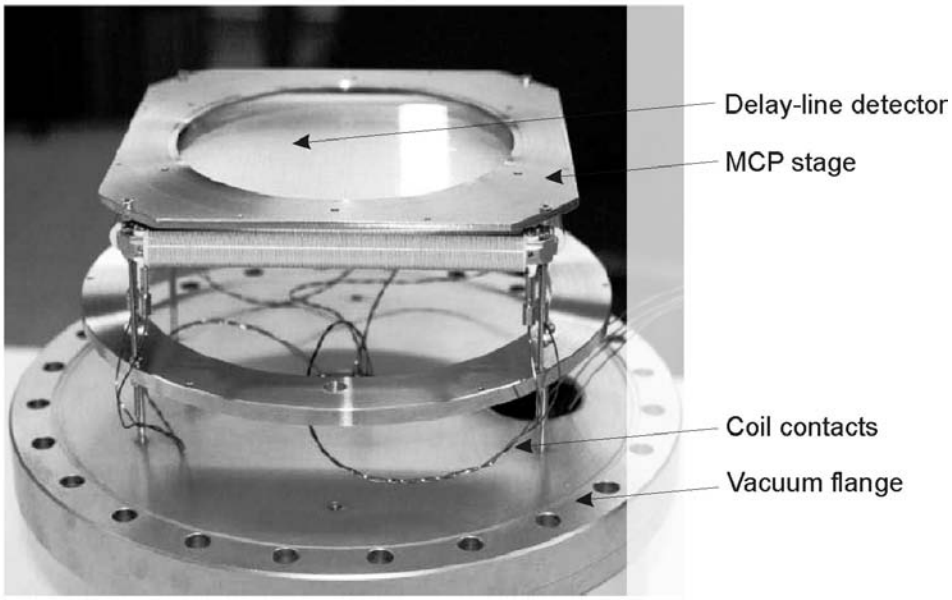

Figure 3.9: Roentdek delay-line detector mounted on the vacuum flange. MCP is removed to provide better detector view.

It consists of two perpendicular (x and y) coils which register the electric pulse produced by the electron cloud (see Fig. 3.10). This pulse propagates with the velocity of light in both directions in the x and y coils. One can calculate the velocity, v, at which the signal propagates along the x and y directions knowing the geometry of the coils. A high precision clock measures the times of signal propagation to both ends of the wire (four different values). The difference in propagation time is proportional to the x and y coordinates:

$$x = \frac{t_{x1} - t_{x2}}{v_x}, \qquad y = \frac{t_{y1} - t_{y2}}{v_y}, \tag{3.7}$$

where v_x and v_y are the propagation velocities of the signal along the x and y directions. The center of the detector has coordinates (0;0), since in the center the time values in the following pairs: t_{x1} and t_{x2}, t_{y1} and t_{y2} are equal. The sum of each pair of times, t_x and t_y, are constant values. These constants are used for assigning of signals in case of multiple ions hitting the detector simultaneously and for the purpose of noise filtering and reconstruction of missing signals. The detector system of the LAWATAP in Münster is located at a distance of only 150 mm from the tip apex without loosing the mass resolution of the device (both positions of the detector are shown on the drawing in Fig. 3.8). By that, the detection area of the specimen was increased by a factor of 5-6 compared to the conventional TAP (longer flightpath), as it is sketched on the Fig. 3.11. If in conventional TAP the typical tungsten measurements contained about $0.5 \cdot 10^6$ atoms in a volume of $1.5 \cdot 10^4\,\mathrm{nm}^3$ (for a measurement depth of 100 nm), WATAP measurement of the same depth contains about $3 \cdot 10^6$ atoms having the volume of about $10^5\,\mathrm{nm}^3$ (for aluminium, which has very low evaporation field strength a data set of the same depth may contain $15 \cdot 10^6$ atoms). Tab. A.2, A.3, A.4 and A.5 give

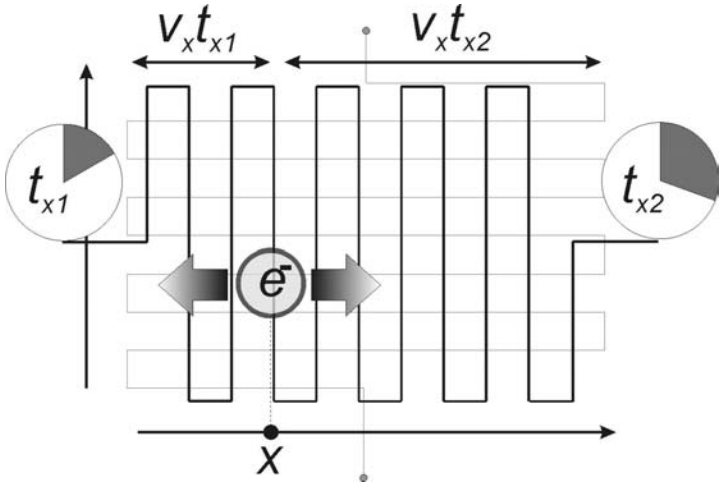

Figure 3.10: Schematic drawing of a delay-line detector.

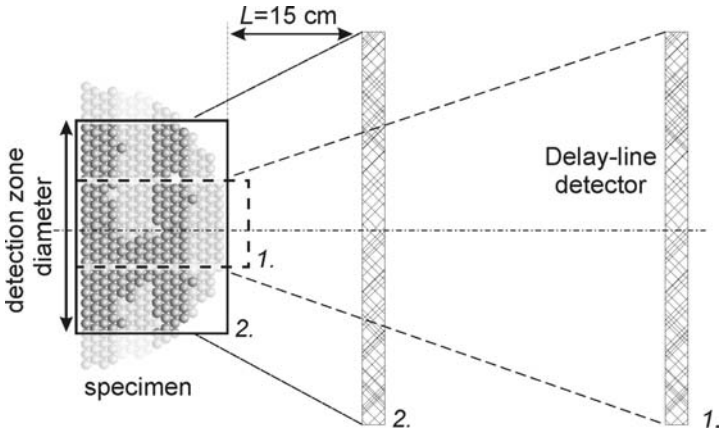

Figure 3.11: Point projection implies the increase of the measurement area by decreasing the detector to specimen distance (1 - conventional TAP; 2 - WATAP).

Flight path:	150 mm
Aperture half angle:	35°
Image compression factor, κ:	0.6
Detection efficiency, η:	0.5
Delay-line detector diameter:	120 mm
Detection zone diameter:	up to 40-100 nm[a]
Max. tip voltage:	16 kV
Electric pulse	
-max. voltage:	5 kV
-width:	7 ns
-frequency:	25 kHz
Laser pulse	
-energy:	15 μJ
-width:	500 ps
-frequency:	1.5 kHz
Background pressure:	10^{-8} Pa
Minimum specimen temperature:	≈30 K

Table 3.1: Technical data and important parameters of the LAWATAP at the Institute of Material Physics in Münster

[a]The detection zone diameter of 100 nm or more can be reached in special conditions for materials with low evaporation field, e.g. aluminum, at high applied voltages.

the estimate of the tip radius, detection diameter (see in Fig. 3.11) and detected atoms per nm depth for the whole range of applied voltages for tungsten, cobalt, copper and aluminum, respectively. The larger viewing area enables better statistics and better identification of the measured microstructural and morphological features (compare the measured volumes 1 and 2 in Fig. 3.11). Faceting of thin films deposited on the curved W-tip substrate, occuring after the thermal treatment, observed in this work for the first time, was only possible to observe due to the large detection zone covering different crystallographic directions on the specimens surface. As nanoscale material interactions in polycrystals are greatly influenced by the presence of grain boundaries (GB), it is always an exciting task to detect GBs in the reconstructed volume. The LAWATAP gives the possibility to detect grain boundaries in almost each measurement. Even though a big grain is usually formed in the apex area of the specimen, its dimensions are smaller than the measured area, which was not the case for conventional TAP.

The important technical data specifying the 3D atom probe at the Institute of Material Physics in Münster are compiled in Tab. 3.1.

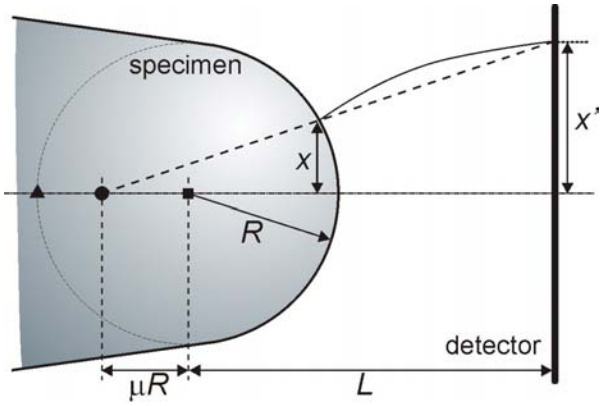

Figure 3.12: Ion trajectory approximation by a point projection ($\mu \approx 0.67$). Projection points of stereographic and gnomonic projections are marked by the triangle and square, respectively.

3.3.1 Volume data reconstruction

To reconstruct the measured volume from the TAP data, the trajectories of the ions have to be calculated back to the original positions in the specimen. Typically, the data set consists of N lines (for the N atoms) in each of which the information for a single measured atom is given. The minimal content of each data line is the following: x' and y' positions on the detector, applied base and pulse voltage, TOF. It would be impossible to simulate all the trajectories of typically 10^7 atoms from the local field distribution near the sample routinely. Instead, x and y coordinates are determined straightforward by projecting the detector coordinates onto the spherical tip surface. The best projection is achieved by a point projection with the projection focus placed μR behind the center of the specimens apex (which is fitted by a sphere) as it is sketched in the Fig. 3.12, where μ is defined by the relation: $1/\kappa - 1$ [70] and equals 0.67 ($\kappa = 0.6$). This projection is intermediate to the stereographic and gnomonic ones, the focuses of which lie on the rear side of the apex sphere and in its center, respectively. The x and y coordinates of the atom on the specimen surface can be determined using the detector impact coordinates, x' and y' and the magnification factor, M, which is defined by Eq. 3.2 as follows:

$$x = \frac{x'}{M}; \qquad y = \frac{y'}{M}\,. \tag{3.8}$$

For the volume reconstruction of measured data it is also necessary to determine the z coordinate:

$$z = z' + z_{tip}\,. \tag{3.9}$$

The first term in this equation accounts for the shift of the tip front during the evaporation of N atoms and the second term accounts for the shift needed to place the atom

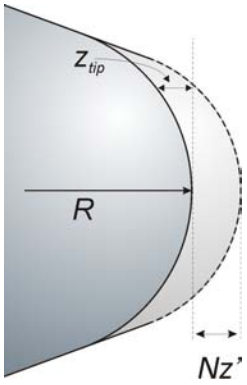

Figure 3.13: Drawing for the calculation of the z coordinate of the atom in the volume reconstruction. Nz' is the shift of the tip front after evaporation of N atoms.

onto the spherical tip surface (see Fig. 3.13):

$$\frac{dz'}{dN} = \frac{\Omega M^2}{\eta A}; \tag{3.10}$$

$$z_{tip} = R - \sqrt{R^2 - \frac{\sqrt{x'^2 + y'^2}}{M}}, \tag{3.11}$$

where Ω is the atomic volume, η is the detection efficiency (the factor, which defines the fraction of detected ions), A is the detector area and R is the tip apex curvature radius, which is calculated from the Eq. 3.1.

3.3.2 TAP analysis of inhomogeneous thin film specimens

Atom probe tomography has become a well-established tool proven to yield reliable analysis data in many examples, where small precipitates are embedded in a matrix element. However, in most cases, precipitates smaller than the analyzed volume or very thin segregation zones have been investigated, which have only a minor influence on the evaporation of the specimen tip. Compared to the microstructure of such samples, layered thin film specimens are heterogeneous on a much coarser scale, which becomes particularly noticeable in the case of layer materials that are distinguished by a pronounced difference in the evaporation field strength. Several limitations arise in the preparation of layered film specimens in order to carry out successful measurements and to calculate a reliable volume reconstruction. During the measurement, the evaporation rate is kept constant by computer controlled voltage adjustment. Very fast evaporation may destroy the specimen but too small evaporation rates increase the noise level in measurements and increase the time of data acquisition. If a material of high evaporation field strength is deposited on top of a material of lower field strength, the specimen becomes unstable when the interface is reached. As soon as the easily evaporating material becomes uncovered, the data rate increases dramatically. Often, computer controlled voltage adjustment can not compensate this increase of flux rate fast enough, resulting in fracture of the specimen. Thus, the deposition of the layer materials should

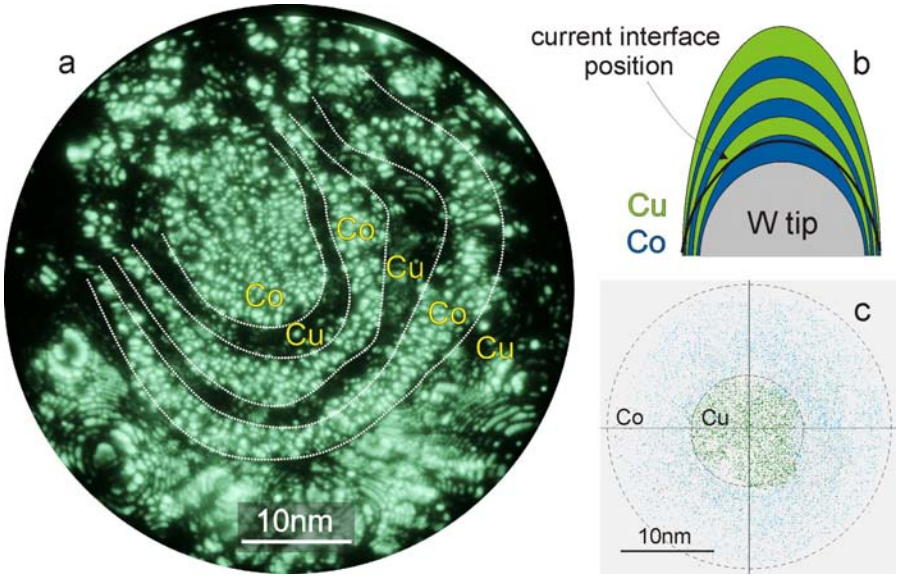

Figure 3.14: Features of FIM/TAP analysis of inhomogeneous multilayer specimens. (a) FIM image of Co/Cu multilayer. Six different layers outcrop to the surface (the measurement volume is shifted from the tip center resulting in bad symmetry of the image). (b) Sketch of the FIM image formation. (c) WATAP detector map of several thousand events (the centers of measurement volume and tip center coincide).

always be planned in the order of decreasing evaporation field strength to improve the mechanical stability of the sample during the measurement. If the individual layers are very thin (under 1-2 nm) layers sequence does not play a big role for the specimen stability since the individual "unstable" layers are measured through very rapidly. In this case, the increase of the evaporation rate at some locations on the sample surface is compensated by those from regions of lower evaporation probability. The stability of the layer stack becomes unaffected in spite of 20% difference in the evaporation field between Co and Cu (36 V/nm and 30 V/nm, respectively). In Fig. 3.14a one can see a FIM image of Co/Cu multilayer in which six alternating layers of Co and Cu are imaged simultaneously. Due to the typically columnar grain growth of the deposited material, the film profile does not necessarily mimics the iso-field profile of the predeveloped substrate. During the subsequent measurement, the iso-field surface is always maintained, so that a new layer becomes uncovered while the previous ones are still on the surface (sketch 3.14 b)). The situation resembles the measurement of an alloy specimen, with different atomic species being measured in the same time. One has to take care about the possible artifacts in the reconstruction due to the effect described above. The local radii of the tip surface may differ for the locations with different materials considerably, changing the trajectories of the ions. This so-called local magnification effect is described in detail in [71]. Consequently, the evaporation rates at a given moment can be very inhomogeneous. When a new layer of material with lower evaporation field appears at the surface, evaporation takes place preferentially from the respective area,

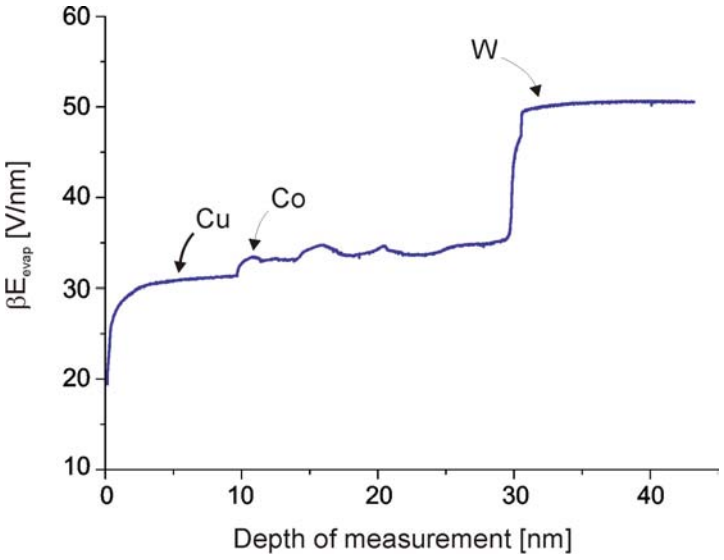

Figure 3.15: Typical βE_{evap}-trace ($\beta = 7$).

until the equilibrium local radius is reached as can be seen from the detector map of several thousand events in the Fig. 3.14c (the density of the measured ions is higher in the middle part of the picture, on the locations, where Cu is detected). This way, the volume reconstruction reveals compressed regions on the higher-to-lower evaporation field interfaces and gaps or expanded z-scaling on the lower-to-higher evaporation field interfaces. On the other hand, the described effect can be weakened to some degree by the fact that the real evaporation field difference of materials in multilayer can be much smaller than predicted for the pure materials. A field development of substrates prior to the deposition is very important to achieve an undisturbed reconstruction of the atom positions of the interface region. If this is not the case, a distorted interface region is obtained in the atomic reconstruction. Furthermore, asperities on the substrate surface may destroy the planarity of the single layers and by that changing the physics of the interface-related processes. As well, attention has to be payed to the alignment of the specimens during development, deposition and measurement to ensure sufficient symmetry of the measured data. As an example, the FIM image in the Fig. 3.14a reveals poor symmetry due to the tilt of the specimen axis during deposition or measurement. It is a daunting task to evaluate misaligned TAP measurements. Good alignment results in concentric interfaces of the respective films as exemplified in TAP detector map are shown in the Fig. 3.14c.

To project the impact position at the detector to the atomic position on the tip surface, the actual tip radius R has to be known (Eq. 3.11). Blavette et al. [72] calculate the radius from the applied voltage and the evaporation field according to Eq. 3.1. But because of the considerable variance of evaporation fields in heterogeneous layer specimens, this formula leads to severely distorted volume reconstructions [73] (if parameters of pure Co are used for the reconstruction, the lateral dimension of the Cu layer becomes

underestimated and overestimated for W substrate, which leads to overestimation of the z-direction along the tip axis for Cu and underestimation for W). In order to obtain a reliable reconstruction, in this work the tip radius is determined independently from the varying evaporation field, by geometrical considerations using the initial tip radius R_0 and constant shaft angle γ. The tip radius development during the measurement is obtained by:

$$\frac{dR}{dz} = \frac{sin\gamma}{1 - sin\gamma}\,. \tag{3.12}$$

This equation can be obtained by differentiating Eq. 3.5, assuming γ to be a constant. Geometrical relations are shown in the Fig. 3.6 ($dz = Nd_{hkl}$). Usually, R_0 and γ are adjusted until the evaporation field strength deduced from the volume reconstruction and the measured tip voltage matches the known evaporation fields of the pure metals outside the reaction zone according to Eq. 3.1. As a first approximation for the initial radius and shaft angle, they can be determined from FIM images of the substrate taken during predevelopment as described in the Sec. 3.2.1 and 3.2.2. A typical $\beta E_{evap}(z)$ dependence is depicted in Fig. 3.15 demonstrating the different evaporation fields in relation to the various phases.

3.4 X-ray diffraction (XRD) characterization

X-ray diffractometry was carried out with a Siemens D5000 diffractometer using Cu Kα radiation. Primarily it was used for the characterization of the NiFe/Cu specimens regarding the recrystallization taking place during the heat treatment. Volume fraction of specifically oriented grains as well as crystallite size in the system were determined by means of XRD. For that, the peak positions and intensities as well as full width at the half-maximum (FWHM) were measured. All the evaluation issues were made automatically using the custom-made software.

The {111} and {200} reflections indicating the respective textures were evaluated and the volume fraction of <100>-oriented crystallites V_{100}/V_{tot} was determined by the relation:

$$\frac{V_{100}}{V_{tot}} = \frac{\gamma\, I_{200}}{\gamma\, I_{200} + I_{111}}\,, \tag{3.13}$$

where I_{111} and I_{200} denote the integrated intensities of the {111} and {200} peaks. The factor γ takes into account the weaker atomic scattering by the {200} planes and can be estimated to be $\gamma \approx 2$ according to the powder diffraction file (PDF) data (# 04-0836 and #38-0419 for Cu and Py, respectively [74]).

The peak positions were derived using the Bragg's law:

$$\lambda = 2d_{hkl}sin(\theta)\,, \tag{3.14}$$

where λ is the wavelength of the incident x-rays ($\lambda = 1.541$ Å), θ – incidence angle and d_{hkl} – distance between lattice planes, having the (hkl) Miller indices and is determined for the cubic lattice as follows:

$$d_{hkl} = \frac{a}{\sqrt{h^2 + k^2 + l^2}}, \tag{3.15}$$

where a is the lattice parameter of respective material. In a conventional XRD measurement, the angle of incidence relative to the sample surface is varied and the angle of detection is kept equal to it. Under this condition (so-called mirror condition) and according to Bragg's law, planes parallel to the sample surface can be detected. Predominant crystallographic orientations of grains (texture) in the polycrystalline samples were detected using this principle. The extinction rule for the face centered cubic (fcc) lattice allows only such peaks to be measured, which have all the miller indices even or odd. Thus, it is not possible for example to observe 100 reflections, instead 200 are detected being produced on the same planes family and corresponding to the <100> texture.

The crystallite size can be estimated using the following considerations (as derived in [75] and by other authors). When diffraction in an ideal infinite crystal occurs, i. e. when the Bragg condition (Eq. 3.14) is satisfied with the angle of incidence being θ_B, then the path difference between adjacent planes is exactly a multiple of λ. When the incidence angle deviates from θ_B, every plane has a counterpart deeper in the crystal, which is exactly in antiphase, so that the diffracted waves of these two planes cancel each other. In the infinite ideal crystal, the only angle at which the waves do not disappear due to the destructive interference is the θ_B. The closer the angle to the θ_B, the deeper in the crystal lies the plane which produces the antiphase wave. But when the crystal is not infinite and deeper planes producing the antiphase waves are not present, there is net scattering also at close to θ_B angles and the peak becomes broader. It follows that there is a correlation between crystallite size and peak width, which is expressed for cubic lattices by the Scherrer equation:

$$t = \frac{0.9\lambda}{Bcos(\theta_B)}, \tag{3.16}$$

where t is the crystallite size measured normal to the scattering plane and B is the FWHM of the correspondent x-ray peak measured in radians. The factor 0.9 in the equation is dependent on the specific lattice structure constant. The peak broadening may also result from instrumental inaccuracy and from the stress state of the sample. Thus, the crystallite size may be underestimated. Therefore, appropriate corrections have to be made in order to get an accurate evaluation.

3.5 Transmission electron microscopy (TEM) characterization

Grain morphology and layer structure were characterized by TEM. The same method was also used for FIM/TAP specimens geometry characterization. The instruments Hitachi H800NA (LaB_6-cathode) and Zeiss Libra 200FE were applied, both with an operation voltage of 200 kV were applied. FIM/TAP samples were introduced in the microscope using a dedicated specimen holder. Due to the miniature dimensions of the tip-like specimens, no additional specimen preparation is needed in order to get transmission microscopy images. Since the presence of a contamination film may hinder subsequent accurate FIM/TAP investigations, special measures have to be observed regarding the vacuum conditions.

3.6 Sample preparation

In this work two major types of specimens were used. For the investigation of mismatch-induced recrystallization, studied by XRD and TEM methods, NiFe/Cu multilayer systems, and for multilayer morphology and structure investigations, studied by means of FIM and TAP techniques, Co/Cu multilayer systems.

3.6.1 Specimens for FIM/TAP (curved substrate geometry).

As it was mentioned above, the atom probe analysis of thin films requires particular efforts in preparation of specimens, since the investigated layers must be deposited on a substrate tip of only 30-50 nm radius of apex curvature. The preparation of FIM/TAP specimens involves:

1. Electropolishing of tungsten wire;
2. Field development of the W-tip in a FIM;
3. Deposition of desired materials;
4. Heat treatment of the specimen.

At the first step, high-purity tungsten wire is cut into pieces of about 1.5 cm in length and fastened to a Cu tube, which serves as a handle. The wire is then electropolished in two molar sodium hydroxide (NaOH) solution by short pulses of 2-7 V of AC voltage in order to obtain a geometry suitable for the FIM. Fig. 3.16 demonstrates the setup used

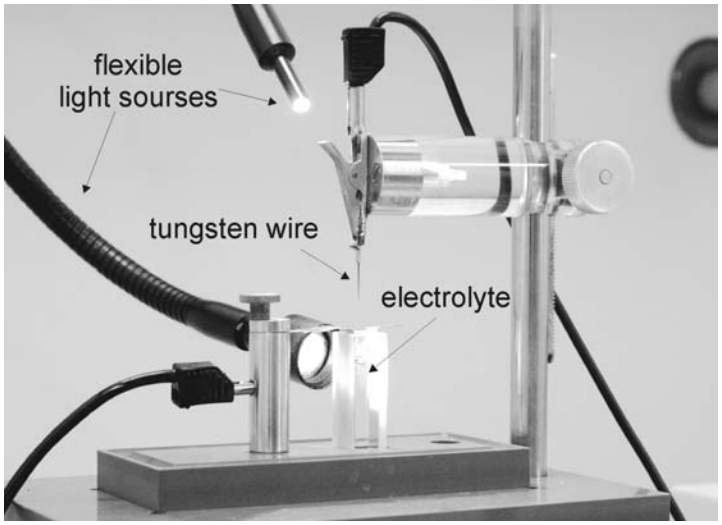

Figure 3.16: Arrangement for electrolytic etching and polishing of FIM samples.

for electropolishing. Good skills and feeling are needed to produce specimens having an apex curvature radius of 10 nm only. The shape of the tip is controlled in a optical stereo microscope in one ocular of which the bright field and in other the dark field conditions are adjusted using a flexible light source. After electropolishing, the tip is developed in the FIM to produce a smooth surface and to increase the radius of the tip apex curvature to some 30-50 nm. The tip is typically developed to voltages of about 12 to 14 kV. Subsequently, the tips are transferred into a sputtering chamber, where the desired materials are deposited (see Sec. 3.6.3). The last step in specimen preparation is the thermal treatment in UHV furnace.

Electrical grounding of the sample during its handling has been proven to be a very important point to avoid formation of amorphous W oxide layer, which deteriorates the quality of the substrate tip (see the details in the Sec. 4.1).

3.6.2 Specimens for XRD/TEM (planar substrate geometry).

Multilayers for preliminary investigations (Py/Cu multilayer as well as Py/Cu/Co/Cu and Co/Cu) were prepared in a laboratory at University of Bielefeld using a L560 and a CLAB600 (Leybold Dresden) magnetron sputtering systems. A brief report about the sputtering conditions and multilayer structures prepared is given in App. C. The main series of specimens was produced in the Institute of Material Physics in Münster using the ion beam sputtering technique. The efforts were concentrated on a particular architecture of the system, namely $[Ni_xFe_{(1-x)\,3\,nm}/Cu_{6\,nm}]_{20}$, since in preliminary investigations a thickness ratio 2:1 (Cu:Py) was distinguished by a very high probability for recrystallization. This striking dependence of the transformation probability on the

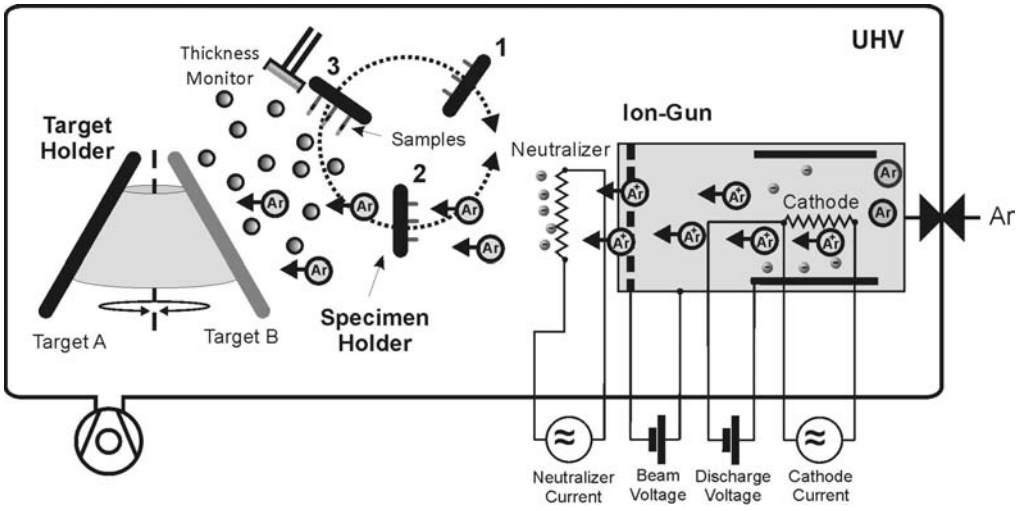

Figure 3.17: Schematic drawing of the ion beam sputtering chamber.

relative thicknesses will be quantitatively justified in the discussion of the experimental results. As substrates thermally oxidized silicon wafers of [100] orientation and an oxide thickness in the range of 47 nm to 1.5 μm were used. The root mean square roughness of such wafers amounts to about 0.3 nm, as measured with atomic force microscopy. In some cases, conventional glass substrates were used as well.

Cross section thin foils for TEM investigations were prepared using a standard preparation technique. The substrate with the deposited layers is fitted between two halves of a copper cylinder placed into a tiny stainless steel tube of 3 mm in diameter. Special UHV-glue is used to fix the parts together. This tube is cut into 0.5 mm thick slices, which are subsequently ground manually to a thickness of 100 μm or thinner. Using the dimple grinder, the sample is further thinned to a thickness of 30 μm in the center of the specimen. Subsequently, Ar^+ ion milling (5 kV and 20μA at room temperature) is applied to decrease the thickness of the sample in the central region to 20-50 nm, which is suitable for TEM.

3.6.3 Ion beam sputtering technique

Thin film deposition has been performed in UHV chamber with a base pressure better than $1 \cdot 10^{-5}$ Pa. A quartz crystal thickness monitor enabled a precise thickness indication. Custom made deposition software, controlling the deposition rates, ensured reproducible multilayer structures and decreased the efforts in specimens preparation (the quality of multilayers was increased substantially after software implementation).

The basic principle of ion beam sputtering is the bombardment of so-called targets (plates of material to be deposited) with Ar gas ions having kinetic energies typically

	Beam voltage [V]	Beam current [mA]
Target cleaning:	800	30
Substrate cleaning:	500	10
Deposition (XRD/TEM):	800	30
Deposition (FIM/TAP):	550	15

Table 3.2: Sputtering parameters for preparation of FIM/TAP specimens.

of about 1 kV. The material is removed (sputtered) from the target and forms a cloud of radially moving particles. This particles of target material are deposited onto the specimens situated in front of the target. The Ar gas, which is supplied to the vacuum chamber is ionized and accelerated in a so-called Kaufmann ion source. A neutral Ar gas is ionized by electrons that are emitted from a heated filament. These Ar ions then drift through a pair of closely spaced carbon grids, where they get their final kinetic energy (see the Fig. 3.17). The ion beam emerges from a 40 mm grid plate at the front of the source (where it is neutralized to avoid target charging) and diverges to a diameter of about 60 mm near the targets. The typical working pressure of Ar-gas is about $2 \cdot 10^{-2}$ Pa. During the deposition considerable energy is transferred to the targets, so that they warm up, changing the deposition rates during sputtering. Therefore, water-cooling is utilized for maintaining the targets at room temperature. Targets are attached to a rotatable target holder, which allows switching between different materials within a fraction of a second. The specimens are placed in the deposition chamber onto a specimen holder which can also be rotated. As seen in the Fig. 3.17, there are 3 different positions for the specimen holder which are used in turn during the deposition procedure:

1. target cleaning in order to remove oxide and contamination films before deposition;
2. tip cleaning necessary to produce stable specimens;
3. thin film deposition.

Main sputtering parameters for the preparation of reliable FIM/TAP specimens are listed in Tab. 3.2 The correspondent sputtering rates of $Ni_xFe_{(1-x)}$ and Cu (specimens for XRD/TEM analysis) were about 2.1-2.3 Å/s and 3.7 Å/s, respectively. For Co and Cu (FIM/TAP specimens) 0.4 Å/s and 0.75 Å/s, respectively. The ion beam sputtering chamber used in this work offers the ability to perform thermal treatment without breaking the vacuum.

Figure 3.18: $Ni_xFe_{(1-x)}$ target prepared by melting pure Ni and Fe materials.

Targets for ion beam deposition

The $Ni_xFe_{(1-x)}$ targets were melted from pure Ni (99.98%) and Fe (99.9%) in an arc furnace. Several targets with 5 to 10% difference in iron content were prepared. The composition of each targets was proven using secondary ion mass spectrometry (SIMS) to be in the range of 2% deviation from the desired concentration. The alloy pieces were prepared in form of small bricks of about 2x4x1 cm^3 and subsequently cut by spark erosion into thin plates. This plates were glued with special UHV glue onto stages having the diameter of 8 cm (see Fig. 3.18). The surface of the targets was then mechanically polished to make it flat and remove contamination resulting from spark erosion cutting. Prior to preparation of first samples, several tens of micrometers of target material were removed by sputtering. The other targets used for the specimen preparation are commercial sheets of high purity materials (Co - 99.99%, Cu – 99.9% and Ni – 99.98%).

3.6.4 Thermal treatment

To investigate the behavior of the GMR multilayer at high temperatures, corresponding heat treatment procedures were carried out. For this purpose FIM/TAP specimens were annealed directly after the deposition of multilayers in the sputtering chamber using a ceramic heating plate. The annealing procedure was carried out in an Ar atmosphere with a pressure of $5 \cdot 10^{-2}$ Pa (residual pressure of about $10^{-}6$ Pa). A dedicated UHV-furnace, consisting of the same ceramic heating plate was used to prepare the planar XRD/TEM specimens. The vacuum level during annealing was held at about 10^{-5} Pa. The samples investigated in this work were annealed at temperatures in the range from 150 °C up to 550 °C and times ranging from 1 to 90 min and from 1 to 24 h for FIM/TAP and XRD/TEM, respectively. It is a critical point that a nominal duration of heat treatment does not represent the total time of the specimen high temperature exposure. This is due to finite times of warming up (about 5 min to reach 450 °C) and cooling down of the furnace (about 30 min to reach 100 °C). This point is especially

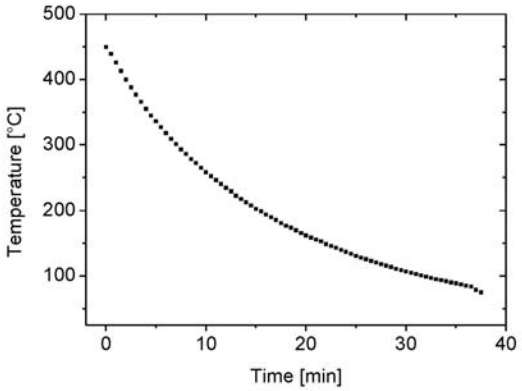

Figure 3.19: Cooling down curve after the heat treatment.

important if annealing times are short. Water cooling was employed to ensure a better annealing time measurement but still the times of cooling are considerable. The typical temperature decrease curve is depicted in Fig. 3.19. This curve may help to estimate effective annealing times depending on the studied physical process.

Chapter 4

Thermal behavior of Co/Cu multilayer system as studied by TAP

Experimental results presented in this chapter were obtained using the 3D atom probe at the Institute of Material Physics in Münster. As first experiments were conducted during the final phase of instrument construction and subsequent rearrangement for the wide angle geometry (WATAP), establishment of specimen preparation and measurement routine was an important task to achieve the reproducibility of experimental results. Several critical issues concerning the WATAP data acquisition and interpretation had to be solved in order to produce reliable volume reconstructions. For the sake of consistency of the preparation and measurement conditions, very early measurements carried out in a "narrow angle" (conventional TAP) geometry are excluded from the discussion, though their contribution is quite valuable for the general understanding of the observed physical phenomena.

4.1 Substrate tip characterization

Well-controlled substrate tip geometry and accurate material deposition process are prerequisites for the reliable TAP measurements and subsequent data reconstruction. Hence, TEM investigations were involved in the specimen preparation for checking of the substrate tip geometry and the quality of deposited layers. A typical micrograph of an as deposited specimen is demonstrated in Fig. 4.1a. The shape of the cross section of the deposited layer is elliptic (see the sketch in the Fig. 4.1b) increasingly deviating from the spherically shaped surface of the substrate tip with the increasing thickness of the layer. Since the fracture probability is significantly higher on the individual Co/Cu interfaces, the total bilayer number was limited to four. Thus, the typical specimens used for FIM and TAP analysis in this study have the following structure: $W/[Co_{2\,nm}Cu_{2\,nm}]_4$. The shaft angle of the W tip in the apex region derived from TEM micrographs coincides with values estimated using the FIM images (as described in Sec. 3.2.2) and is typically of about 7-10°. The substrate tip radius in the apex region after the FIM

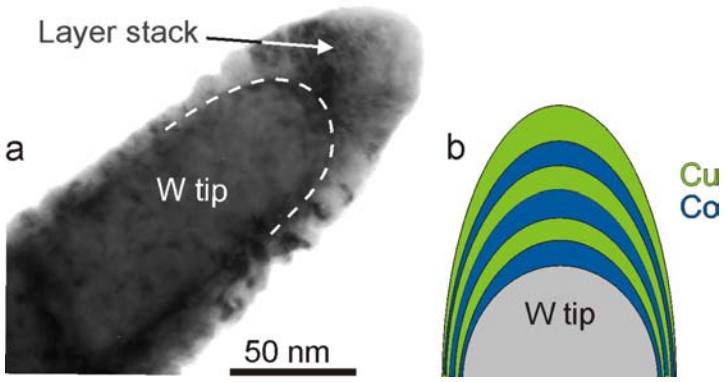

Figure 4.1: (a) TEM micrograph of the Co/Cu multilayer on the W substrate tip. No contrast between individual layers is visible due to the projection nature of the image formation. (b) Sketch of the specimen geometry (tip cross section).

predevelopment is estimated to 30 nm. After the film deposition, the curvature radius of the as-prepared specimen tends to be smaller than those of the substrate tip. However, the field evaporation process settles the equipotential shape of the specimen surface with increased curvature radius. Moreover, due to the lower evaporation fields of cobalt and copper layers compared to the tungsten substrate tip, the radius of the equipotential shape surface becomes higher than those of the initial tungsten tip. Thus, the initial radius of the specimen, after the adjustment of the equipotential shape, is typically about 35-40 nm (this value provides proper z-scaling of 3D volume reconstructions).

As was recently discovered in our group [76], due to a field assisted oxidation process, some 500-1000 V are applied to the tip in ambient atmosphere, produce a thick layer of amorphous tungsten oxide covering the tip surface. It deteriorates the tip and makes it unsuitable for further utilization (see Fig. 4.2). The voltage magnitude needed for the formation of the oxide layer is easily reachable by a static electrical discharge. Thus, it is a very important point to ensure electrical grounding during the specimen handling.

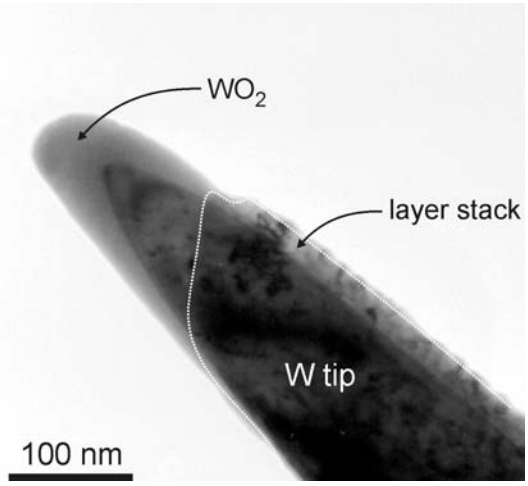

Figure 4.2: TEM micrograph revealing the oxide layer formation. Dotted line outlines the broken thin film stack.

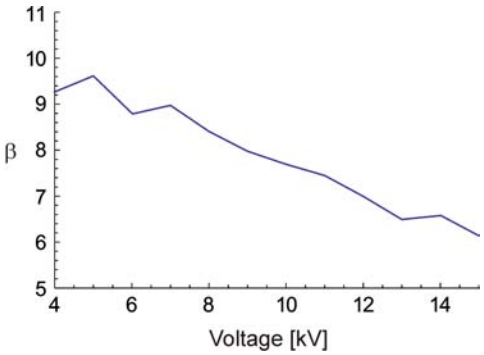

Figure 4.3: Dependence of the geometric factor β on the applied voltage.

Indeed, this issue was the reason for poor measurement efficiency during initial stage of TAP investigations, until careful TEM observations and the comparison with the data of the mentioned study revealed the problem.

The geometric factor β, which is important for experimental data evaluation, is determined by Eq. 3.1 using applied voltage value and estimating tungsten tip radius from the FIM micrographs as described in Sec. 3.2.1. The value of this parameter amounts to about 10 for low voltages (4 kV) and decreases to 6 (14 kV) with the increase of the applied voltage. The exemplary behavior of a $\beta(V)$ curve is depicted in Fig. 4.3.

4.2 FIM analysis

FIM analysis of the Co/Cu multilayer system was carried out in order to reveal the systems' microstructure. Since the field of view in FIM measurements is larger than in TAP measurements, the information deduced from the FIM analysis can be very helpful for TAP data evaluation. It is also important to ensure that the microstructure of the multilayers evolved on the special curved tip surface is comparable to those found in multilayers grown on planar substrates.

FIM micrographs of the Co/Cu multilayer in as-prepared state are shown in Fig. 4.4. The micrographs are obtained by subsequent field evaporation of surface material. The current specimen surface position is indicated in the sketch. As seen from Fig. 4.4a, the layer stack grows with <111> orientation along the tip axis. This feature can be deduced from the three-fold symmetry of the observed configuration of the crystallographic poles in the uppermost Cu layer. The FIM micrograph in the Fig. 4.4b reveals that the (111) crystallographic pole of Co is placed exactly under the (111) Cu pole. This suggests the coherency of the Co/Cu interface structure. A single large grain is typically detected on the tip apex, which is the typical morphological feature observed in thin film TAP specimens deposited on top of the tungsten tips. Grain boundaries, observed mainly on the tip periphery, propagate through the layer stack down to the substrate upon subsequent field evaporation of all deposited layers, implying the columnar grain morphology (this

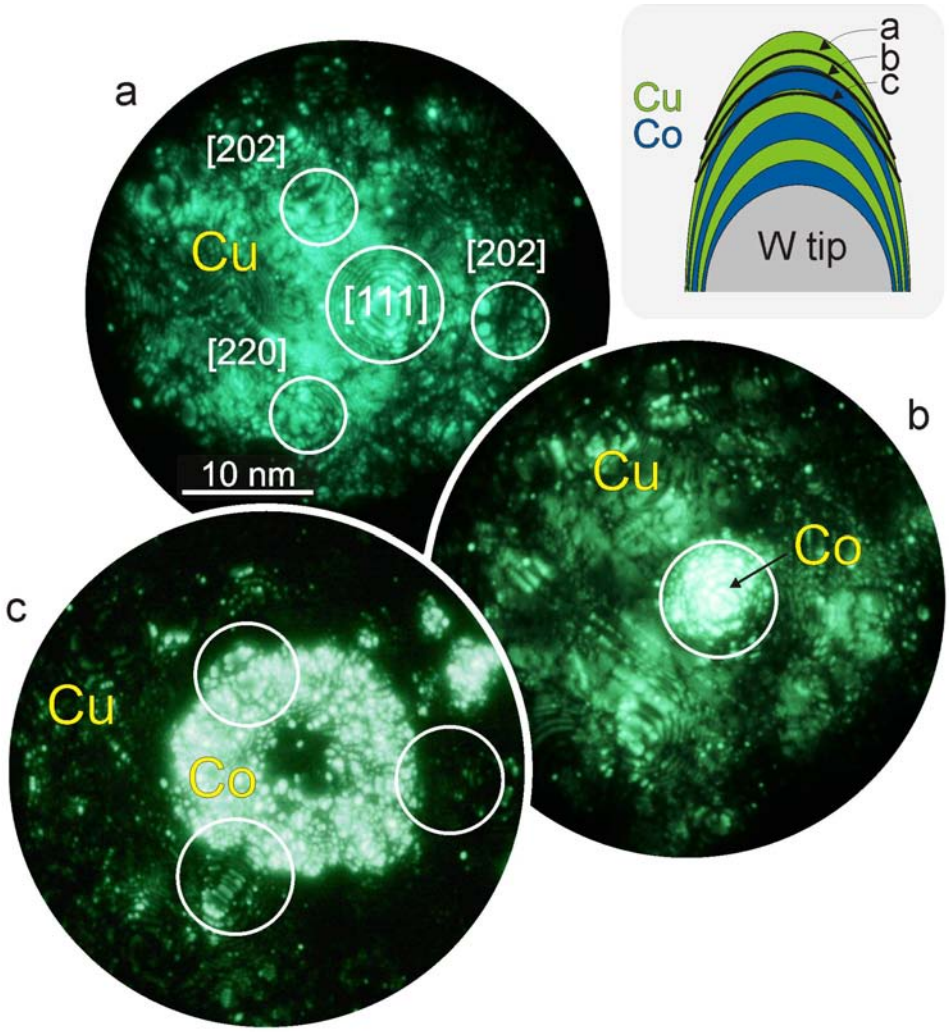

Figure 4.4: FIM micrographs of the Co/Cu multilayer in as-prepared state. The micrographs are obtained by subsequent field evaporation of surface material. Correspondent surface positions are indicated in the sketch by the black lines.

feature is clearly seen in TAP measurements described below). Continuation of the 220 poles from Cu into Co (see Fig. 4.4c) reveals that the Co layers sandwiched between adjacent Cu layers have face centered cubic (fcc) structure and not the hexagonal close packed (hcp) structure as in bulk. There was no indication of hcp Co, which agrees with previous reports on thin Co films on fcc substrates (see Ref. [41, 42, 77]). All the microstructural features described above are similar to those observed in planar specimens (see Sec. 5.1). Thus, no significant discrepancy is expected in the thermal behavior of planar and curved multilayers.

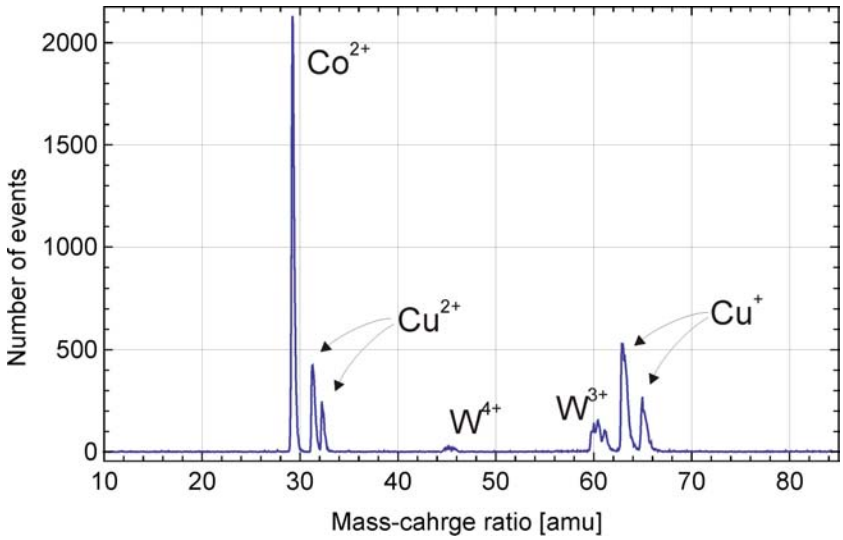

Figure 4.5: Mass spectrum obtained by atom probe analysis of a Co/Cu multilayer.

4.3 TAP analysis

The Co/Cu system was proven to be suitable for the FIM and TAP analysis in voltage evaporation mode. It shows sufficient mechanical stability despite a high number of potentially unstable Co/Cu interfaces. It was possible to conduct the measurements at lowest reachable temperatures ($\approx 30\,\mathrm{K}$), yielding measurement data with rather low noise levels. A typical mass spectrum obtained during the Co/Cu multilayer analysis is depicted in Fig. 4.5. As seen from the figure, individual mass peaks can be distinguished without any overlap ambiguity resulting in reliable species identification. However, the mass spectrum presented in the Fig. 4.5 is produced from the selected reconstruction volume containing the feature of interest rather than the whole data set (larger lateral dimension of the analyzed volume results in decreased mass resolution due to the imperfect length of flight correction for the ions from the tip periphery).

The measurements were carried out with a pulse frequency of 20 kHz, a pulse to base voltage ratio of 26% in a base voltage range of 4 to 14 kV. Ion flux rate was maintained in the range of 0.5-1.0% using the automatic computer control (upward step 1 V, downward step -7 V). Due to the small total layer stack thickness of some 15-20 nm, measurements contained typically 1.5-2.5 million events (larger measurements were produced by measuring the tungsten substrate to a larger depth).

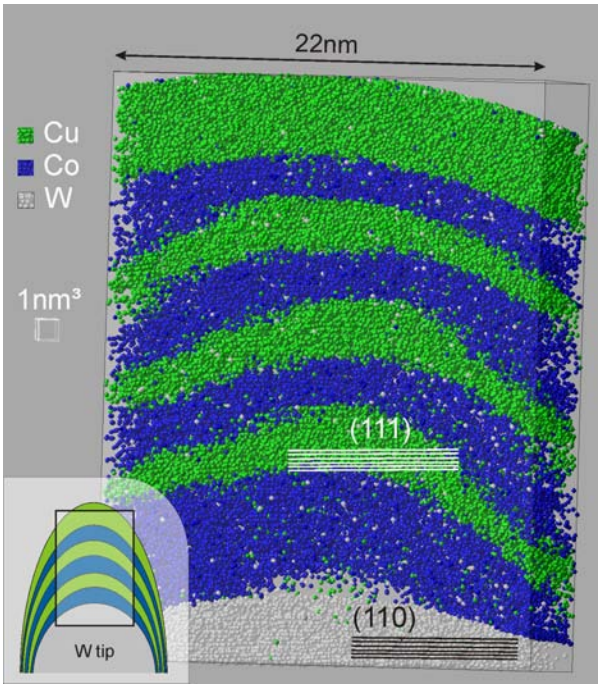

Figure 4.6: 3D volume reconstruction of the Co/Cu multilayer in as-prepared state. Detection area is highlighted in the tip sketch.

4.3.1 Characterization of as-prepared state

A 3D volume reconstruction of the Co/Cu multilayer in the as-prepared state is depicted in Fig. 4.6. Due to the wide angle atom probe measurement setup (WATAP), the diameter of the detection area is large enough to reproduce the curvature of the individual layers induced by the substrate geometry (as **seen** in the sketch). Parallel (110) and (111) atomic planes are resolved inside the tungsten and cobalt/copper layers, respectively. This points to the epitaxial film growth on the substrate, at which, due to the small lattice mismatch, the crystallographic orientation of the deposited film stack is dictated by the substrate crystallography. This feature is also observed during the FIM analysis: the (111) crystallographic pole of the Co/Cu stack is situated directly over the (110) pole of the W substrate tip. The multilayer morphology in as-prepared state is characterized by smooth interfaces with almost uniform layer thicknesses along the interface. In order to evaluate the Co/Cu interface width, 1D compositional profiles are utilized (see Fig. 4.7). Such composition profiles are generated by cutting out a cylindrical volume across the interface and dividing it into small sections along the cylinder axis each of which gives a concentration point in the diagram. Note that the composition profiles are positioned in such a way as to minimize the projection effect resulting from the layer curvature. I.e., for the better chemical resolution along the concentration profile axis, only flat parts of interface can be used for the analysis (smaller analysis cylinder radius can be chosen to minimize the effect of the interface curvature, as in the Fig. 4.7). Proper scaling of the reconstruction volume is of great importance for

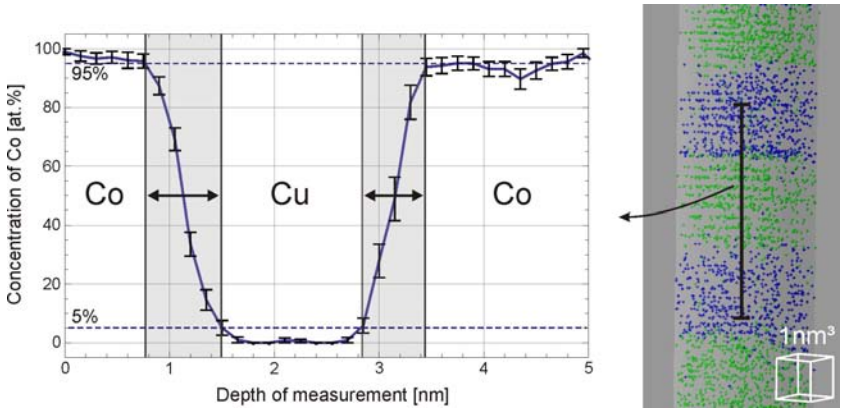

Figure 4.7: Exemplary concentration profile measured perpendicular to the interfaces of three adjacent layers (left). Interface zones, as defined between 5% and 95% Co content, are shaded. Atomic distribution in analyzed volume visualizes almost atomically sharp Co/Cu transition on the interfaces (right).

the accuracy of the described 1D concentration profiles. Fortunately, the atomic layer resolution along the measurement axis provides the possibility to adjust the proper z-scaling of the reconstruction; it can be proven by the right atomic layer distances. The interface width as defined between 5% and 95% of Co content (see Fig. 4.7) from several measurements in as-prepared state amounts to 7.1±1Å. Within the measurement accuracy, the difference of the interface width is the same in both interface configurations: when Cu grows on Co and vice versa.

4.3.2 Thermally induced interface faceting

Thermally induced interface faceting is observed by means of 3D volume reconstructions after annealing at 450 °C for 90 seconds[1]. This morphological reaction was observed for the first time in metallic multilayer systems grown on curved substrates. Due to large lateral dimensions of the WATAP analysis volume (comparable to the substrate tip dimensions), larger areas of layer interfaces could be analyzed during a single measurement (see Sec. 3.3). This allowed to detect non-uniform layer thicknesses, which depend on the crystallographic orientation of Co/Cu interfaces (see Fig. 4.8a). As seen from the figure and highlighted in the sketch, the area of interfaces parallel to (111) planes, which are clearly resolved in this reconstruction, is substantially increased due to the atomic transport taking place in the course of interface faceting. Due to the sufficiently high mobility of the constituent materials, regions of Cu layers with interfaces parallel to (111) planes grow in lateral direction on the cost of material from the interface areas with non-symmetric crystallographic orientations. There is a diffusion flux of Cu atoms to the center of the specimen, whereas Co atoms move to its outer regions. This way, the

[1] actual heat treatment time is larger due to a slow cooling down process (see Sec 3.6.4)

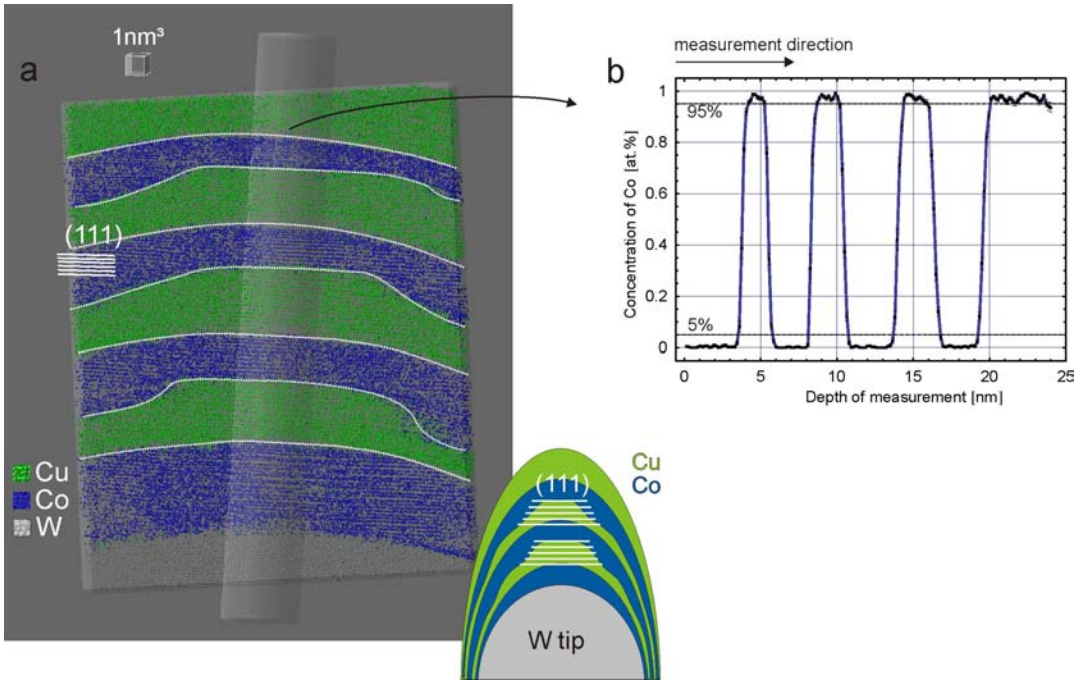

Figure 4.8: Thermally induced faceting of the Co/Cu interfaces. (a) - 3D volume reconstruction of the Co/Cu multilayer annealed at 450 °C for 90sec. The inserted sketch highlights the observed interface faceting. (b) - 1D concentration profile measured along the tip axis as shown in the figure (a) by the transparent cylinder.

steps are formed in the regions where interface planes significantly deviate from <111> orientation (by an angle of about 10-15°), as seen in the Fig. 4.8a). With a high probability, the driving force for the observed morphological transformation is the anisotropy of interfacial energy. Typically, vicinal surfaces and grain boundary planes are found to be unstable and facet into high-symmetry (low interfacial/surface energy) (111) and (100) crystallographic orientations [78, 79]. Thereby, the phenomenon of interface faceting resembles the well known surface and grain boundary faceting.

Despite of atomic transport, the 1D concentration profile generated from the middle region in the volume reconstruction (shown by the transparent cylinder) remained very sharp regarding the Co/Cu interfaces (see Fig. 4.8b). The average value of the interfacial zone determined from several measurements in this reaction stage is 6.2±1Å, as measured between 5% and 95%. Slight sharpening of the interface is attributed to the expected demixing tendency of Co and Cu materials. As seen in the 3D volume reconstruction in Fig. 4.8a, reduced normal spacing of (111) layers takes place in the topmost Co layer and no atomic planes at all are observed in the uppermost Cu layer. This points to a reconstruction artifact in this region. Thus, mentioned above layers were excluded from the interface width analysis. In some measurements, lower detection efficiency of Co was observed, resulting in smaller (111) plane distances than expected from the scaling in copper and tungsten layers. This could be corrected by an appropriate

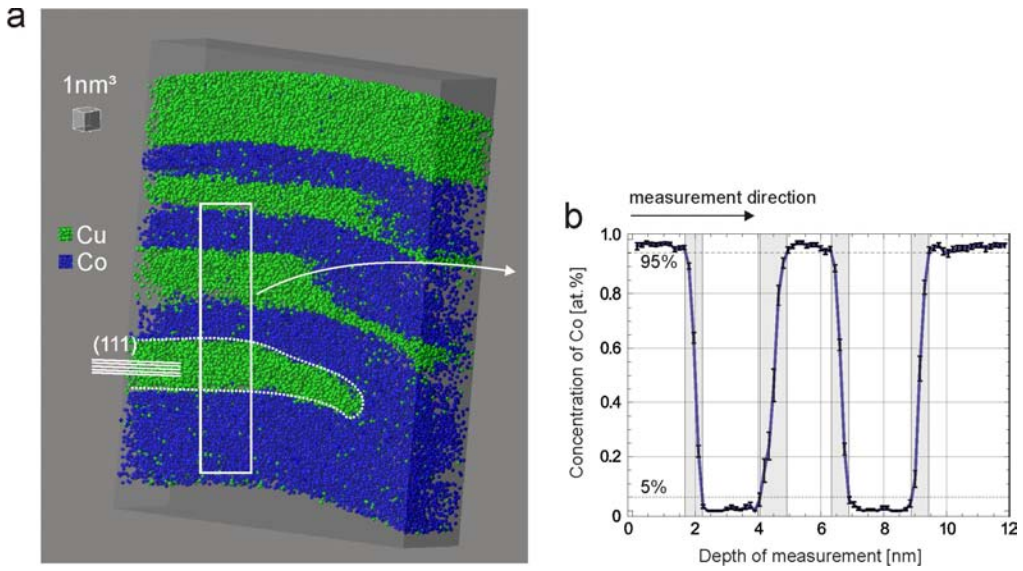

Figure 4.9: 3D volume reconstruction of the Co/Cu multilayer annealed at 500 °C for 30 min. The junction of two Co layers is observed, which arises due to the layer faceting morphology transformation. (b) - 1D concentration profile measured along the tip axis as schematically shown in the figure (a).

decrease of the atomic density of Co (it is not possible to change the detection efficiency parameter for each material independently). In this quite artificial way, proper scaling could be adjusted, which is crucial for accurate interface sharpness evaluation.

4.3.3 Co breakthrough through Cu layers due to layer faceting transformation

Multilayer morphology transformation described in the previous sections is detected in all specimens annealed at 450 °C and higher temperatures. Several measurements annealed at 500 °C revealed a Co layer bridging in the outer specimen regions due to the atomic transport in the course of the layer faceting (see Fig. 4.9a). Unfavorable interface crystallography (interface orientations with high interfacial energy) results in a continuous decrease of the local layer thickness up to its final breakup. This stage is believed to be an initiation of the material fragmentation process observed after annealing at higher temperatures.

A concentration profile measured across the layer interfaces as depicted in Fig. 4.9a reveals no change in interface width after annealing at 500 °C (see Fig. 4.9b). Its average value, 6.3±1Å, is almost the same as those observed after annealing at 450 °C . Thus, in the whole range of annealing temperatures, the interface width remains constant having a value of 6 to 7 Å.

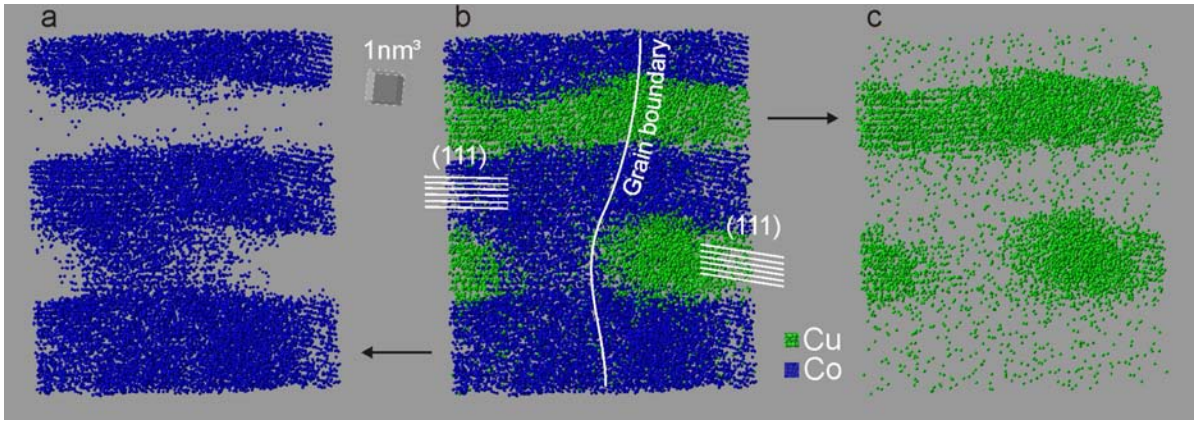

Figure 4.10: 3D volume reconstruction of the Co/Cu multilayer annealed at 450 °C for 90 min. A Co breakthrough through the Cu layer is observed on the grain boundary site. The presence of the grain boundary is deduced from different atomic layer inclinations on the left and right sides of the reconstruction. Co breakthrough morphology is demonstrated by means of different reconstruction representations: (a) - Co atoms (Cu atoms are hidden); (b) Co and Cu atoms map; (c) Cu atoms (Co atoms are hidden).

4.3.4 Co breakthrough through Cu layers at grain boundaries

Another mechanism of the deterioration of layered geometry is observed in the measurement demonstrated in Fig. 4.10. Due to the excellent resolution of this measurement, many interesting features can be revealed. A grain boundary can be identified in the middle of the reconstructed volume as shown in Fig. 4.10b. Its presence is deduced from the different inclination of (111) atomic planes on the right and on the left hand side, as shown in the figure. Apparently, Co breakthrough borders the grain boundary. It can be assumed that this breakthrough is initiated by the grain boundary diffusion of Co into Cu. Taking into account that the atomic reconstruction demonstrated in Fig. 4.10 is confined by a cylinder having 8 nm in diameter, the Co breakthrough takes place along the plane of grain boundary having the lateral extent in the Cu layer of about 2-3 nm (the same as the Cu layer thickness). A further interesting feature, which can be identified in Fig. 4.10b is the coherency of the Co breakthrough and the adjacent edge of the Cu layer within the left grain (continuation of lattice planes from Cu to Co). Presumably, observed Co breakthrough occurred due to the grain boundary movement from the left copper layer edge to its current position. From the four measurements of the specimens annealed at 450 °C for 90 min, a Co breakthrough was observed only in the measurement presented above. Although grain boundaries could be identified in two other measurements, no indication even to the grain boundary diffusion process could be found (see Fig. 4.11). A 1D concentration profile across the grain boundary in the Cu layer did not reveal any statistically significant Co transport there.

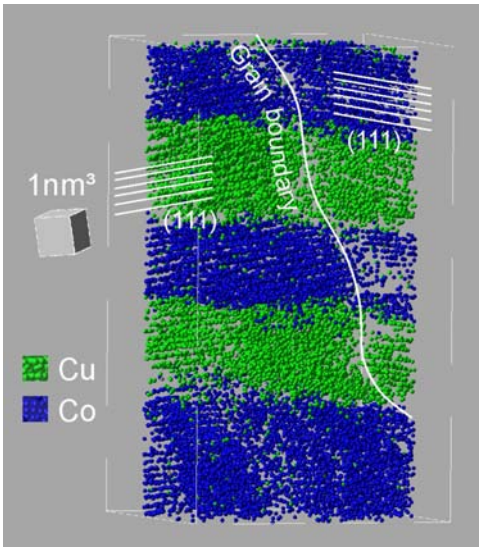

Figure 4.11: 3D volume reconstruction of the Co/Cu multilayer annealed at 450 °C for 90 min. Despite the presence of a grain boundary, no Co breakthrough through Cu is observed in this specimen.

4.3.5 Layer interpenetration in the later annealing steps

Transformation from a multilayer towards a granular-like structure is observed after heat treatment at 550 °C for 50 min. Interpenetration of layers takes place in the course of material fragmentation, driven by the reduction of interfacial energy related to the layer interfaces (see Fig. 4.12). Due to the extensive destruction of the layer structure, an iso-concentration representation of the 3D volume reconstruction is chosen for the demonstration. Iso-concentration surface is determined by a three dimensional concentration grid, which is created in the reconstructed volume. Points of chosen constant concentration are connected by the iso-concentration surface (interpolation between grid points values is applied for exact iso-surface determination). The behavior, which is observed at this reaction stage, is in agreement with the results of the XRD investigations carried out by Hecker et al. [80].

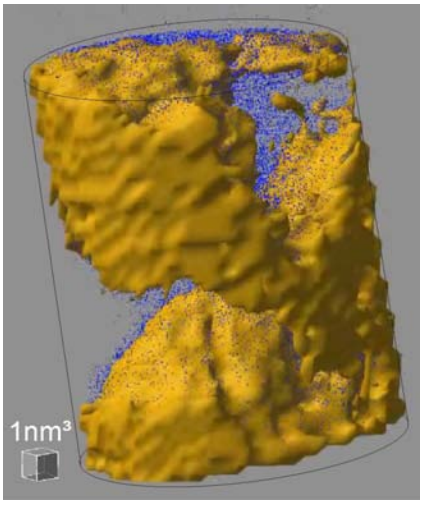

Figure 4.12: 50% Co iso-concentration surface of the specimen annealed at 550 °C for 50 min (no Cu atoms are represented). Layered geometry is destroyed due to the morphological transformation into granular-like structure.

Chapter 5

Texture transformation under annealing

5.1 Experimental background

As proven by TEM and wide angle X-ray diffractometry during the preliminary study, Co/Cu and Py/Cu/Co/Cu multilayer systems reveal in the as-prepared state a columnar grain structure with a well-defined <111> wire texture. The columnar grains with an average lateral size of 10-15 nm spread in the normal direction across several single layers, as shown in Fig. 5.1a,c. During a thermal treatment at 350-500 °C, a recrystallization takes place, which leads to grain growth by orders of magnitude (see Fig. 5.1b,d), so that the layers end up in a quasi-single-crystalline structure. Moreover, the texture transforms into a <100> direction perpendicular to the layers as is demonstrated by the respective diffraction patterns shown on the inserts of Fig. 5.1(a-d). As indicated by the TEM micrographs in Fig. 5.1b,d and proven by TAP investigations in this work and in [11], the chemical integrity of the layer structure is to a great extent preserved or even enhanced by the thermal treatment. This behavior is observed in both Co/Cu and Py/Cu/Co/Cu multilayers. It is rather surprising, at least in the case of Py and Cu, since Ni and Cu materials are completely miscible above 354.5 °C (see Fig. B.3).

Since the RKKY interaction is controlled by the Fermi surface of the paramagnetic spacer, the thickness of maximum AFC depends on the crystallographic orientation of the Cu layers. Thus, the observed texture reorientation should influence the magnetoresistivity of a given system. In Fig. 5.2 the change in GMR amplitudes by a heat treatment of 1h at 500 °C is shown for different spacer layer thicknesses. The figure shows almost complete degradation of the GMR amplitude for a Cu layer thickness of 2.05 , corresponding to the 2nd AFC maximum in <111> orientation. However, for a Cu layer with a thickness of 2.77 nm, corresponding to the 2nd AFC maximum in <100> orientation, an increase in the GMR amplitude is observed. Furthermore, a specimen prepared with a <100> texture via a suitable pre-annealing remains stable during subsequent long-term heat treatments at rather high temperatures (e.g. 400 °C for 64 h).

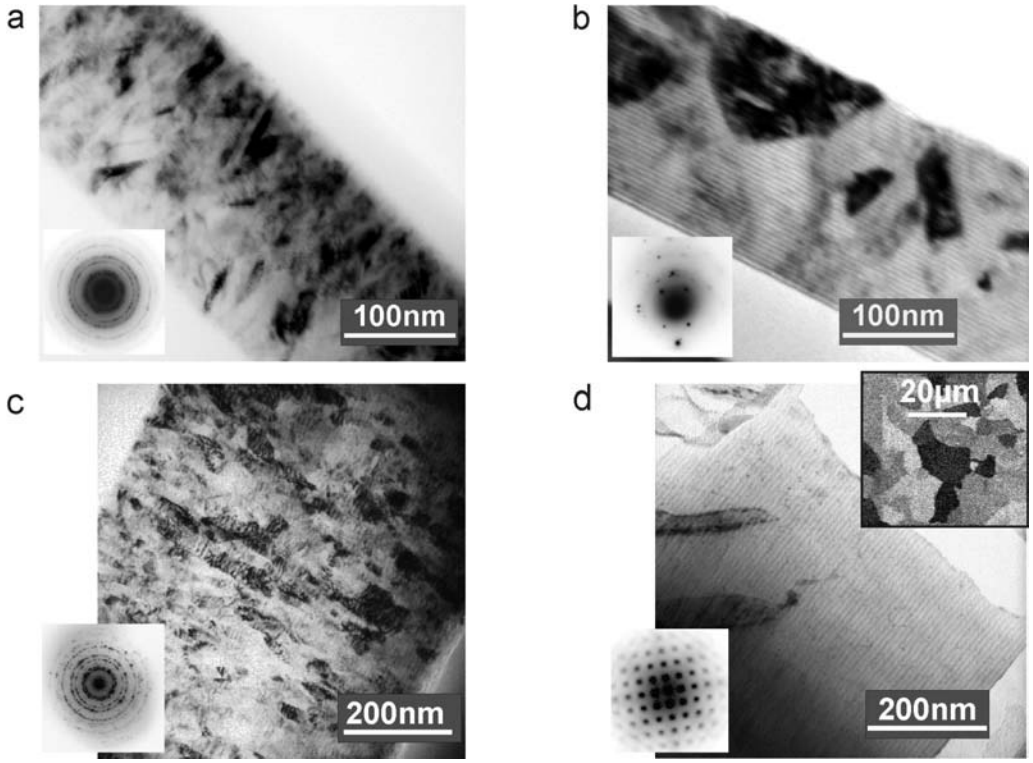

Figure 5.1: (a,b) TEM images of the $[Co_{2.0\,nm}/Cu_{2.65\,nm}]_{40}$ system in as-prepared and annealed (500 °C for 1 h) states with respective diffraction patterns (adapted from Ref. [12]). (c,d) TEM images of the $[Py_{3\,nm}/Cu_{6\,nm}/Co_{3\,nm}/Cu_{6\,nm}]_{40}$ system in as-prepared and annealed (350 °C for 24 h) states with respective diffraction patterns. In (d), a SEM image of lower magnification is shown in upper insertion. TEM images were considerably defocused to accentuate the compositional contrast between individual layers.

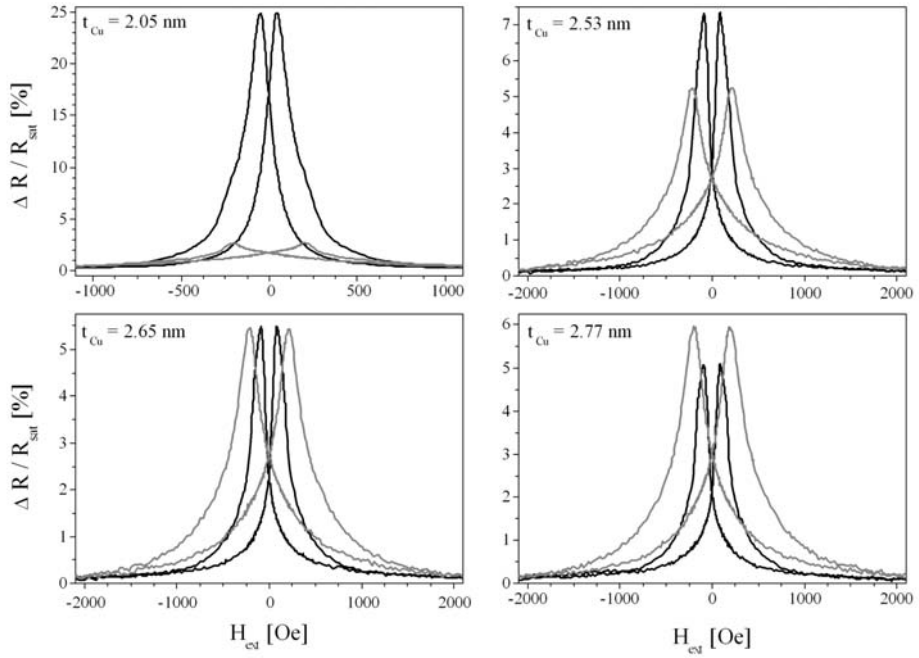

Figure 5.2: Magnetoresistance loops in as-prepared state (black) and after annealing at 500 °C for 1h (grey) of $Co_{3.8\,nm}/Cu_{t_{Cu}}/[Co_{2.0\,nm}/Cu_{t_{Cu}}]_{40}$ multilayers with Cu spacer thickness as stated (from Ref. [12]).

Thus, the recrystallization offers a possibility of producing sensor layers of very high thermal stability [12].

In consequence, it is expected that the described recrystallization will affect significantly the GMR amplitude of a layer system. The understanding of this recrystallization phenomenon is a prerequisite for controlling GMR degradation at high temperatures. In the following, we will focus on the driving force of the described transformation. In general, either the anisotropic interfacial energy or anisotropic elasticity can be the decisive factor. With the experiments described below the actual driving force is identified by controlling the lattice mismatch in the NiFe/Cu system (Py = $Ni_{81}Fe_{19}$) by changing the content of Fe in NiFe layers and thus the elastic energy in the system. Experimental findings are interpreted by theoretical estimations of the contributions to the final driving force in Chap. 6.2. But first, it is necessary to check whether Py/Cu multilayers undergo the same microstructural transformation as is observed in Co/Cu and Py/Cu/Co/Cu multilayers. For that, the microstructural analysis of Py/Cu multilayers is carried out as described below.

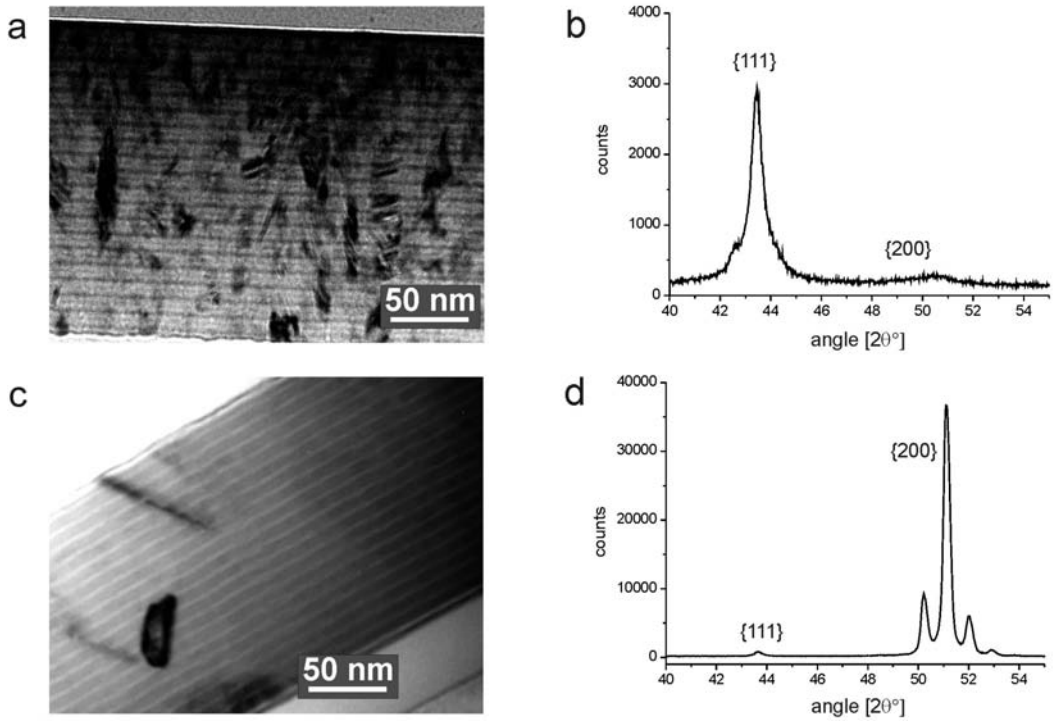

Figure 5.3: Microstructure of a Py/Cu system. (a,c) TEM images of the $[Py_{3\,nm}/Cu_{6\,nm}]_{20}$ system in as-prepared and annealed state (450 °C for 24 h); (b,d) Bragg-Brentano X-ray diffractograms corresponding to the specimen states in (a) and (c). TEM images were considerably defocused to accentuate the compositional contrast between individual layers.

5.2 Microstructure characterization of Py/Cu system

In the as-deposited state, the X-ray patterns of the Py/Cu multilayers show a predominant <111> texture (see Fig. 5.3b) and a considerably broad distribution of grain orientations. As seen from TEM micrographs (see Fig. 5.3a), the grain sizes normal to the interfaces amount to about 20-30 nm, as is also determined from x-ray measurements using the Scherrer equation (Eq. 3.16). Whereas the lateral grain size amounts to 10-15 nm. Thus, the grain morphology is essentially columnar, the same as in Co/Cu and Py/Cu/Co/Cu multilayers. It should be noted, that in $Ni_xFe_{(1-x)}$/Cu multilayers the mean grain size has a tendency to become smaller for lower iron contents and also for iron concentrations higher than 60%, at which the FeNi alloy reveals a body-centered cubic (bcc) structure with a significantly different lattice parameter. In addition, there exists a correlation between the thickness of the Cu layers and the average grain size. An increase of the Cu layer thickness in $[Cu_{x\,nm}/Co_{2\,nm}]_{40}$ systems from 2 to 2.8 nm leads to a 30% enlargement of the initial <111> grains perpendicular to the interfaces (from 19 to 25 nm) (see Ref. [12]). Extrapolation to the respective pure materials films confirms this observation in Py/Cu system. Pure Py layers, Py/Cu multilayers and pure

Cu layers of comparable total thickness exhibit sizes of 10 nm, 20 nm and 35 nm normal to the interfaces, respectively. Presumably, the increase with Cu content is due to the higher mobility of Cu ad-atoms during the deposition.

5.2.1 Texture evolution under annealing

Annealing at relatively low temperatures (200 °C for 24 h) has no effect on the X-ray diffraction peak intensities, and the FWHM of the corresponding peaks is unchanged. Thus, the only change in microstructure at this stage is the annihilation of lattice defects. This is confirmed by the reduction of the overall resistivity in the metallic stack and, consequently, an increased GMR effect amplitude [7]. The absence of microstructural transformation is also observed in recent in situ X-ray measurements made by Hecker et al. [81] In their experiments temperature was increased in successive steps following the $\theta/2\theta$-scans, which results in a very low heating rate. The authors stated that no structural changes are observed up to 300 °C.

By contrast, a complete transformation of microstructure is observed after annealing at 450 °C. Irreversible transition of the initial broad <111> to a sharp <100> texture takes place as a result of secondary recrystallization. This texture reorientation is clearly demonstrated by wide angle X-ray diffractometry. X-ray patterns obtained in Bragg-Brentano geometry before and after the thermal treatment are shown in Fig. 5.3b,d. Furthermore, the improvement of reflection satellites in the annealed state, which are to be expected for coherent multilayer systems with single film thicknesses thinner than some 10 nm [82], confirms the enhancement of the layer structure and the interface quality. The described change of the microstructure occurs due to abnormal growth of <100> grains and stagnation of the <111> texture component. Some individual <100> grains grow through the complete multilayer stack, spreading in lateral direction on a macroscopic scale (compare Fig. 5.3c and Fig. 5.1d upper insertion). A bimodal grain size distribution develops. On the other hand, the maximal grain size is limited by the total stack thickness of about 200 nm. Surprisingly, even after the secondary recrystallization the layered geometry remains preserved in Py/Cu system. Obviously, the considerable amount of interfacial energy saved in layer-to-layer interfaces is not released, although atomic transport is possible at the moving recrystallization front. Indeed, one may expect complete mixing of constituents in the miscible NiFe/Cu system (see the Fig. B.3) as well as layer fragmentation into pure element regions in the case of the immiscible Co/Cu system (see the Fig. B.1). But those processes are reported only after annealing at even higher temperatures of at least 500 °C, as shown in the current work and in [11, 80]. Thus, due to the likeness of Py and Co materials (almost exactly the same lattice parameter and material stiffness), similar microstructural reaction is detected in both Py/Cu and Co/Cu systems. The main features of the microstructure in as-prepared and annealed states are listed below:

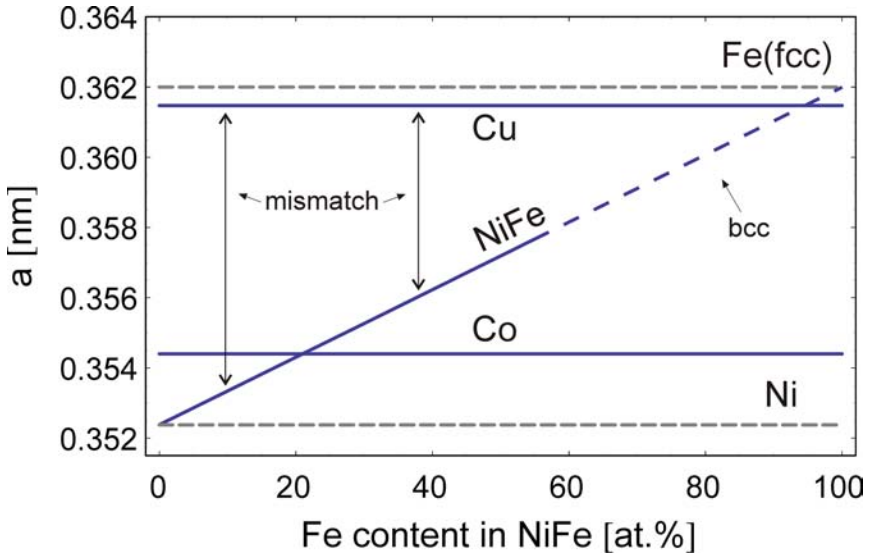

Figure 5.4: Lattice constant data. Full lines indicate the lattice parameters of Cu [83], $Ni_xFe_{(1-x)}$, and β-Co [83]. Lattice parameter variation in $Ni_xFe_{(1-x)}$ is obtained according to Vegard's law by linear interpolation between pure Ni [83] and fcc Fe (dashed lines). The lattice parameter of metastable fcc Fe is averaged from the extrapolated values found in Refs. [84, 85, 86].

As-prepared:

- polycrystalline nature;
- columnar grain structure;
- <111> wire texture.

Annealed:

- recrystallized quasi-single-crystalline structure;
- <111> to <100> texture transformation;
- preservation of layered geometry.

5.3 Driving force for texture reorientation

In general, only anisotropic constituents of the driving force for recrystallization can be made responsible for a texture reorientation: namely, the anisotropic interfacial or surface energies and the anisotropic elastic strain energy. Strain can result either from the general lattice mismatch between the different layer materials or from differential thermal expansion of the layer stack and the substrate. In order to elucidate the reason for textural transformation, a series of experiments was carried out on the $Ni_xFe_{(1-x)}$/Cu

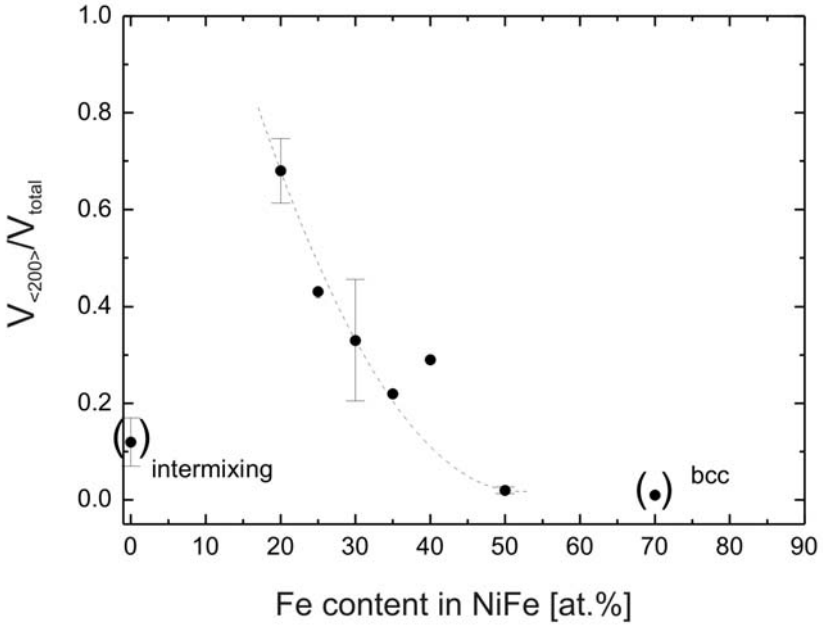

Figure 5.5: Variation of <200>-crystallite volume fraction with Fe content in $Ni_xFe_{(1-x)}$ layers.

system with varying Fe content in $Ni_xFe_{(1-x)}$ layers. This variation changes the lattice mismatch between the $Ni_xFe_{(1-x)}$ alloy layers and the Cu layers as shown in Fig. 5.4. Although the room temperature lattice parameters are shown, at elevated temperatures the lattice mismatch becomes even higher, since the thermal expansion of Cu is larger than that of $Ni_xFe_{(1-x)}$ (Tab. 6.3). Thus, if the texture reorientation is driven by the anisotropic elastic energy induced by the lattice mismatch between the individual layers, the driving force for the texture transformation should be significantly affected by the compositional variation. Moreover, regarding the quadratic dependence of elastic energy on strain, a very significant control of the driving force is expected. Although texture reorientation is not responsible for the GMR breakdown in Py/Cu (in this system GMR deteriorates at earlier annealing stages), this system is used to get insight into the mechanisms of microstructural evolution from both the fundamental point of view and for comparison with Co/Cu multilayers, the GMR stability of which is greatly affected by the texture transformation.

The main experimental result of this investigation is represented in Fig. 5.5. It is clearly seen that the volume fraction of <200> crystallites after annealing depends strongly on the Fe content of the NiFe layers. Thus, the volume fraction depends on the misfit strain in the system. The larger the mismatch, the higher the volume fraction of <200> crystallites. This experimental result indicates that the elastic energy is the controlling driving force for texture reorientation. The data point corresponding to a pure Ni/Cu

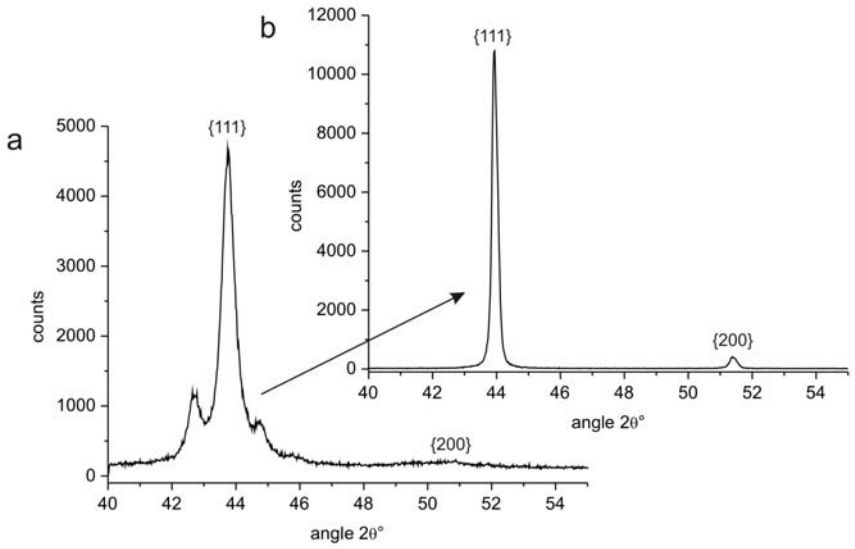

Figure 5.6: X-ray diffractometry patterns of $[Ni_{3nm}Cu_{6nm}]_{20}$ system: (a) as-prepared state; (b) annealed state (450° C for 24 h).

multilayer is parenthesized because the thermal treatment leads in this case to the deterioration of the layer structure. This may be demonstrated by the corresponding X-ray diffraction patterns in Fig. 5.6. In remarkable contrast to Fe containing films, no satellites were observed after the heat treatment, which indicates that the layer structure is degraded. Furthermore, it is seen that no reorientation of the rather sharp initial <111> texture takes place in this case. Similarly, the data point at 70% Fe has to be excluded from further considerations here, since at this Fe content the $Ni_xFe_{(1-x)}$ alloy has switched into the bcc structure [86]. Thus, the presence of a coherent interface is doubtful because of the significantly lower lattice parameter of 2.87 Å for pure bcc Fe. The remaining data between 20 and 50 at.% Fe show clearly that the probability of a texture reorientation decreases with Fe content and vanishes at about 50 at.% iron.

Chapter 6

Discussion

The results of the Co/Cu and Py/Cu investigations presented in Chap. 4 and 5 are discussed in this chapter. Thermally induced morphological reactions in Co/Cu multilayers leading to the GMR degradation are analyzed. Despite of the different thermodynamics of both systems, which result in different mechanisms of the GMR degradation, implications of the Py/Cu study on the texture transformation during annealing can be fully applied to the Co/Cu system. Also the driving forces for the observed texture transformation are discussed in the second part of this chapter, since the precise control of recrystallization may enhance the GMR stability of the Co/Cu system.

6.1 Mechanisms of GMR deterioration in a Co/Cu multilayer system

Numerous studies have been carried out in order to identify the mechanisms of the GMR deterioration in Co/Cu system. The breakdown of the GMR amplitude is usually explained by the degradation of the multilayer structure, but no final agreement exists regarding the exact mechanisms [8, 9, 87, 88]. Cu as well as Co bridging are suggested.

6.1.1 Morphological transformations

Experimental results obtained using the highest resolution microscopy technique revealed the formation of bridges between the neighboring Co layers formed by breakthroughs through the Cu layer along grain boundaries as well as by the interface faceting transformation (see Chap 4). The formation of FM Co bridges was observed after annealing at 450-500 °C (temperature region of GMR amplitude breakdown in the systems adjusted for 2-nd AF maximum [7]). Contrary to the TEM analysis of Rätzke et al. [8] and Bobeth et al. [9], neither Cu penetration along the grain boundaries of Co nor pinhole formation in the Co layer due to interface roughening was observed in the present

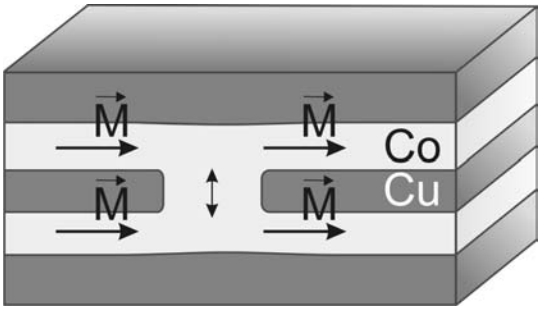

Figure 6.1: Magnetostatic FM coupling due to Co layer bridging.

study. Probably, this processes can be observed only in later annealing states during the massive destruction of layered geometry. However, the stress states induced in the specimens of curved geometry (tungsten tips) can differ from those of planar specimens, and they can potentially affect the mechanisms of layered structure deterioration. Nevertheless, observations of Co breakthroughs through the Cu layers in samples with planar geometry are also reported. Larson et al. [87] and Langer et al. [88] observed such effects at Co/Cu multilayers in the as-prepared state. The presence of ferromagnetic pinholes in thin Cu layers has also been proposed by Kikuchi et al. [89]. FM connections between the Co layers (see Fig. 6.1) would cause a magnetostatic FM coupling deteriorating the GMR effect . As no changes of the interface sharpness were detected by TAP analysis in this work (interface width of 6-7 Å remains constant in all annealing stages), the formation of FM bridges is suggested to be the dominant reason of the GMR breakdown.

Co bridging due to interface faceting

The interface faceting observed by TAP analysis, as described in Sec. 4.3.2, is most likely attributed to the dedicated curved geometry of the substrate tips. Nevertheless, this phenomenon can potentially be observed also in the multilayer systems deposited on planar substrates, due to the waviness of interfaces and the presence of high-angle grain boundaries. Significant layer curvature at high angle grain boundaries was e.g. observed by FIM/TAP analysis of planar Co/Cu specimens that were prepared by means of focused ion beam milling technique in as-prepared state [87]. As seen in FIM micrographs (Fig. 6.2), individual layers within a single grain have a curvature, which is of the same magnitude as those in TAP specimens prepared on W substrate tips. Thus, a situation depicted in Fig. 4.9 can be observed in the high angle grain boundary regions of planar samples as well. As observed in TAP experiments, a 10-15° deviation of the local interface orientation from the <111> orientation is enough to produce an abrupt decrease of the Cu layer thickness. I.e., the faceting transformation, driven by the minimization of the interfacial energy, can lead to the disrupture of the Cu layer on grain boundary locations, where layer interfaces have non-symmetric crystallographic orientations.

Co/Cu multilayers with smooth layer interfaces can be achieved by the deposition of a buffer layer (for example Fe as shown in [88] or Py [12]) prior to multilayer deposition.

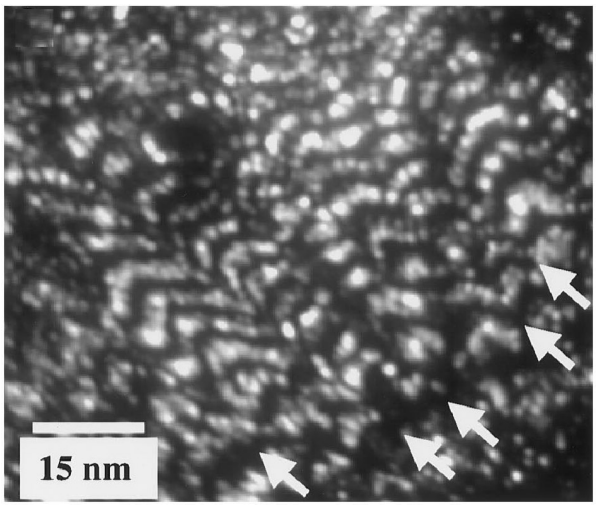

Figure 6.2: FIM micrograph of a planar Co/Cu multilayer in as-prepared state (Co atoms bright). Cross section view prepared using the focused ion-beam milling technique (from Ref. [87])

In this case, layer faceting is prevented so that the GMR amplitude gets stabilized.

Co bridging on grain boundary sites

Let us now discuss the formation of the Co breakthrough through the Cu layer, which is demonstrated in Fig. 4.10. Apparently, this situation is not attributed to the layer faceting as it takes place in the apex region of the specimen, where interface orientation is parallel to (111) planes. A planar interface geometry is observed in this region of the specimen, the planarity is even enhanced by the interface faceting in its initial phase, which takes place at earlier reaction stages. Thus, no significant difference in the layer morphology of the specimens prepared on curved substrates (in their apex region) and planar specimens is expected.

The diffusion coefficient of Co in Cu is described by $D_{Co \rightarrow Cu} = 0.43 \cdot 10^{-4} \cdot exp(\frac{-2.22eV}{kT})$ [90]. Using a diffusivity of $D_{Co \rightarrow Cu} \approx 1.5 \cdot 10^{-20}\,m^2\,sec^{-1}$ a simple $\sqrt{Dt}$ estimate of the diffusion distance of Co in Cu yields about 9 nm, after annealing at 450 °C for 90 min (a reaction stage at which Co breakthrough through Cu is observed). The layered structure is maintained only due to the strong demixing tendency. On the other hand, grain boundary diffusion is activated at this annealing stage having diffusion distances in the order of some micrometers (grain boundary diffusion coefficients are typically by several orders of magnitude higher than volume diffusion coefficients). Grain boundary diffusion was not observed in TAP analyzes because of the very low Co solubility in Cu (lower than 1% for 450,°C), which can not be resolved by TAP analysis.

Due to the high atomic mobility in the multilayers, Co bridges can nucleate at the grain boundaries of the Cu layer. The mechanism of this process can be described in terms of interfacial energy minimization. Let us consider a Co bridge through the Cu layer having a circular shape of radius r (see Fig. 6.3). The thickness of the Cu layer is

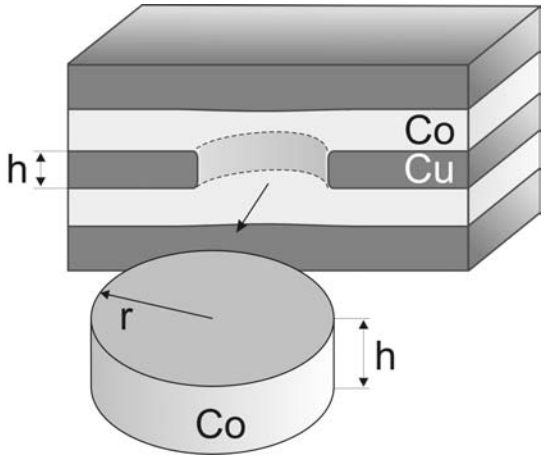

Figure 6.3: Schematic representation of the Co bridge through the Cu layer for calculation of a nucleation barrier for its formation.

denoted by h. Then, the interfacial energy recovered during the Co bridge formation is $2\pi r^2$ (upper and lower areas of the bridge in the plane of the interface) and the energy increase due to creation of new Co-Cu interfaces on the bridge rim is $2\pi rh$. Thus, the change of the systems Gibbs free energy during the Co bridge formation is given by:

$$\Delta G = 2\pi\sigma^{int}(rh - r^2)\,, \tag{6.1}$$

where σ^{int} is the Co/Cu interfacial energy. A critical radius for the Co bridge nucleus, r_{cr}, corresponding to the maximum free energy of the system, ΔG^*, can be found by setting the derivative of the Gibbs free energy in respect to the radius to zero: $r_{cr} = h/2$. Thus, the Co bridge becomes stable after reaching the radius of half the thickness of the Cu layer; further increase of the Co bridge radius lowers the free energy of the system parabolically (see the Fig. 6.4a). The height of the nucleation barrier, ΔG^*, can be expressed as

$$\Delta G^* = \frac{\pi\sigma^{int}}{2}h^2\,, \tag{6.2}$$

and is depicted in Fig. 6.4b versus the Cu layer thickness for the σ^{int}=200 mJ/m^2. As seen from the graph, the nucleation barrier for a 2 nm thick Cu layer is higher than

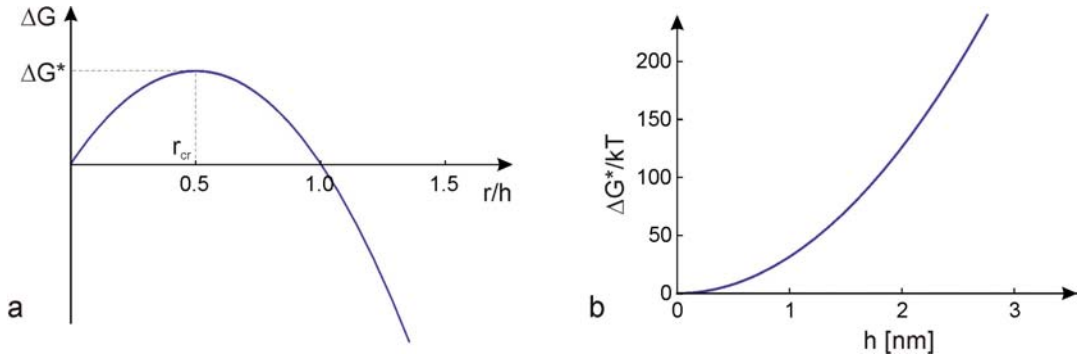

Figure 6.4: Nucleation barrier for Co bridging through the Cu layer. (a) - Dependence of the Gibbs free energy change on the radius of the bridge volume. (b) - Dependence of the nucleation barrier height on the Cu film thickness.

$100\,kT$, which is too high for the nucleation of Co bridges to take place. But due to the parabolic decrease of the nucleation barrier with the decrease of the Cu layer thickness, already at Cu layer thickness of 1 nm, the nucleation barrier is decreased to about $30\,kT$, which is a reasonable value for the formation of overcritical nuclei. It means that the nucleation of Co bridges through Cu layers, which are thicker than 1 nm, occurs on locally thin sites existing due to the finite roughness in the multilayer system or on grain boundaries, which was the case in the TAP observation. Thus, this instructive model is able to explain the observed Co breakthroughs through Cu layers. Obviously, the same model can predict a formation of Cu bridging through Co layers, but probably due to certain kinetic factors, this can occur only at later annealing stages.

6.2 Mismatch induced recrystallization of Py/Cu and Co/Cu multilayer systems

The presented experimental results reveal an important correlation between the lattice mismatch of the single layer materials and the driving force to texture reorientation. In order to understand, why a specific grain orientation may be preferred by thermodynamics, direction-dependent terms of the total free energy of the system have to be carefully analyzed. There are, in general, only two of them: i) the anisotropic elastic energy and ii) the anisotropic interfacial or surface energy. The quantitative assessment of these contributions will allow identifying the controlling driving force. A multilayer with particular structure, $[Ni_{3nm}Cu_{6nm}]_{20}$, is chosen as the main model system to assess the physical parameters. Although, due to the similarity of Py and Co materials, the main conclusions drawn from the analysis are also valid for Co/Cu multilayers. For the sake of simplicity all calculations of elastic and interfacial/surface energies are carried out for the total thickness of model system of $1\,\mu$m, scaling all thickness dependent parameters correspondingly.

6.2.1 Anisotropic elastic energy

Free standing multilayer model

Let us consider two materials with different lattice parameters, a_{m1} and a_{m2}, brought into contact under the epitaxial constraint. There are two principle mechanisms of lattice accommodation in the size mismatched system. The first one relies on the adaptation of in-plane lattice constants by elastic deformation of the constituent materials. The lattice mismatch in both layers is accommodated by the elastic in-plane strains

$$\varepsilon_{m1} = \frac{a^*}{a_{m1}} - 1\,; \qquad \varepsilon_{m2} = \frac{a^*}{a_{m2}} - 1\,, \tag{6.3}$$

Material	c_{11} [GPa]	c_{12} [GPa]	c_{44} [GPa]	B_{111} [GPa]	B_{100} [GPa]	α
Cu [92]	168.4	121.4	75.5	261	115	3.21
$Ni_{79.2}Fe_{20.8}$ [85]	232.4	144.2	120.6	376	198	2.73
β-Co [85]	242	160	128	402	190	3.12

Table 6.1: Literature data for elastic constants at room temperature, biaxial elastic moduli, and anisotropy constants.

leading to a tetragonal distortion of lattices. The intermediate in-plane lattice constant a^* of the compound system depends on the relative thicknesses and elastic properties of the materials involved. A thick layer of elastically hard material is barely strained, whereas a thinner and softer layer is more strongly deformed to accommodate the mismatch. The other possibility is the introduction of interfacial dislocations (misfit dislocations). In this case, the energetic effort of forming the dislocations is compensated by the reduction of elastic strain energy. Since the energy of dislocations is, to a first approximation, proportional only to the interfacial area, while the elastic strain energy is proportional to the strained volume, a critical layer thickness, h_{cr}, exists, above which the formation of misfit dislocations is preferred over the elastic matching of the lattice.

In the case of a thin film sandwiched between much thicker films, the following implicit equation is found for h_{cr} [91]:

$$\frac{h_{cr}}{b} = \frac{2G_{hkl}}{4\pi\varepsilon Y_{hkl}} \left[ln\left(\frac{h_{cr}}{b}\right) + 1 \right] , \tag{6.4}$$

where b is the Burgers vector of the dislocations, G_{hkl} is the shear modulus of the film material and Y_{hkl} is its Young's modulus. In an anisotropic system with cubic symmetry the latter parameters are orientation dependent and can be expressed as:

$$\frac{1}{G_{hkl}} = \frac{1}{c_{44}} - \frac{\alpha - 1}{c_{44}} \Gamma_{hkl} , \tag{6.5}$$

$$\frac{1}{Y_{hkl}} = \frac{c_{11} + c_{12}}{(c_{11} - c_{12})(c_{11} + 2c_{12})} - \frac{\alpha - 1}{c_{44}} \Gamma_{hkl} , \tag{6.6}$$

where c_{11}, c_{12} and c_{44} denote the elastic moduli (see Tab. 6.1). Here and in the following, the parameter α is the anisotropy constant:

$$\alpha = \frac{2c_{44}}{c_{11} - c_{12}} . \tag{6.7}$$

For all the materials considered in this article, α is greater than unity (see Tab. 6.1). The factor Γ_{hkl} describes the dependence on orientation. If the direction perpendicular to the interfaces is expressed by the cosines to the cubic axes (L, M, N), it is given by

$$\Gamma_{hkl} = L^2M^2 + M^2N^2 + N^2L^2 . \tag{6.8}$$

Film material	$h_{cr}^{<111>}$ [nm]	$h_{cr}^{<100>}$ [nm]
Py	7.6	7.7
Co	12.0	9.0
Cu	13.8	9.7

Table 6.2: Critical layer thicknesses at 450 °C of epitaxial Py and Co layers sandwiched between much thicker Cu layers and epitaxial Cu layer sandwiched between much thicker Py or Co (the same due to identical lattice parameters of Py and Co) layers.

With the following expression, the direction cosines may be related to specific *hkl* indices:

$$L, M, N = \frac{h, k, l}{\sqrt{h^2 + k^2 + l^2}} \,. \tag{6.9}$$

The estimated h_{cr} for the Py and Co films sandwiched between much thicker films of Cu are given in Tab. 6.2. A much smaller value of h_{cr} ≈2.0 nm has been reported for epitaxially deposited Co on single crystalline Cu substrate by Jesser et al. [41]. However, in that case the Co layer was bonded to the substrate only on one side and not sandwiched between Cu layers as it is the case for multilayers. In sandwiched films, dislocation dipoles have to be formed to accommodate the mismatch, and these have higher energies of formation than ordinary dislocations. Furthermore, due to the compliance of Py, Co and Cu, the accommodation of the mismatch can be shared between the different constituent layers in the system. Since this decreases the stress field of the system considerably, the first strain-relieving dislocation will appear at even higher critical thicknesses than listed in Tab. 6.2. Since the multilayers considered here have single layer thicknesses below the limits stated in Tab. 6.2, ideal coherent interfaces without formation of misfit dislocations can be expected. High-resolution transmission electron micrographs as depicted in Fig. 6.5 confirm the expected coherent structure of the studied $[\mathrm{Py}_{3\,nm}\mathrm{Cu}_{6\,nm}]_{20}$ system.

For the ideal epitaxial case (as it is observed in studied multilayers due to the high grain size values after the recrystallization and coherency of interfaces), the magnitude of the elastic energy density can be calculated for the NiFe/Cu model system with layer thicknesses of 3 and 6 nm for NiFe and Cu, respectively. According to Eq. 2.44, the elastic energy density per unit film area for biaxial in-plane stress is:

$$E_{el} = \left(B_{hkl}^{Cu}\varepsilon_{Cu}^2 h_{Cu} + B_{hkl}^{NiFe}\varepsilon_{NiFe}^2 h_{NiFe}\right) n \,, \tag{6.10}$$

where B_{hkl}^{x} is the appropriate biaxial elastic modulus, ε_x is the strain of the corresponding layer, h_x is the corresponding film thickness, and n the number of double layers in a multilayer of given total thickness. The biaxial elastic modulus is given by [91]:

$$B_{hkl} = \left(\frac{c_{11} + 2c_{12}}{2}\right)\left(3 - \frac{c_{11} + 2c_{12}}{c_{11} + 4c_{44}(1 - \frac{1}{\alpha})\Gamma_{hkl}}\right) . \tag{6.11}$$

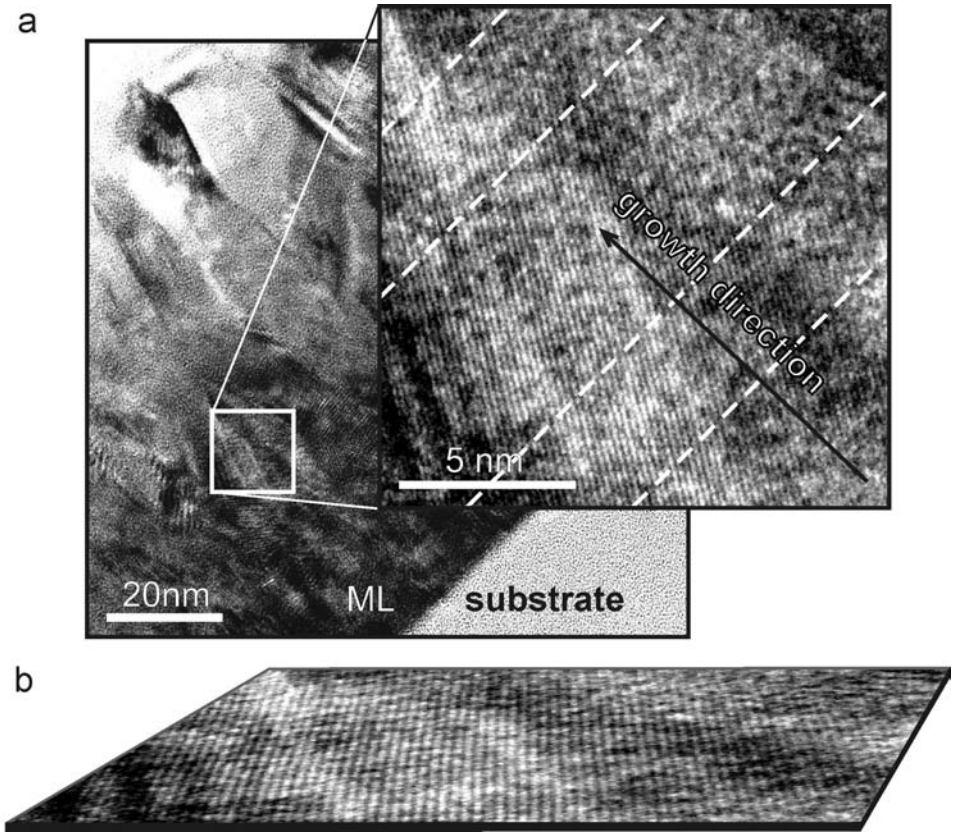

Figure 6.5: High-resolution transmission electron micrographs of the Py/Cu cross-sectioned multilayer system. (a) Overall multilayer view with magnified region showing the (111) planes going through five metallic layers (in the absence of the layer contrast, possible positions of the layer interfaces deduced from the scale and layer thicknesses are shown with dashed lines). (b) Glancing angle perspective view of the same micrograph as shown in (a) in order to clarify the absence of dislocations.

Analyzing Eqs. 6.8 and 6.9, it is seen that the factor Γ takes its minimum of 0 for the <100> direction and its maximum value of $\frac{1}{\sqrt{3}}$ for the <111> direction. Thus, the biaxial elastic modulus B_{hkl} has its minimum value for <100> and its maximum for <111>, and in consequence, the elastic energy of the system has its extremum values for the <100> (minimum) and <111> (maximum) directions of the interface. This reflects the experimental <111> to <100> texture reorientation. The specific values of B_{hkl} for the analyzed materials are also listed in Tab. 6.1.

The strain of the respective layer material is defined by Eq. 6.3:

$$\varepsilon_{NiFe} = \frac{a^*}{a_{NiFe}} - 1\,; \qquad \varepsilon_{Cu} = \frac{a^*}{a_{Cu}} - 1\,. \tag{6.12}$$

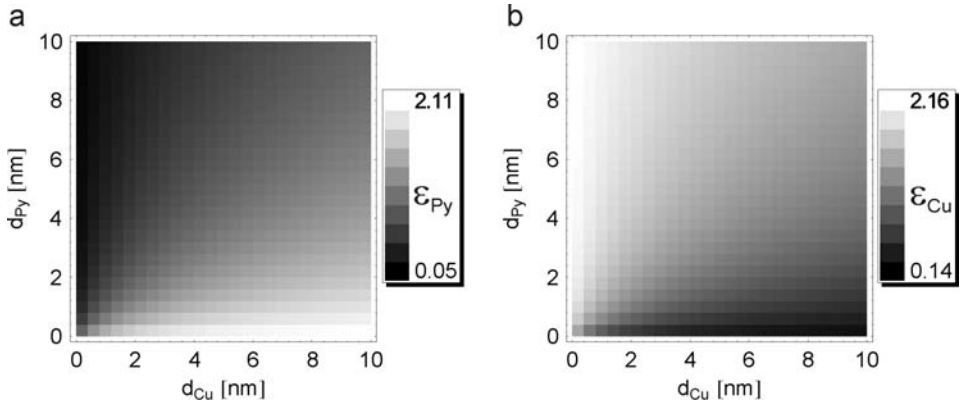

Figure 6.6: Elastic strain in $Ni_{80}Fe_{20}$ (a) and Cu (b) layers at 450 °C vs. single layer thicknesses in the $Ni_{80}Fe_{20}$/Cu multilayer depicted in grades of gray (white, maximum value; black, minimum value).

Furthermore, the strain in the Cu layer can be expressed by the strain in the NiFe layer:

$$\varepsilon_{Cu} = \frac{(\varepsilon_{NiFe} + 1)a_{NiFe}}{a_{Cu}} - 1\,. \tag{6.13}$$

If the total elastic energy, Eq. 6.10, is minimized with respect to the strain in the NiFe layer:

$$\frac{\partial E_{el}}{\partial \varepsilon_{NiFe}} = 0\,, \tag{6.14}$$

the strain in the NiFe layer can be determined as:

$$\varepsilon_{NiFe} = \frac{a_{NiFe}(a_{Cu} - a_{NiFe})}{\beta a_{Cu}^2 + a_{NiFe}^2}\,; \tag{6.15}$$

$$\beta = \frac{t_{NiFe}}{t_{Cu}} \frac{B_{hkl}^{NiFe}}{B_{hkl}^{Cu}}.$$

Eq. 6.15 expresses the dependence of the elastic strain on the relations of respective elastic constants and single layer thicknesses, denoted by the factor β. This dependence was already mentioned in the beginning of this section. It is demonstrated in Fig. 6.6. It is seen that the stiffer NiFe layers are strained to a smaller degree than the softer Cu layers; only at small thicknesses of NiFe layers and high thicknesses of Cu, strain of NiFe dominates. Finally, based on Eqs. 6.10, 6.11, 6.13 and 6.15, the absolute values of the elastic energy density can be calculated.

Taking into account the thermal activation of recrystallization, appropriate corrections for the temperature dependence of the material properties have to be made. Namely, the lattice parameters of the materials involved and their stiffness constants have to be corrected. The coefficients of thermal expansion and the temperature coefficients of the elastic moduli are presented in Tab. 6.3 and 6.4, respectively. Not all the parameters

Material	T [°C]	$\alpha\times10^6$ [1/K]	$\beta\times10^9$ [1/K^2]	$\gamma\times10^{12}$ [1/K^3]
Cu [93]	20...825	15.89	4.492	3.888
$Ni_{80}Fe_{20}$ [94]	0...500	10.4	4.7	0.5
β-Co [93]	20...100	12.5	0	0
Si [93]	18...950	3.6	0	0

Table 6.3: Thermal expansion coefficients: linear (α), quadratic (β), and cubic (γ).

Material	T [°C]	$Tc_{11}\times10^4$ [1/K]	$Tc_{12}\times10^4$ [1/K]	$Tc_{44}\times10^4$ [1/K]
Cu [95]	27...527	-2.36	-3.51	-1.63
$Ni_{75}Fe_{25}$ [95]	-193...27	-2.28	-2.84	-0.4

Table 6.4: Linear thermal coefficients of the elastic moduli (data for Co are not available).

are available in the required temperature range, but their influence on the calculations performed here is small. In Fig. 6.7a the lattice parameters of $Ni_{80}Fe_{20}$-alloy and Cu as well as the mismatch between the two lattices, η, are shown vs. temperature for the model NiFe/Cu multilayer. Due to the higher thermal expansion coefficients of Cu compared with $Ni_{80}Fe_{20}$, the absolute value of the elastic in-plane strain in the metallic layers increases with temperature (Fig. 6.7b). Although the biaxial elastic moduli of layer materials are somewhat lowered at high temperatures, the elastic energy density increases due to the quadratic dependence on strain, as depicted in Fig. 6.7c. This increase amounts to about 20 % and 24 % for NiFe/Cu and Co/Cu multilayers, compared to values at room temperature.

The energy gain depicted in Fig. 6.7 is calculated for a near-ideal situation, assuming that initially all the material of the multilayer is <111> oriented, and that it transforms completely into the <100> orientation. This is not fulfilled experimentally, where the initial <111> texture is considerably broad. In consequence, the elastic energy gain for a transformation of grains with initial orientation different from the dominant <111> into the <100> orientation is also of interest. Fig. 6.8 demonstrates the dependence of the elastic energy density at 450 °C on the orientation. In the density plot, the energy values are depicted in gray grades vs. the direction cosines of the layer normal to the cubic axes (in the insert a corresponding three-dimensional representation is shown). This representation resembles the standard (001) stereographic projection. But in a strict sense, it represents an orthogonal projection. For convenience, some *hkl*-indices are indicated in the figure. The main feature of the energy density configuration is a sharp minimum and a broad maximum around the <100> and <111> directions,

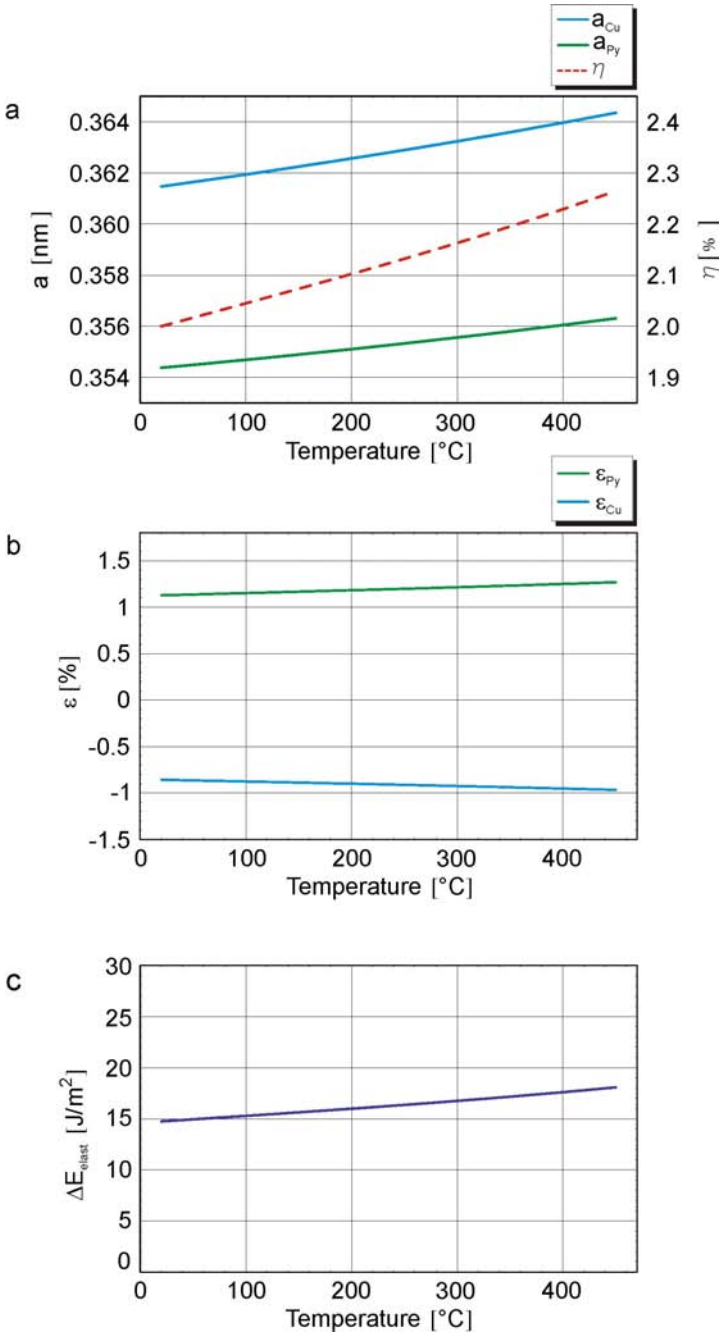

Figure 6.7: (a) Temperature dependence of the Cu and $Ni_{80}Fe_{20}$ lattice parameters and lattice mismatch. (b) Temperature dependence of strain in Cu and $Ni_{80}Fe_{20}$ layers as determined by Eqs. 6.15 and 6.13. (c) Temperature dependence of elastic energy gain due to the <111> to <100> texture reorientation.

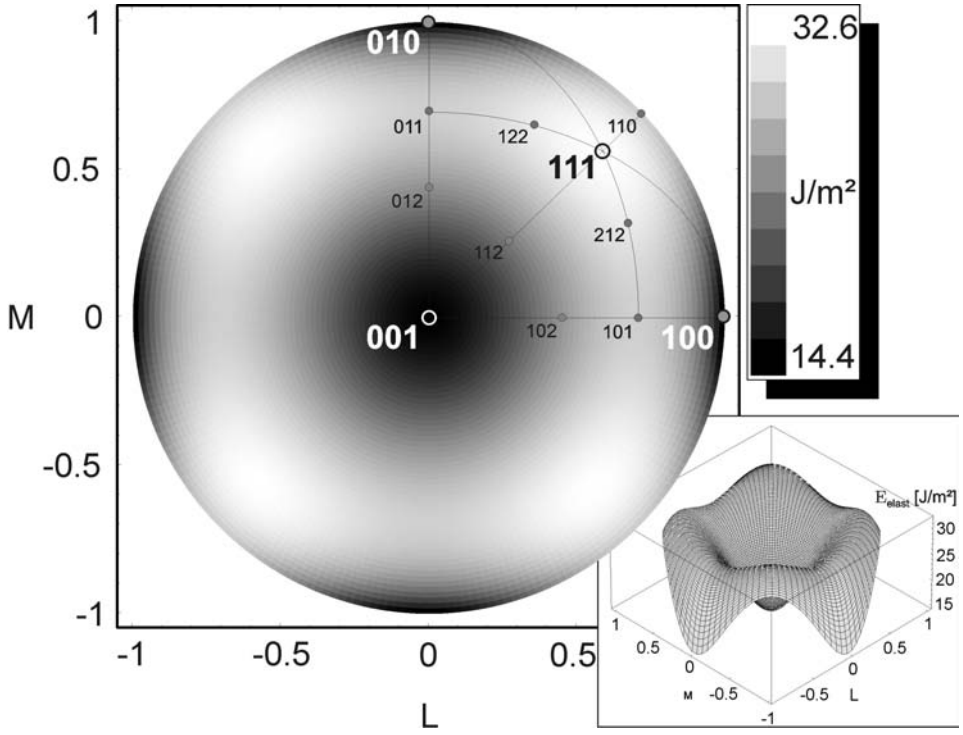

Figure 6.8: Elastic energy density of a $Py_{3\,nm}/Cu_{6\,nm}$ multilayer with a total thickness of $1\,\mu$m vs. direction cosines of the normal to the interface. The energy density values are represented in gray grades according to the plotted scale. In the smaller insertion, a 3D representation of the same energy is shown.

respectively. Therefore, within the qualitative context of the calculations, the influence of the initial scatter of crystallographic orientations is minor.

Substrate defined strain field

Up to now, the influence of the substrate on the strain field in the system was not considered. The model described above assumes a free standing multilayer or a multilayer without rigid bonding to substrate, which is not the case in the experiments. Due to different thermal expansion coefficients of the Si substrate and the metallic multilayer stack (see Tab. 6.3), the strain field of the multilayer is significantly affected at high temperatures. It is assumed that at room temperature, the temperature of deposition, the multilayer stack rests on the substrate without mismatch, having the in-plane lattice parameter a^* defined by the elastic energy minimization condition (Eq. 6.14). Mismatch is absent due to the amorphous structure of the substrate surface (thermally oxidized Si). At room temperature, the elastic energy is defined by the mode for a free standing multilayer. However, with increasing temperatures, the strains of the respective layer materials may become controlled by the thermal expansion of the substrate, so that the

	$\sigma^{<111>}$ [GPa]	$\sigma^{<100>}$ [GPa]
$\sigma_{Ni_{80}Fe_{20}}$	2.4	1.0
σ_{Cu}	-3.4	-1.5
σ_b	1.5	0.7
σ_y^{ML}	3.5	2.3

Table 6.5: Elastic mismatch stresses in $Ni_{80}Fe_{20}$ and Cu layers after substrate-defined strain field model; absolute values of balanced stress and yield stress for the averaged multilayer material at <111> and <100> fibre textures.

strain at the annealing temperature is given by:

$$\varepsilon_{NiFe_T} = \frac{a^*_{Si_T}}{a_{NiFe_T}} - 1\,; \qquad \varepsilon_{Cu_T} = \frac{a^*_{Si_T}}{a_{Cu_T}} - 1\,, \tag{6.16}$$

where $a^*_{Si_T}$ is the initial in-plane lattice parameter of the metallic stack a^* expanded in accordance with the coefficient of thermal expansion of the Si substrate; a_{NiFe_T} and a_{Cu_T} are the lattice parameters of the metallic layers taking into account the thermal expansion of the corresponding material. As the Si material has much smaller coefficients of thermal expansion than the metals, at elevated temperatures the intermediate lattice parameter of the multilayer approaches the bulk value of the material with the smallest lattice constant (NiFe). It diminishes its tensile strain (in fact, the strain can even become compressive for the multilayers with d_{NiFe}/d_{Cu}>1) and induces much higher compressive strains in the material with the largest lattice parameter (Cu), which concentrates the major amount of systems elastic energy. Fig. 6.9a demonstrates this behavior. The elastic energy density vs. the annealing temperature is depicted in Fig. 6.9b. As seen from the figure, this more realistic model yields a higher value of elastic energy gain by the <111> to <100> texture reorientation. The relative increase compared to the room temperature amounts as much as 56 percent for NiFe/Cu system. The same relative increase of the elastic energy gain takes place in the Co/Cu system. However, because of the higher stiffness of Co compared to NiFe, the absolute elastic energy gain in Co/Cu system is larger than those in Ni/Fe multilayers (see Fig. 6.10). The main features of the elastic energy dependence on the crystallographic orientation of layer interfaces remain the same as for the previous model (see Fig. 6.8); only the absolute values need to be corrected.

One should acknowledge the high stress fields in the individual NiFe and Cu layers, σ_{NiFe} and σ_{Cu}, reaching several gigapascals (particular stress values are given in Table 6.5). However, of greater importance for the mechanical stability of the substrate-multilayer interface is the balanced stress value, σ_b, which describes the force acting from the side of substrate on the multilayer as a whole. It is defined as the thickness-weighted average of the individual stresses:

$$\sigma_b = \frac{\sigma_{NiFe} t_{NiFe} + \sigma_{Cu} t_{Cu}}{t_{NiFe} + t_{Cu}}\,, \tag{6.17}$$

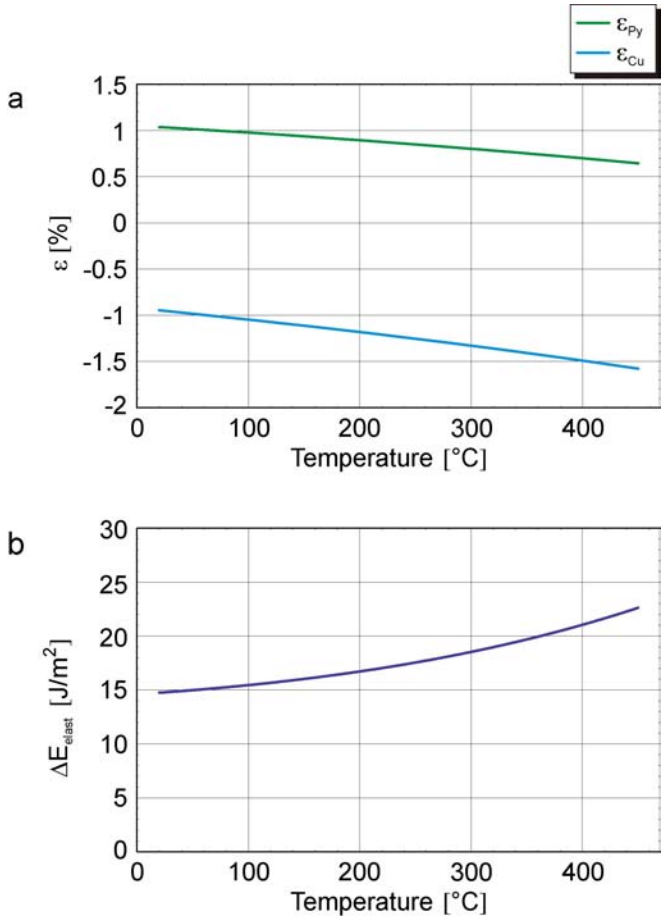

Figure 6.9: (a) Temperature dependence of substrate-defined strain in Cu and $Ni_{80}Fe_{20}$ layers. (b) Temperature dependence of elastic energy gain due to the <111> to <100> texture reorientation in NiFe/Cu multilayer system.

where t_{NiFe} and t_{Cu} are the thicknesses of the correspondent layers. In other words, σ_b is the deviation from the equilibrium condition of zero net force acting on any plane perpendicular to the interface. In the absence of traction between the multilayer and the substrate (the free standing multilayer model) the left-hand side of the equation would equal zero. The values of σ_b for <111> and <100> textures are given in the Table 6.5.

For comparison, the typical yield stress, σ_y, for metals in the bulk do not exceed several tens of megapascals. However, it is widely known that in the case of thin polycrystalline films, the yield stresses can reach much higher values, up to several gigapascals. It is obvious that the elastic energy increases during a deformation as long as the mechanical stress in the system is less than σ_y. At higher stresses, the elastic strain energy remains almost constant and may be estimated by the value of σ_y. Also, as argued by Sanchez et al. [96], due to σ_y being texture dependent, films with some predominant texture will yield before those with another texture. Therefore, an orientational dependence of the strain energy would be induced even in the case of isotropic materials. Thus,

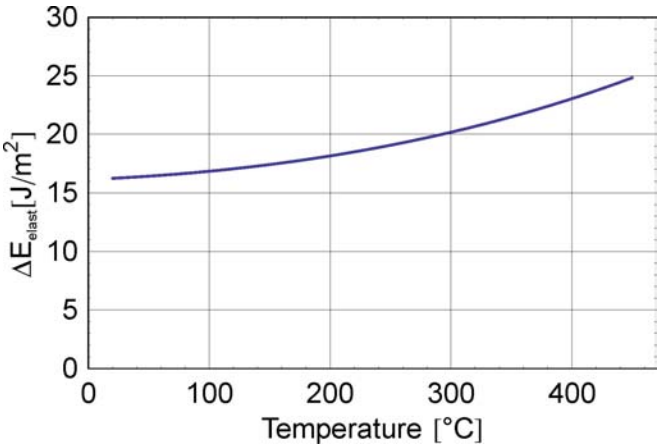

Figure 6.10: Temperature dependence of elastic energy gain due to the <111> to <100> texture reorientation for Co/Cu multilayer system.

yielding of the multilayer material may change not only the absolute value but also the established directional dependence of the system's elastic energy. Therefore, it is of great importance here to assess the yield stress and compare it with the balanced stress formulated above.

To estimate the yield stress of a polycrystalline multilayer film, calculations of the yield stress of a polycrystalline monolayer film proposed by Thompson [61] can be adapted. The yield stress of the system is given by:

$$\sigma_y = C_{hkl}\left(\frac{2\,W_S}{b\,d\,sin\phi_{hkl}} + \frac{W_B}{b\,h}\right)\,, \tag{6.18}$$

where C_{hkl} is a factor depending on the orientation of the glide system for the $< hkl >$ texture (C_{111}=3.46 and C_{100}=2.00 [46]), ϕ_{hkl} is the angle between the normal to the slip plane and the normal to the layer interface plane for the $< hkl >$ texture (ϕ_{111}=70.5° and ϕ_{100}=54.7°), d is the in-plane grain diameter, h is the grain thickness perpendicular to the layer interface, b is the Burgers vector of dislocation, W_S and W_B are the energies per unit length of the dislocation directed along the sides and bottoms of the grain, respectively. For the case of a multilayer, these energies are approximated by:

$$W_S = \frac{\mu_f\,b_f^2}{4\,\pi\,(1-\nu_f)} ln\left(\frac{d}{b_f}\right) \tag{6.19}$$

and

$$W_B = \frac{b_f^2}{4\,\pi\,(1-\nu_f)}\,\frac{2\,\mu_f\,\mu_s}{\mu_f+\mu_s} ln\left(\frac{h}{b_f}\right)\,, \tag{6.20}$$

where indices f and s denote the averaged layer material (thickness weighted average of corresponding material properties) and the substrate material, respectively, and μ_f and μ_s are the shear moduli (μ_{Cu}=48.5·10^9 Pa [97], μ_{NiFe}=77·10^9 Pa [98], and μ_{Si}=66.5·10^9 Pa [46]),

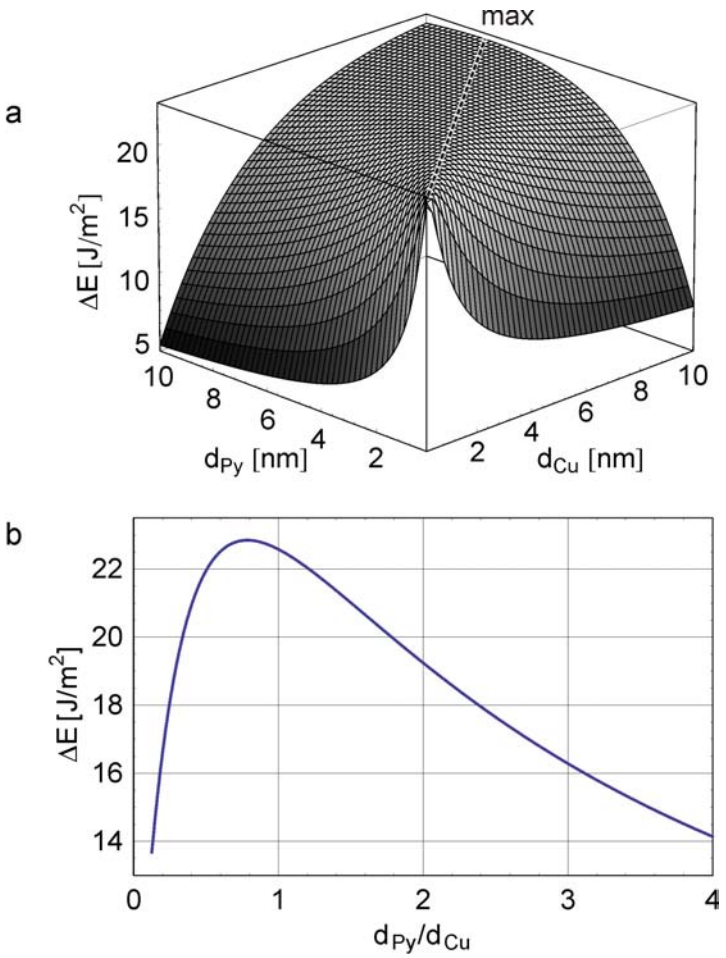

Figure 6.11: (a) Elastic energy gain vs. single layer thicknesses of $Ni_{80}Fe_{20}$/Cu multilayer system, (b) Elastic energy gain vs. layer thickness ratio.

and ν_f is the Poisson's ratio (ν_{Cu}=0.37 [97] and ν_{NiFe}=0.29 [98] as interpolated from pure Ni and Fe data). The yield stresses σ_y obtained using Eq. 6.18 (for columnar grains with d=15 nm and h=180 nm) are compiled in the Table 6.5. It should be noted that the estimate of the yield stress is well above the balanced stress of the system. In consequence, it can be concluded that no yielding occurs in the model system, so that no further corrections are needed for the evaluation of the elastic energy density made above. Even if the yield stress would be reached, the <100> orientation would be preferred due to $\sigma_y^{111} > \sigma_y^{100}$. In fact, even higher elastic energy gain would be expected.

Dependence on the multilayer architecture

Both approaches discussed in this section give us in principle identical results concerning the elastic energy density and its anisotropic behavior. Using the elasticity model described, it is possible to predict some key features observed experimentally.

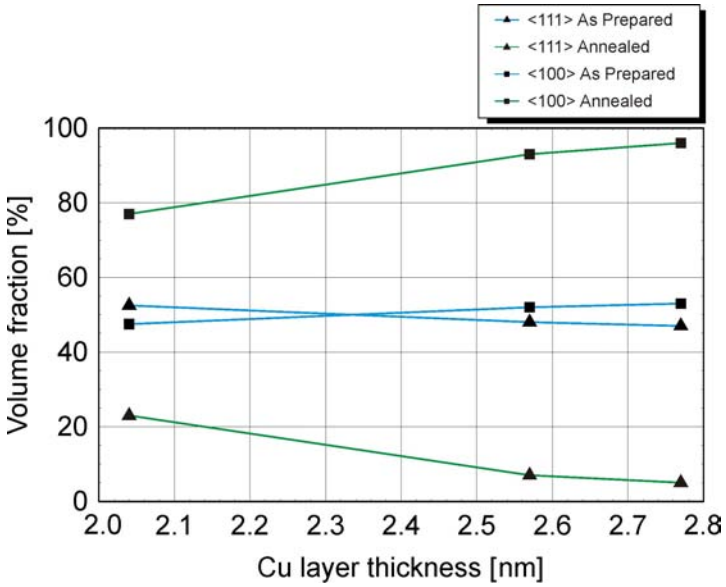

Figure 6.12: Experimentally determined volume fractions of crystallites with <111> and <200> orientation in as-prepared and annealed states for $[Co_{2.0\,nm}/Cu_{t_{Cu}}]_{40}$ multilayers in dependence on Cu thickness (from Ref. [12]).

For example, let us derive the best multilayer architecture in order to get the highest recrystallization probability. That is, the single layer thickness ratio has to be found that provides the highest possible elastic energy gain during the <111> to <100> texture reorientation. In Fig. 6.11a this energy gain is depicted vs. the single layer thicknesses of Cu and $Ni_{80}Fe_{20}$. The asymmetry of layer thicknesses is clearly seen in Fig. 6.11b - the maximum is reached at $d_{Py}/d_{Cu} \approx 0.8$. Indeed, the preliminary investigations of Py/Cu and Co/Cu multilayers revealed a poor recrystallization probability for the systems with symmetric layer thicknesses. For that reason, the main series of experiments were done using a system with Cu layers thicker than NiFe layers. Although the maximum elastic energy gain is quite broad, this correspondence between experimental and theoretical data justifies the basic concept of the model. Also the Co/Cu multilayer system reveals this feature, as it is expected due to the similarity of the elastic properties of Co and $Ni_{80}Fe_{20}$. It is also worth to mention that though the dependence shown in Fig. 6.11b holds for all correspondent thicknesses of Cu and Py (Co) layers, the layer thickness tolerance for the maximum energy gain becomes tighter for small layer thicknesses (see the Fig. 6.11a). It means that in order to obtain multilayers with the highest recrystallization probability, the thickness accuracy of the deposited layers has to be increased with the decrease of the multilayer periodicity during the manufacturing process. The experimental dependence of the degree of texture reorientation on the Cu layer thickness in the Co/Cu system is demonstrated in Fig. 6.12.

In conclusion, the elastic energy gain by the <111> to <100> texture reorientation will be assessed for the $Ni_xFe_{(1-x)}/Cu$ multilayer with different Fe contents in the NiFe layers. For that the lattice parameter of the $Ni_xFe_{(1-x)}$-alloy is defined using Vegard's law, i.e.

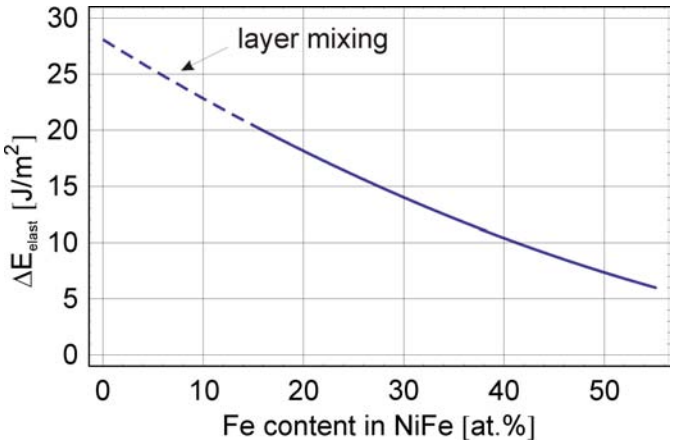

Figure 6.13: Elastic energy vs. iron content in $Ni_xFe_{(1-x)}$ layers. The dashed part of the curve is of limited relevance due to mixing of layers.

by linear interpolation between pure Ni and pure fcc Fe as shown in Fig. 5.4. Due to the decrease in the lattice mismatch between pure Cu and $Ni_xFe_{(1-x)}$ alloy with higher Fe contents, x, the elastic energy of the model system is expected to be reduced with increasing iron concentration, thereby reducing the driving force for grain growth and texture reorientation. The dependence of elastic energy on the Fe content is depicted in Fig. 6.13. This mimics to some degree the behavior of the recrystallization probability observed experimentally (Fig. 5.5).

As was argued in a previous section, at low Fe content (smaller than about 15%) the mixing of layers takes place due to good Ni-Cu miscibility. This mixing relieves the elastic energy, thereby diminishing the driving force for texture reorientation. Unfortunately, it is not a trivial task to find the elastic constants and their temperature dependence for different Fe contents in NiFe. However, due to the similarity of Fe and Ni only small deviations are expected. In general, with higher Fe content the $Ni_xFe_{(1-x)}$ is expected to become softer, which will just enhance the effect of driving force reduction.

6.2.2 Anisotropic interfacial/surface energy

Interfacial and surface energies are important in considering the microstructure in very thin single layers and multilayer systems with nanometer-scale periodicity. Since thin films have just only one free surface (or two for free-standing films), the effects related to surface energy and its anisotropy dominate at small film thicknesses and become negligible for thicker films. Multilayer systems, in turn, have additional free energy due to the bonding of different constituent materials. This interfacial energy depends on the density of interfaces (number of interfaces per multilayer thickness) and can reach very high values for a system of small periodicity. Thus, GMR systems, which have a typical periodicity of few nanometers only, possess a high amount of interfacial energy. It may

be expected, therefore, that texture changes will be initialized or at least affected by the anisotropy of interfacial/surface energy.

It is known that the relation $\sigma_{111}^{int,surf} < \sigma_{100}^{int,surf}$ holds for the interfacial/surface energies of fcc metals, with $\sigma_{111}^{int,surf}$ being the global minimum. This is explained naturally by the minimum of out-of-plane bonds between closed-packed {111} planes. Thus, interfacial energies should drive microstructural reactions in the opposite direction to the observed $< 111 >$ to $< 100 >$ texture reorientation. Hence, for comparison of elastic energy gain and interface/surface energy gain during texture reorientation, the values of interface and surface energies and their dependence on the crystallographic orientation have to be carefully analyzed. Finding literature values for the dependence of interfacial and surface energies on crystallographic orientation for particular pure materials is not a trivial task, and in the case of alloy materials, e.g. Py, these data are even more sparse. Thus, in this section the Co/Cu system will be used for evaluation as the required data are more readily available. Since Co, Fe and Ni are very similar materials, the conclusions drawn for Co/Cu are than applied to the Py/Cu model system with minimal required corrections.

In order to estimate the dependence of the interfacial energy on the crystallographic orientation in the system with coherent boundaries, the sharp interface model can be used, which was first suggested by Becker in 1938. This model assumes that the interface energy is the product of the atomic bonds density crossing the unit area of the interface plane, ν_{hkl}, and the pair exchange parameter $\epsilon_{mix} = \epsilon_{AB} - (\epsilon_{AA} + \epsilon_{BB})/2$ of the appropriate regular solution model

$$\sigma_{hkl}^{int} = \nu_{hkl}\epsilon_{mix} \,. \tag{6.21}$$

This simple ansatz neglects any relaxation of the atoms at the interface and further peculiarities of the real atomic potentials of the considered materials. However, it provides an estimate of the orientational dependence to a first approximation. In order to find how the density of the bonds across the boundary depend on its crystallographic orientation, the six different types of next-neighbor bonds are considered separately. This bonds are described by the following vectors: $\vec{l^i}$=$a(0\ \frac{1}{2}\ \frac{1}{2})$, $a(0\ \frac{1}{2}\ \frac{\bar{1}}{2})$, $a(\frac{1}{2}\ 0\ \frac{1}{2})$, $a(\frac{\bar{1}}{2}\ 0\ \frac{1}{2})$, $a(\frac{1}{2}\ \frac{1}{2}\ 0)$, $a(\frac{1}{2}\ \frac{\bar{1}}{2}\ 0)$, with a being the lattice parameter.

In Fig. 6.14a the bonds of a specific type, $\vec{l^i}$, are depicted for the purposes of illustration. The volume density of the bonds of each type equals to $\rho = \frac{4}{a^3}$. In order to determine the total number of bonds across an interface of arbitrary orientation, the effective thickness of the interfacial zone for a given bond type, $d_{hkl}^{(i)}$, is calculated by the projection of the bond vector $\overrightarrow{l^i}$ onto the interface normal (see Fig. 6.14b):

$$d_{hkl}^{(i)} = |(\overrightarrow{l^i} \cdot \overrightarrow{n}_{hkl})| \,. \tag{6.22}$$

Taking into account the constant volume density of bonds, the number of bonds across the interface follows as:

$$\nu_{hkl}^{(i)} = \rho d_{hkl}^{(i)} \,. \tag{6.23}$$

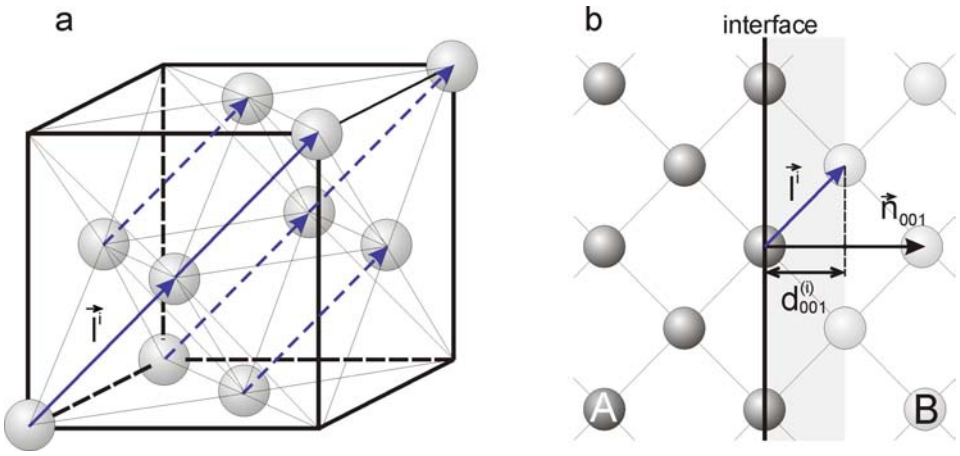

Figure 6.14: Drawings for interfacial/surface energy calculation in fcc material. (a) All next-neighbor bonds of specific bond type $\vec{l^i}$. (b) Exemplary effective thickness of the <001> oriented interface, d^i_{001}, between A and B species atoms. Shaded region corresponds to the interfacial zone separating the materials.

Finally, the contributions of all bond types have to be summed up, thus:

$$\nu_{hkl} = \sum_i \nu^{(i)}_{hkl} \,. \tag{6.24}$$

The values of ν_{hkl} for some low-indexed, high-symmetry orientations, following Eqs. 6.22 and 6.24, are given in Table 6.6. Scaling the ν_{hkl} with the pair exchange parameter of Co/Cu ($\epsilon_{mix} = 4.898 \cdot 10^{-21}$ J [99]) in accordance with Eq. 6.21, gives a graph similar to that for the elastic energy (Fig. 6.8) for the anisotropic interfacial energy, as presented in Fig. 6.15. As can be seen, the distribution has minium values around highly symmetrical interface orientations with Miller indices of the type $< hkk >$ and its global minimum at <111>. Large values of ν_{hkl} are found at orientations with poor symmetry with the global maximum at <102> orientations. During recrystallization, grains with poor symmetry orientations are unfavorable due to significantly higher interfacial energies. The values of interfacial energies are given in Table 6.6. There is a good principal agreement between the calculated values and experimental values found in the literature, $\sigma^{int} \approx$240 mJ/m^2 (measured for Co-rich precipitates in a Cu-rich matrix) [99, 100, 101], maintaining the known orientational relations ($\sigma^{int}_{111} < \sigma^{int}_{100} < \sigma^{int}_{110}$).

The values calculated this way are to some degree overestimated due to the assumption of atomically sharp interfaces between the layers with an unrelaxed lattice structure, which is certainly not the case for real interfaces. Also the ratios of $\sigma^{int}_{hkl}/\sigma^{int}_{111}$ given in Table 6.6 are generally higher compared to values obtained from more accurate models. For example, the full charge density method yields for pure Cu: $\sigma_{100}/\sigma_{111}$=1.08, $\sigma_{110}/\sigma_{111}$=1.15 [102]. The total interfacial/surface energy, σ^{total}_{hkl}, in the $[\mathrm{Co}_{3\,nm}/\mathrm{Cu}_{6\,nm}]_{20}$ multilayer (scaled for 1 μm total multilayer thickness) including the additional surface

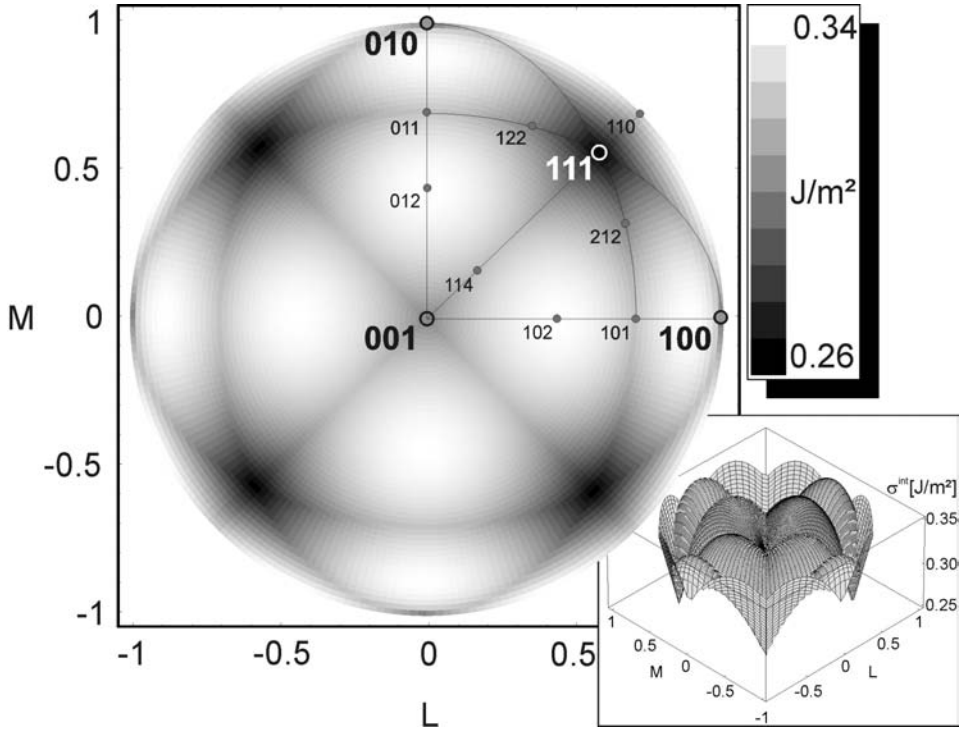

Figure 6.15: Interfacial energy density of $Co_{3\,nm}/Cu_{6\,nm}$ bilayer vs. direction cosines of the normal to interface. The energy density values are represented in gray grades with black being the minimum and white the maximum values. In the insertion, a 3D representation of the same energy configuration is shown.

energy of the outermost Cu layer ($\approx 1.8\,J/m^2$ [103, 104]) is shown in Table 6.6 for different interface orientations.

Due to the miscibility of Ni and Cu, the NiFe/Cu interfacial energy at low Fe content is expected to be lower than that of Co/Cu, or even negative. However, from the experimental observation that even at elevated temperatures only weak intermixing between Py and Cu layers takes place, one can conclude that the system still has a positive mixing energy. Thus, at the ideal Fe content of Py, the interfacial energy should be positive but significantly lower than that of Co/Cu. Together with the increase in the Fe content, the interfacial energy of NiFe/Cu will increase and approach the Co/Cu value for high Fe contents.

6.2.3 Comparison of elastic and interfacial/surface energy gains during the texture reorientation

Now the gains of elastic and interfacial/surface energy by the observed <111> to <100> texture reorientation can be compared and conclusions about the driving force for this

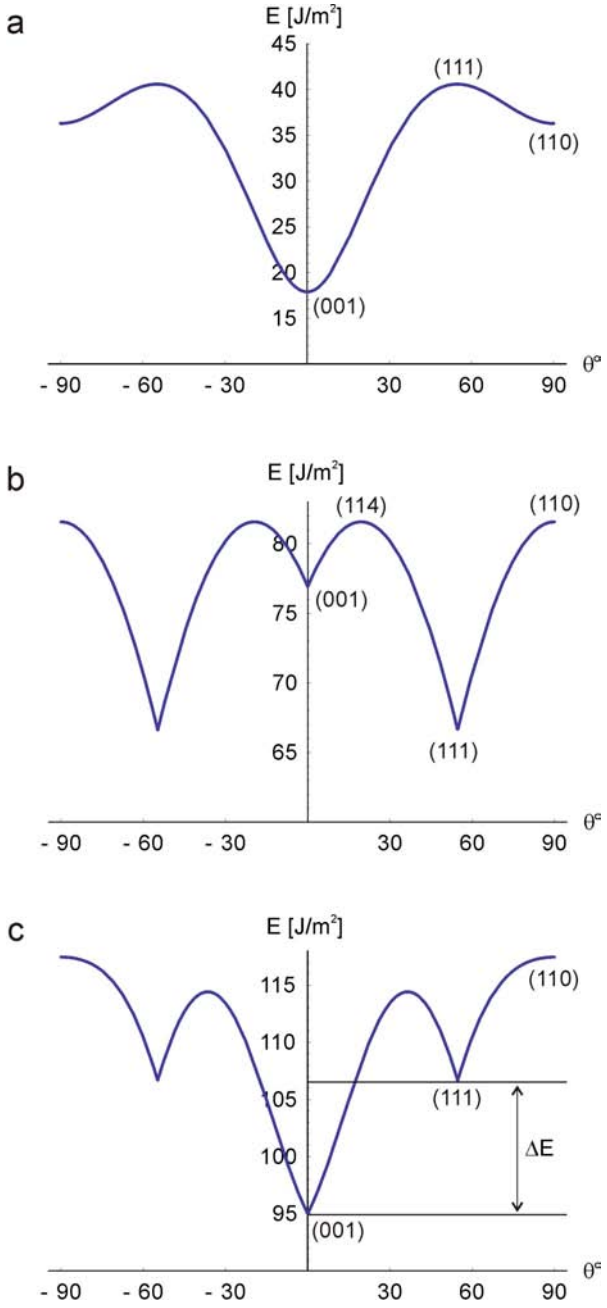

Figure 6.16: Anisotropic energy terms along the {hkk} line in the stereographic projection: (a) elastic energy; (b) interfacial/surface energy; (c) sum of elastic and interfacial/surface energies.

Interface plane	ν_{hkl}	σ^{int}_{hkl} [mJ/m^2]	σ^{total}_{hkl} [J/m^2]	$\sigma^{int}_{hkl}/\sigma^{int}_{111}$	Notice
{111}	$\frac{4\sqrt{3}}{a^2}$	261	66.6	1	global minimum
{100}	$\frac{8}{a^2}$	301	76.7	1.15	local minimum
{110}	$\frac{6\sqrt{2}}{a^2}$	320	81.5	1.22	average value
{102}	$\frac{4\sqrt{5}}{a^2}$	337	85.9	1.29	global maximum

Table 6.6: Density of bonds across the interface, interfacial energy density for different interface orientations, and their relations to the σ^{int}_{111}.

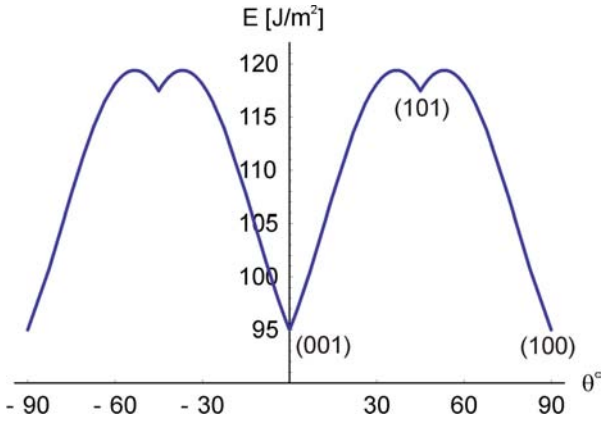

Figure 6.17: Sum of elastic and interfacial/surface energies along the {hk0} line of the stereographic projection.

transformation can be drawn. For this comparison, we take the elastic energy of Py/Cu system calculated within the more realistic substrate-defined strain field model and the Co/Cu interfacial/surface energy (keeping in mind that it is larger than that of Py/Cu). Let us compare the relative energy terms along the *hhl* line in the stereographic projection, i.e. the line containing the major crystal planes: (001), (111) and (110). In Fig. 6.16a-c the corresponding energy terms are depicted. As one can see, even though the interfacial/surface energy stabilizes the <111> texture, the minimization of elastic energy by the <111> to <100> texture transformation yields a greater energy release. Even in the case of overestimated interfacial/surface energy for the NiFe/Cu system, the total gain of free energy for the total multilayer thickness scaled to 1 μm amounts to about 12 J/m^2 (or about 14 J/m^2 for Co/Cu system). These values are very large; e.g., the same order of magnitude energy saved in grain boundaries and lattice defects can trigger the recrystallization of material. If the orientational scatter of the initial texture is also considered, a somewhat higher driving force is expected, as seen from Fig. 6.16c. In fact, due to the contribution of the interfacial energy, random orientations deviating from the exact <111> are even more unstable. This can explain the experimental observation that though the <111> orientation has the largest elastic

energy, it never disappears completely after the recrystallization. In some cases, the intensity of {111} peaks remains constant or even slightly increases. This means that <100> grains grow preferentially at the expense of randomly oriented grains. This can be better demonstrated by drawing the sum of elastic and interfacial/surface energy terms along the the $h0l$ line in the stereographic projection, i.e., the line containing the major crystal planes: (001), (101) and (100) (see Fig. 6.17). It is clearly seen that the <100> texture possesses a much lower free energy compared to random orientations.

The energy configuration shown in Fig. 6.16c also explains the fact that the system maintains its as-deposited <111> texture already at 50 at.% Fe, though the lattice mismatch, and thus the elastic energy, is not yet zero. The quantitative calculations show that taking into account both anisotropic contributions to the free energy, the gain of the texture reorientation vanishes already at 50-55 at.% Fe due to the additional interfacial contribution. Although the calculations presented here have only a demonstrative character, this agreement is remarkable.

These considerations can also explain the absence of recrystallization in GMR systems optimized for the first AFC maximum. The single layer thicknesses in this case are only about 1 nm, which increases the interfacial/surface energy term significantly. In fact, if the periodicity of multilayer (the thickness of the NiFe and Cu bilayer) is smaller than about 3-4 nm, the initial <111> texture becomes stable and represents the minimum of the system's free energy. The texture reorientation is thus precluded.

Chapter 7

Conclusions

The mechanisms of GMR deterioration in the Co/Cu system have been studied by atom probe tomography. In the temperature range up to 500 °C, the interfacial width remains constant having a value of 6-7Å. Strong repulsive interaction between cobalt and copper atoms opposes the chemical mixing at the interfaces in spite of the high material mobility at elevated temperatures. This behavior is in contrast to that of Py/Cu multilayers. In the Py/Cu system, a short range mixing at the interfaces is observed, which is caused by gradient energies and is quantitatively described by the Cahn-Hilliard theory. The broadening of layer interfaces causes the GMR amplitude breakdown in this system already at about 250 °C.

Due to the favorable thermodynamics (stability of the miscibility gap), Co/Cu multilayers remain stable until morphological changes come into play at about 450 °C. Two types of morphological changes are detected, causing the formation of ferromagnetic bridges through the Cu layer:

- layer faceting (first detected at 400 °C);
- breakthroughs of Co through the Cu layer along grain boundaries (detected at 450 °C).

Both morphology transformations are driven by the interfacial energy minimization. Layer faceting occurs due to the interfacial energy anisotropy. As observed in specimens grown on curved substrates (tungsten tips), <111> interface orientation is preferred over the other configurations leading to the formation of <111> facets on the interface and steps on locations, where the interface plane significantly deviates from the <111> orientation (by an angle of about 10-15°). Finally, Co breakthrough occurs through the Cu layer eliminating the unfavorably oriented interface portions. This observation can explain strong ferromagnetic coupling (low GMR amplitudes) in multilayers with high layer waviness. The second mechanism of Co bridging is observed on flat parts of the layer interfaces. Realistic nucleation barriers of about $30\,kT$ were assessed for the formation of Co bridges through 1 nm thick Cu layers. The barrier height has a quadratic dependence on the Cu layer thickness, which explains higher stability of the

multilayer systems optimized for the second AFC maximum. At later annealing states, massive destruction of the layered geometry is observed due to layer interpenetration. The morphology of the system develops towards material fragmentation.

Besides the described reactions, recrystallization leading to a complete transformation of layer texture is observed in both metallic systems. As demonstrated by elasto-mechanic calculations, this transformation is induced by elastic anisotropy of the metallic components. Microstructural transformation has an important impact on the magnetoresistivity. Taking into account the rotation of lattice orientation already during the preparation of thin films, GMR senor layers of high thermal stability can be produced.

Although Py/Cu and Co/Cu are equivalent in respect to the observed phenomenon, the Ni_xFe_{1-x}/Cu system is chosen for a detailed analysis, because it allows a precise control of the lattice constant by varying the Fe content in the Ni_xFe_{1-x} layer. It is shown that the anisotropic elastic energy induced by the lattice mismatch is the main driving force for the <111> to <100> texture reorientation. Moreover, the counteraction between the elastic and interfacial energy minimizations exerts a critical influence on the recrystallization probability. The additional contribution of the orientational dependence of the interfacial/surface energy points at the <111> texture being the next favorable one. The importance of the interfacial/surface energy term increases with the decrease in the multilayer periodicity. Thus, the probability of recrystallization becomes rather low for layer thicknesses corresponding to the first AFC length.

Appendix A

Auxiliary tables for TAP acquisition data evaluation

Following tables are useful in the TAP data evaluation during the acquisition process. They predict the tip apex curvature radius, detection diameter (visible for the TAP zone on the tip surface) and detected atoms per nm depth for different values of applied voltage. Applied voltage is taken as follows: $U = U_{base} + \alpha U_{pulse}$. In table A.1 the parameters are given, used for the calculation of presented in tables A.2, A.3, A.4 and A.5 data. Atomic density is calculated from the lattice parameters of corresponding materials.

	Evaporation field, [V/nm]	Atomic density, [1/nm^3]
W	57	63.4
Co	36	90.2
Cu	30	84.7
Al	19	60.2
Aperture half-angle, [°]	35	
β	7	

Table A.1: Parameters used for the calculation of data presented in tables A.2, A.3, A.4 and A.5. Evaporation fields for respective materials are taken from [65]. Atomic densities are calculated using correspondent lattice parameters.

W

Applied voltage, [kV]	4	6	8	10	12	14	16
Tip radius, [nm]	10	15	20	25	30	35	40
Detection diameter, [nm]	12	18	24	30	36	42	48
Detected atoms per nm depth ($/10^3$)	4	8	15	23	33	44	58

Table A.2: Specimen parameters in dependence on applied voltage for pure W.

Co

Applied voltage, [kV]	4	6	8	10	12	14	16
Tip radius, [nm]	16	24	32	40	48	56	64
Detection diameter, [nm]	18	27	36	46	55	64	73
Detected atoms per nm depth ($/10^3$)	12	26	47	73	106	144	188

Table A.3: Specimen parameters in dependence on applied voltage for pure Co.

Cu

Applied voltage, [kV]	4	6	8	10	12	14	16
Tip radius, [nm]	19	29	38	47	57	67	76
Detection diameter, [nm]	22	33	44	55	66	77	87
Detected atoms per nm depth ($/10^3$)	16	36	64	99	143	195	254

Table A.4: Specimen parameters in dependence on applied voltage for pure Cu.

Al

Applied voltage, [kV]	4	6	8	10	12	14	16
Tip radius, [nm]	30	45	60	75	90	105	120
Detection diameter, [nm]	35	52	69	86	104	121	138
Detected atoms per nm depth ($/10^3$)	28	63	113	176	253	345	450

Table A.5: Specimen parameters in dependence on applied voltage for pure Al.

Appendix B

Equilibrium binary alloy phase diagrams

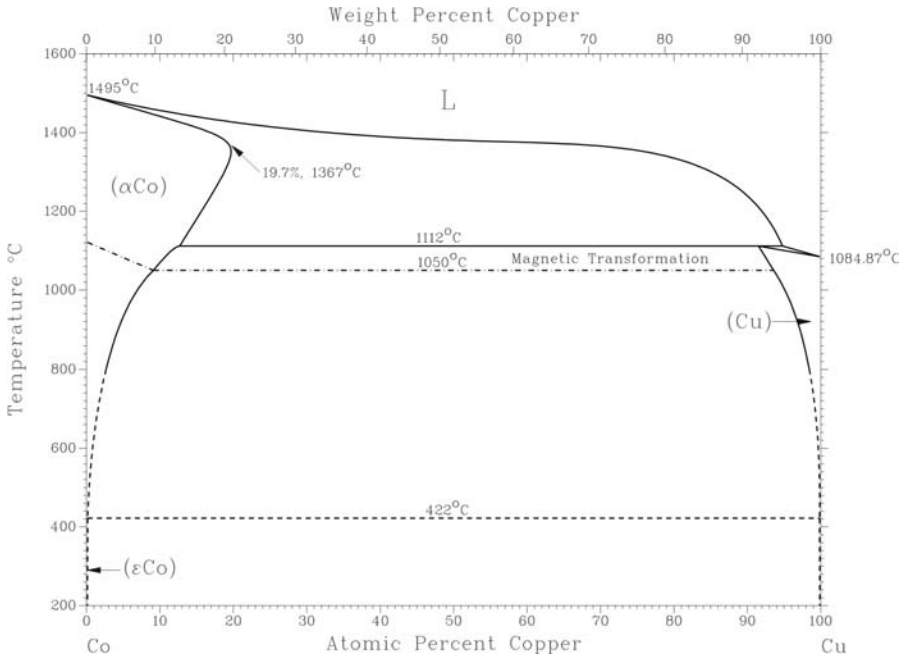

Figure B.1: Assessed CoCu phase diagram [105].

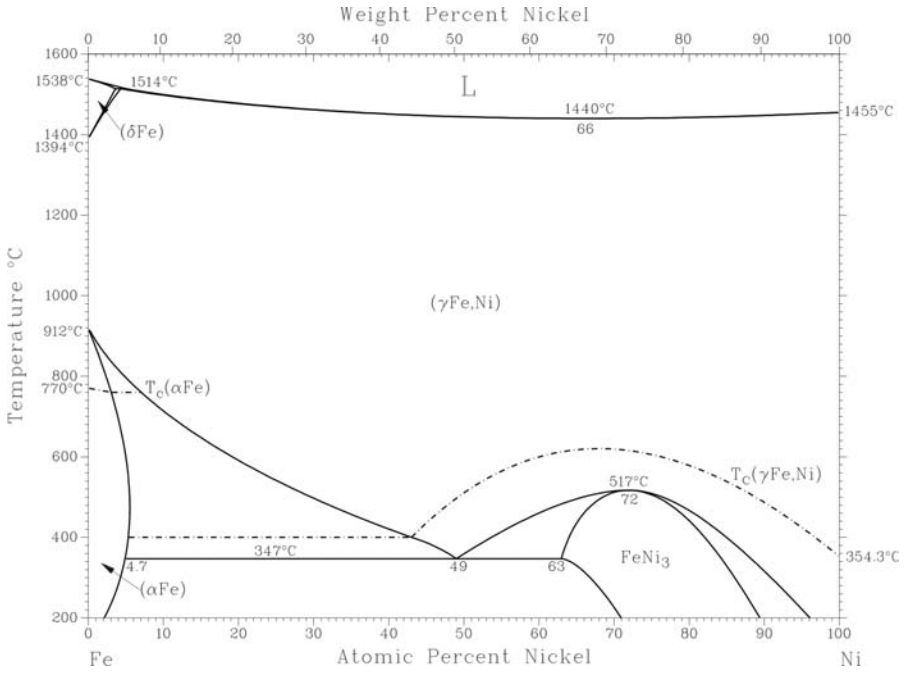

Figure B.2: Assessed FeNi phase diagram [105].

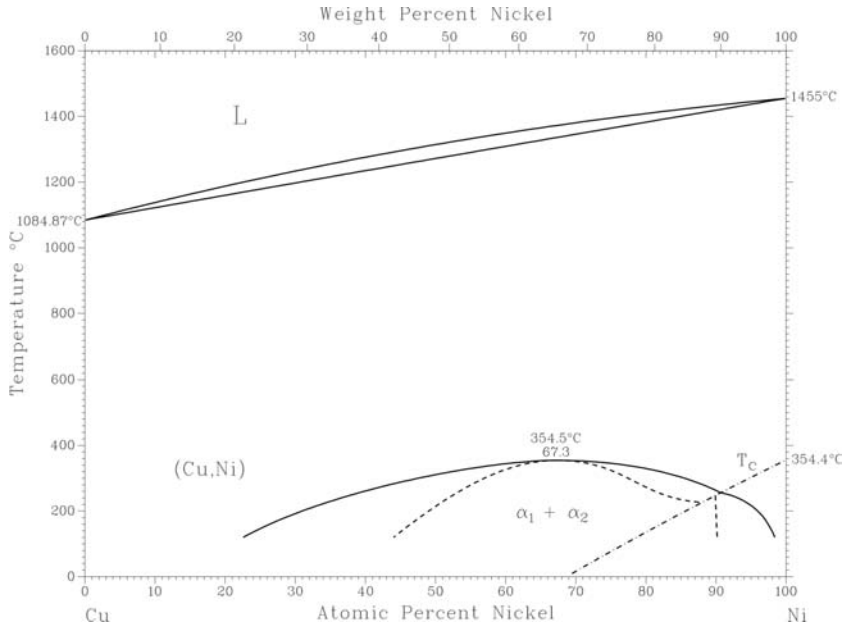

Figure B.3: Assessed CuNi phase diagram. Liquidus and solidus are obtained from experimental data. The low-temperature portion of the diagram is obtained from the thermodynamic modeling [105].

Appendix C

GMR multilayer systems investigated during preliminary study

The samples were prepared by magnetron sputtering using a sputtering system type *L560 Leybold Dresden* in the laboratory of the Bielefeld University. This system consists of four 4-inch magnetron sources, three of which are capable of sputtering magnetic materials. The sources were mounted in a vacuum chamber with basic pressure of $8 \cdot 10^{-7}$ mbar. The distance between target and sample was approximately 11 cm. Thermally oxidized [100] silicon wafers with the thickness of the oxide layer of 47 nm ($Si_{[100]}/(SiO_2)_{47nm}$) cut in pieces of suitable size as well as the conventional object car-

Set #	Multilayer structure	Substrate
1	$[Py_{2nm}Cu_{2nm}]_{40}$	A
2	$[Py_{4nm}Cu_{4nm}]_{40}$	A
3	$Cu_{6nm}/[Py_{2.7nm}Cu_{6nm}]_{40}$	A,B
4	$Cu_{6nm}/[Py_{6nm}Cu_{6nm}]_{40}$	A,B
5	$Cu_{6nm}/[Py_{4nm}Cu_{4nm}]_{20}$	A
6	$[Py_{6nm}Cu_{6nm}]_{40}/Ta_{5nm}$	A,B
7	$[Py_{6nm}Cu_{6nm}]_{20}/Ta_{5nm}$	A
8	$[Py_{10nm}Cu_{10nm}]_{20}/Ta_{10nm}$	A
9	$[Py_{3nm}Cu_{6nm}]_{40}$	A
10	$[Py_{4nm}Cu_{4nm}Co_{4nm}Cu_{4nm}]_{10}$	A
11	$[Py_{4nm}Cu_{4nm}Co_{4nm}Cu_{4nm}]_{20}$	A,B
12	$[Py_{3nm}Cu_{6nm}Co_{3nm}Cu_{6nm}]_{20}$	A,B
13	$[Co_{4nm}Cu_{4nm}]_{20}$	A,B
14	$[Fe_{4nm}Cu_{4nm}]_{20}$	A
15	$[\{(Fe_{0.5nm}Py_{0.5nm})_6\}/Cu_{6nm}]_8$	A,B

Table C.1: Sample ML architectures examined during preliminary study for the maximum recrystallization degree. A – thermally oxidized silicon wafer, B – object carrier glass.

Material	Sputtering power, W	Sputtering power per area, W/cm^2	Sputtering rate, nm/sec
Py	102	1.3	0.31
Cu	91	1.1	0.57
Co	105	1.3	0.39
Fe	105	1.3	0.27
Ta (cap)	105	1.3	0.25
$P_{risidual} = 8 \cdot 10^{-7}\, mbar$;		$P_{sputtering} = 10^{-3} mbar$	

Table C.2: Parameters of the magnetron sputtering

rier glass of $18 \times 18\,\mathrm{mm}^2$ were used as substrates for the ML deposition. Directly before the deposition the substrates were cleaned in ultrasonic bath using acetone and alcohol respectively and dried in nitrogen gas stream. The main sputtering parameters used during preparation of samples are listed in the Tab. C.2.

The high accuracy of multilayer architecture (thicknesses of the single layers) was provided by computer controlled deposition process. Due to the presence of the load lock chamber it was possible to produce a large amount of samples with different multilayer architectures within a limited time.

List of Tables

Bibliography

[1] Grünberg P, Schreiber R, Pang Y, Brodsky MB, and Sowers H, Phys. Rev. Lett. **57** (1986) 2442. 3, 7

[2] Baibich MN, Broto JM, Fert A, Nguyen Van Dau F, Petroff F, Etienne P, Creuzet G, Friederich A, and Chazelas J, Phys. Rev. Lett. **61** (1988) 2472. 3, 11, 12

[3] Binash G, Grünberg P, Saurenbach F, and Zinn W, Phys. Rev. B **39** (1989) 4828. 3, 11

[4] Hütten A, Mrozek S, Heitmann S, Hempel T, Brückl H, and Reiss G, Acta mater. **47** (1999) 4245. 4

[5] van Loyen L, Elefant D, Tietjen D, Hecker M, Thomas J, and Schneider CM, J. Appl. Phys. **87** (2000) 4852. 4

[6] Heitmann S, Hütten A, Hempel T, Schepper W, Reiss G, and Alof C, J. Appl. Phys. **87** (2000) 4849. 4

[7] Hecker M, Tietjen D, Wendrock H, Schneider CM, Cramer N, Malkinski L, Camley RE, and Celinski Z, J. Magn. Magn. Mater. **247** (2002) 62. 4, 74, 78

[8] Rätzke K, Hall MJ, Jardine DB, Somekh RE, and Greer AL, J. Magn. Magn. Mater. **204** (1999) 61. 4, 78

[9] Bobeth M, Hecker M, Pompe W, Schneider CM, Thomas J, Ullrich A, and Wetzig K, Z. Metallkunde **92** (2001) 810. 5, 78

[10] Schleiwies J, Schmitz G, Heitmann S, and Hütten A, Appl. Phys. Lett. **78** (2001) 3439. 5

[11] Ene CB, Schmitz G, Kirchheim R, and Hütten A, Acta Materialia **53** (2005) 3383. 5, 70, 74

[12] Heitmann S, *Cobalt / Copper Multilayers: Interpalay of Microstructure and GMR and Recrystallization as the Key Towards Temperature Stability*, PhD thesis, Bielefeld University, Bielefeld, 2004. 5, 71, 72, 73, 79, 94

[13] Slonczewski JC, J. Magn. Magn. Mater. **150** (1995) 13. 7

[14] Yan SS et al., Phys. Rev. B **59** (1999) 11641. 7

[15] Parkin SSP, More N, and Roche KP, Phys. Rev. Lett. **64** (1990) 2304. 7

[16] Néel L, Comptes Rendus **255** (1962) 1676. 7

[17] Larson DJ, Petford-Long AK, Ma YQ, and Cerezo A, Acta Mater. **52** (2004) 2847. 7

[18] Mangan MA, Spanos G, McMichael RD, Chen PJ, and Egelhoff Jr. WF, Metal. and Mat. Trans. A **32** (2001) 577. 8

[19] Bürgler DE et al., *Handbook of Magnetic Materials*, Elsevier, 2001. 8

[20] Yafet Y, J. Appl. Phys. **61** (1987) 4058. 8

[21] Ruderman MA, Kittel C, Phys. Rev. **96** (1954) 99. 8

[22] Kasuya T, Prog. Theor. Phys. **16** (1956) 45. 8

[23] Yosida K, Phys. Rev. **106** (1957) 893. 8

[24] Bruno P, Chappert C, Phys. Rev. Lett. **67** (1991) 1602. 8

[25] Stiles MD, Phys. Rev. B **48** (1993) 7238. 8

[26] Bruno P, Phys. Rev. B **52** (1995) 411. 8

[27] Kohler M, Metalle. Ann. Phys. **32** (1938) 211. 10

[28] Englert E, Ann. Physik **14** (1932) 589. 10

[29] McGuire T, Potter R, IEEE Trans. Magn. **11** (1975) 1018. 11

[30] Hartmann U, *Magnetic Multilayers and Giant Magneto-Resistance. Fundamentals and industrial applications*, volume 37 of *Springer series in surface sciences*, Springer, 2000. 11

[31] Grünberg P, Physik J. **6** (2007) 33. 13, 16, 110

[32] Blondel A, Meier JP, Doudin B, and Ansermet JP, Appl. Phys. Lett. **65** (1994) 3019. 12

[33] Berkowitz A, Mitchell JR, Carey MJ, Young AP, Zhang S, Spada FE, Parker FT, Hutten A, and Thomas G, Phys. Rev. Lett. **68** (1992) 3745. 12

[34] Shinjo T, Yamamoto H, J. Phys. Soc. **59** (1990) 3061. 13

[35] Gijs MAM, Johnson MT, Reinders A, Huisman PE, Veerdonk RJM, Lenczowski SKJ, and Gansewinkel RMJ, Appl. Phys. Lett. **66** (1995) 1839. 13

[36] Piraux L, George JM, Despres JF, Leroy C, Ferain E, Legras R, Ounadjela K, and Fert A, Appl. Phys. Lett. **65** (1994) 2484. 13

[37] Julliere M, Phys. Lett. A **54** (1975) 225. 16

[38] Jonker GH, Santen JH, Physica B **16** (1950) 337. 17

[39] Kusters RM, Singleton J, Keen DA, McGreevy R, and Hayes W, Physica B **155** (1989) 362. 17

[40] Helmholt R, Wecker J, Holzapfel B, Schultz L, and Samwer K, Phys. Rev. Lett. **71** (1993) 2331. 17

[41] Jesser WA, Matthews JW, Phil. Mag. **17** (1968) 461. 17, 62, 84

[42] Schmid AK, Kirschner J, Ultramicroscopy **42-44** (1992) 483. 17, 62

[43] Hammer L, Müller S, and Heinz K, Surf. Sci. **569** (2004) 1. 17

[44] Smith DJ, Modak AR, Rabedeau TA, and Parkin SSP, Appl. Phys. Lett. **71** (1997) 1480. 17

[45] Freund LB, and Suresh S, *Thin Film Materials: Stress, Defect Formation and Surface deformation*, Cambridge University Press, 2004. 17, 22

[46] Thompson CV, Scr. Metal. Mater **28** (1993) 167. 17, 30, 92

[47] Galanakis I, Bihlmayer G, Belline V, Paranikolaou N, Zeller R, Blügel S, and Dederichs PH, Europhys. Let. **58** (2002) 751. 18

[48] Wulff G, Zeitschr. Krystallogr. Mineral. **34** (1901) 449. 19

[49] Young T, Philosophical transactions of the Royal Society (London) **95** (1805) 65. 20

[50] Aufray B, Giordano H, Legrand B, and Tréglia G, Surf. Sci. **307-309** (1994) 531. 21

[51] Zimmerman CG, Yeadon M, Nordlund K, Gibson JM, and Averback RS, Phys. Rev. Let. **83** (1999) 1163. 21

[52] Doerner MF, Nix WD, CRC Critical Reviews in Solid State and Materials Sciences

14 (1988) 225. 22

[53] Floro JA, Hearne SJ, Hunter JA, Kotula P, Chason E, Seel SC, and Thompson CV, J. Appl. Phys. **89** (2001) 4886. 24, 25

[54] Mays CW, Vermaak JS, and Kuhlmann-Wilsdorf D, Surf. Sci. **12** (1968) 134. 24

[55] Chason E, Sheldon BW, Freund LB, Floro JA, and Hearne SJ, Phys. Rev. Lett. **88** (2002) 156103. 25

[56] Sheldon BW, Ditkowski A, Beresford R, Chason E, and Rankin J, J. Appl. Phys. **94** (2003) 948. 25

[57] Nix WD, Metal. Trans. A **20** (1989) 2217. 27

[58] Thompson CV, Annu. Rev. Mater. Sci. **30** (2000) 159. 28

[59] Thompson CV, Carel R, Mat. Sci. Eng. **B32** (1995) 211. 29

[60] Greiser J, Müllner P, Arzt E, Acta Mater. **49** (2001) 1041. 29

[61] Thompson CV, J. Mater. Res. **8** (1993) 237. 30, 92

[62] Hirth JP, Lothe J, *Theory of dislocations*, Wiley-Interscience, 2nd ed., 1982. 30

[63] Müller EW, Z. Physik **131** (1951) 136. 34

[64] Cerezo A, Godfrey TJ, and Smith GDW, Rev. Sci. Instrum. **59** (1988) 862. 34

[65] Miller NK, Cerezo A, Hetherington MG, and Smith GDW, *Atom Probe Field Ion Microscopy*, Clarendon Press, Oxford, 1996. 42, 104, 110

[66] Schmitz G, *Microstructural mechanisms of solid state interreactions*, Habilitation thesis, Göttingen University, 2001. 42

[67] Keller H, Klingelhöfer G, and Kankelheit E, Nucl. Instr. And Meth. **A258** (1987) 221. 42

[68] Oberdorfer C, *Aufbau einer Laserverdampfungsstrecke für die Tomographische Atomsonde*, Diploma thesis, Münster University, 2006. 43

[69] Unger HG, *Elektromagnetische Wellen auf Leitungen*, Hüthig Verlag, 1996. 43

[70] al-Kassab T, Wollenberger H, Schmitz G, Kirchheim R, *High-Resolution Imaging and Specrtometry of Materials, Chapter "Tomography by Atom Probe Field Ion Microscopy"*, Springer, 2003. 47

[71] Vurpillot F, Bostel A, and Blavette D, Appl. Phys. Lett. **76** (2000) 3127. 49

[72] Bas P, Bostel A, Deconihout B, and Blavette D, Appl. Surf. Sci. **87/88** (1995) 298. 50

[73] Jeske T, Schmitz G, Mat. Sci. Eng. A **327** (2002) 101. 50

[74] ICDD, Powder diffraction file, http://www.icdd.com/. 51

[75] Cullity BD, *Elements of x-ray diffraction*, Addison-Wesley, 2nd, 1977. 52

[76] Nowak C, Kirchheim R, and Schmitz G, Appl. Phys. Lett. **89** (2006) 143104. 60

[77] Hecker M Mattern N, Brückner W, and Scheider CM, Mat. Sci. Forum **443-444** (2004) 193. 62

[78] You DK, Bonzel HP, Scheffler M, New J. Phys. **8** (2006) 65. 66

[79] Straumal BB, Polyakov SA, Mittemeijer EJ, Acta Materialia **54** (2006) 167. 66

[80] Hecker M, Thomas J, Tietjen D, Baunack S, Schneider CM, Qiu An, Cramer N, Camley RE, and Celinski Z, J. Phys. D: Appl. Phys. **36** (2003) 564. 69, 74

[81] Hecker M, Pitschke W, Tietjen D, and Schneider CM, Thin Solid Films **411** (2002) 234. 74

[82] Michaelsen C, Philos. Mag. A **72** (1995) 813. 74

[83] Pearson WB, *A Handbook of Lattice Spacings and Structures of Metalls and Alloys*, volume 2, Pergamon, 1st ed., New York, 1967. 75

[84] Ebrahimi F, and Li HQ, Rev. Adv. Mater. Sci. **5** (2003) 134. 75

[85] Hearmon RFS, The elastic constants of crystals and other anisotropic materials, in *Landolt Börnstein, New Series, Group III Condensed Matter*, edited by Hellwege KH and Hellwege AM, volume 18, Springer, Berlin, 1984. 75, 83

[86] Leith SD, Ramli S, and Schwartz DT, J. Electrohem. Soc. **146(4)** (1999) 1431. 75, 77

[87] Larson DJ, Petford-Long AK, Cerezo A, Mat. Sci. Eng. **A270** (1999) 69. 78, 79, 80

[88] Langer J, Kräußlich J, Mattheis R, Senz St, Hesse D, J. Magn. Magn. Mat. **198-199** (1999) 644. 78, 79

[89] Kikuchi H, Bobo JF, Robert L, IEEE Trans. Magn. **33** (1997) 3583. 79

[90] Döhl R, Macht MP, Naundorf V, Phys. Stat. Sol. **86** (1986) 603. 80

[91] Tu KN, Mayer JW, Feldman LC, *Electronic Thin Film Science (For Electrical Engineers and Materials Scientists)*, Macmillan Publishing Company, New York, 1992. 83, 84

[92] Edington JW, *Monographs in Practical Electron Microscopy in Materials Science, Interpretation of Transmission Electron Micrographs*, University of Cambridge, Cambridge, England, 1975. 83

[93] Ebert R, Methods of measurement; thermodynamic properties of homogenous materials, in *Landolt Börnstein, 6th ed.*, edited by Hellwege KH and Hellwege AM, volume IV/4a, Springer, Berlin, 1967. 87

[94] Bonnenberg D, Hempel KA, Wijn HPJ, 3d, 4d and 5d elements, alloys and compounds, in *Landolt Börnstein, New Series, Group III Condensed Matter*, edited by Hellwege KH and Hellwege AM, volume 19a, Springer, Berlin/Heidelberg, 1986. 87

[95] Hearmon RFS, The elastic constants of crystals and other anisotropic materials, in *Landolt Börnstein, New Series, Group III Condensed Matter*, edited by Hellwege KH and Hellwege AM, volume 11, Springer, Berlin, 1979. 87

[96] Sanchez JE, Arzt E, Scripta Met. et Mat. **27** (1992) 285. 91

[97] Smithells CJ, *Metals Reference Book*, Butterworths, London, 4th ed, 1967. 92, 93

[98] Stöker H, *Taschenbuch d. Physik*, Thun, Frankfurt am Main, 3rd ed, 1998. 92, 93

[99] Hattenhauer R, Haasen P, Philosophical Magazine A **68** (1993) 1195. 97

[100] Servi IS, Turnbull D, Acta Metall **14** (1966) 161. 97

[101] Shiftlet GJ, Lee YW, Aaronson HI, and Russel KC, Scripta Metall **15** (1981) 719. 97

[102] Vitos L, Ruban AV, Skriver HL, and Kollár J, Surf. Sci. **411** (1998) 186. 97

[103] Tyson WR, Miller WA, Surf. Sci. **62** (1977) 267. 98

[104] de Boir FR, Boom R, Mattens WCM, and Miedema AR, *Cohesion in Metals*, North-Holland, Amsterdam, 1988. 98

[105] Massalski TB, *Binary phase diagrams*, American Society for Metals, Metals Park, 2nd ed., Ohio, 1990. 106, 107

Publications and conferences

Publications

[1] V. Vovk, G. Schmitz, R. Kirchheim. Three-dimensional atom probe investigation of Co/Al thin film reaction. *Microelectron. Eng.*, 70(2-4):533–538, 2003.

[2] M.O. Pasichnyy, V. Vovk and A.M. Gusak. In A.I. Kuzmichev, V.I. Lapshin and V.M. Shulayev, editor, *Proceedings of the 15th International Symposium on Thin-Films in Optics and Electronics*, page 128. Constanta, Kharkiv, 2003.

[3] V. Vovk, G. Schmitz, R. Kirchheim. Nucleation of product phase at reactive diffusion of Al/Co. *Phys. Rev. B*, 69:104102, 2004.

[4] V. Vovk, G. Schmitz. Nucleation and growth during early stages of reactive diffusion. *Def. Diff. Forum*, 837:237–240, 2005.

[5] E. Nembach, J. Pesicka, V. Mohles, D. Baither, V. Vovk, T. Krol. The effect of a second aging treatment on the yield strength of γ'-hardened NIMONIC PE16-polycristals having γ'-precipitate free zones. *Acta Mater.*, 53:2485–2494, 2005.

[6] M.O. Pasichnyy, G. Schmitz, A.M. Gusak and V. Vovk. Application of the critical gradient concept to the nucleation of first product phase in Co/Al thin films. *Phys. Rev. B*, 72:014118, 2005.

[7] V. Vovk, G. Schmitz and A. Hütten. Mismatch-induced recrystallization of giant magnetoresistance multilayer systems. *Appl. Phys. Lett.*, 88:023120, 2006.

[8] V. Vovk, G. Schmitz, A.Hütten, S. Heitmann. Mismatch-induced recrystallization of giant magnetoresistance (GMR) multilayer systems. *Acta Mater.*, 55:3033–3047, 2007.

Conferences

2002 - 48th International Field Emission Symposium (IFES), Lyon/France.
Three-dimensional atom probe investigation of Al/Co thin film reaction. (Poster)

2003 - EU-Workshop on Materials for Advanced Metallization (MAM), Marseille/France.
Initial stages of interreaction in Al/Co thin film system. (Poster)

2003 - Spring Meeting of German Physical Society (DPG), Dresden/Germany.
Three-dimensional atom probe investigation of Al/Co thin film reaction. (Talk)

2005 - Spring Meeting of German Physical Society (DPG), Berlin/Germany.
Recrystallization effect in giant magnetoresistance systems during annealing. (Talk)

2006 - 50th International Field Emission Symposium (IFES), Guilin/China.
Thermal stability of Co/Cu and Py/Cu giant magnetoresistance systems.(Talk)

2007 - Spring Meeting of German Physical Society (DPG), Regensburg/Germany.
Thermal stability of Co/Cu and Py/Cu giant magnetoresistance (GMR) systems. (Talk)

2007 - Diffusion and diffusional phase transformation in alloys (DIFTRANS), Uman/Ukraine.
Thermal stability of Co/Cu and Py/Cu giant magnetoresistance (GMR) systems. (Talk)

Invited talk

2007 - Invited talk in Groupe de Physique des Matériaux, Rouen/France.
Thermal stability of Co/Cu and Py/Cu giant magnetoresistance (GMR) systems.

Acknowledgements

Here I would like to owe my gratitude to all the people who helped me during my PhD study. Without the outstanding resources of the Institute of Material Physics – human as well as technical – this thesis would never have come into being.

First and foremost, I would like to thank Prof. Guido Schmitz, who invited me to start my PhD thesis in his group. I am grateful to him for being an excellent supervisor during my entire work. He had always had time for all kinds of discussions. His outstanding scientific scope enriched my research with great ideas and wise advices.

I am also grateful to Dr. Dietmar Baither for his support not only in electron microscopy experiments but also in daily work in the institute. I appreciate a lot his friendliness and high expertise. I would like to thank my room-mates Reza Abouzary, Christian Oberdorfer and Maria Gruber for good mood, numerous interesting discussions and assistance. I thank all of the group members for their companionship and collaboration. The positive working atmosphere made the work in the Institute of Material Physics to a real pleasure.

I would like to express my gratitude to Frank Spaleck and his fine-mechanics workshop team. Their qualified support was of great importance for the fulfillment of experimental work. There were no problems they could not manage. I would like to thank Bruno Lentfort for microprobe measurements and many other tasks he helped me with, our computer and electronics expert Friedbert Biermann for his professional support.

Special thanks go to Sylvia Gurnik and Annette Fröse, who helped to solve any question dealing with administrative paperwork or other complicated stuff the physicist cannot conceive.

And of course my most heartfelt gratitude goes to Lena and Kyrill for great support in my work and many beautiful moments we had together during these years of my PhD.

Thanks to everyone I've met in Münster!